Using ultrafast extreme-ultraviolet pulses for time-resolved dynamics of molecules chemisorbed on metal surfaces

by

Chi-Fong Lei

A dissertation submitted in partial fulfillment
of the requirements for the degree of
Doctor of Philosophy
(Electrical Engineering)
in The University of Michigan
2003

Doctoral Committee:

Professor Henry C. Kapteyn, Chair
Professor John Gland
Professor Margaret M. Murnane
Professor Stephen Rand

For Ruth, Matthew and Jacob

ACKNOWLEDGEMENTS

I would like to thank Profs. Henry Kapteyn and Margaret Murnane for their guidance and patience during my six years of graduate study. They are excellent advisors and have shown me how to tackle problems that I have never seen before, the defintion of scientific research. Their insight and knowledge at scientific problems have opened my eyes and led me to the vast world of physics. I especially thank them for giving me opportunities to try many different things, and providing good advices when needed. I also appreciate that they have given me freedom to apply my ideas to the experiments, never forcing me to do something that I did not want to. I thank Henry for his sometimes "nit-picky" requirements – requiring me to not only get the design working, but to also design it cheaply. I think this is good training for my future research – it is important not only to get the experiment done, but to do it well.

I thank Dr. Michael Bauer for his guidance and for bringing me to the field of surface physics. We had many good times doing these experiments, even while staying up very late in the laboratory. Not only did he have brilliant ideas regarding the experiments, he was also an excellent teacher. I would not have come this far if I had not working with him all these years. Furthermore, thanks for his encouragements which kept me going forwards when the experiments were not running well.

Thanks to Dr. Kendall Read for her valuable discussions about the experiments. Even though we worked together for just a couple of months, I appreciate her patience in explaining the fine details to me, when I was very junior and have absolutely no idea what I

was getting into.

I also want to thank many folks in the laboratory. Many thanks to Dr. Sterling Backus, Ron Tobey, and Dr. Lino Misoguti for their help on the laser systems, without their help these experiments would have been impossible. I would also like to thanks Prof. John Gland, Prof. Steven Rand, Prof. Dan Dassau, Dr. Yi-De Chuang, Emily Gibson, Dr. Kyoungsik Kim, Dr. Robert Shelton, Dr. Randy Bartels, Prof. Zenghu Chang, Prof. Charles Durfee, Dr. Eric Zeek, David Samuels, and Dr. Erez Gershgoren for their valuable discussions. Thanks to Dr. Yanwie Lui and Prof. David Attwood for making the high quality multilayer mirrors for my setup. And also thanks to the people in the JILA machine shop and electronics shop for their excellent support and equipment making, including Seth Wieman, Hans Green, Blaine Horner, David Alchenberger, Todd Asnicar, Paul Beckingham, Michael Whitmore, and James Fung-A-Fat. For the readability of this thesis, thanks are due to David Samuels, Racheal Tearle, and Marilee DeGoede, who corrected my grammar and writing style.

Finally, I would like to pay the greatest tribute to my family. My wife, Ruth, has sacrificed very much to support me through this entire process, and very likely I cannot ever hope to compensate her for her sacrificies. Thanks also to my mother, and my father- and mother-in-law for their support, both mentally and financially. Finally, my faith in Christianity has been vital to me, enabling me to survive some of the most difficult moments during these years.

TABLE OF CONTENTS

LIST OF TABLES

Table

LIST OF FIGURES

Figure

CHAPTER I

Introduction

Surfaces is known to be a very difficult physical system to study, due to tedious surface preparation procedures, and the requirement for maintaining the surface in an ultra-high vacuum chamber to maintain a clean and well-defined surface. Despite these difficulties, surfaces are very important to our daily life, since many chemical reactions actually happen on surfaces. Particularly, many metal surfaces are known to be very good catalysts for a large number of chemical reactions. Thus, understanding chemical reactions on metal surfaces – or in particular, how gas molecules adsorb on metal surfaces and then react – is currently a "hot topic" for many chemical physicists worldwide. In the last two decades, experiments designed to elucidate how gas molecules adsorb on metal surfaces, and how they react at the molecular level, have achieved great success. By utilizing surface sensitive techniques such as scanning tunneling microscopy (STM), low energy electron diffraction (LEED), high resolution electron energy loss spectroscopy (HREELS), ultraviolet photoemission spectroscopy (UPS), x-ray photoemission spectroscopy (XPS), and high-resolution electronic microscopy, many surface processes have become much better understood. However, experiments to directly observe dynamics of adsorbates on sur-

faces, to understand the fundamental time scales for chemical reactions, and to understand detailed dynamics, are still not generally available. This is because typical chemical reactions involve very high speed translational, vibrational and rotational molecular motions, characteristic of the activation energy for the reactants to create or destroy a chemical bond. The typical time scale for a molecule to translate, rotate, or vibrate on top of a metal surface is typically femtoseconds to picoseconds. For this reason, to observe the reaction dynamics of a chemical reaction in real time, surface techniques with sub-picosecond, ultrafast time resolution will be required to take a “snap-shot” of a chemical reaction as it happens.

Fortunately, ultrafast laser technology has advanced significantly in the last decade. Laser pulses with sub-30 fs pulse width and terawatt peak power can now be routinely and effectively generated in many laboratories [1]. Using these lasers, many different types of pump-probe experiments have been implemented to investigate chemical reactions, especially in the gas-phase and the liquid-phase. These experiments have already demonstrated many great successes. Pump-probe transient absorption spectroscopy and time-resolved raman spectroscopy are examples of successful and widely used techniques. However, these techniques cannot be directly applied to the investigation of adsorbate/surface chemical reactions. In general, since there is only a single mono-layer of active molecules adsorbed on the metal surface, surface-sensitive techniques with high sensitivity must be employed – otherwise, signals coming from the bulk material underneath surfaces will totally overwhelm the minute signals originating from the surface molecules.

Ultraviolet photoemission spectroscopy (UPS) has been extensively used for surface

studies, due to its excellent surface sensitivity. Typically, photons (energy range of 20 to 200 eV) generated either by synchrotrons or by laboratory-based light sources – such as a helium lamp – are used to photoeject electrons from a surface. Light in this energy range is called "extreme ultraviolet" or EUV. The reason for the high surface sensitivity of this technique stems from the fact that photo-emitted electrons in this kinetic energy range have an extremely short penetration depth for materials – typically about ~ 10 Å, or several mono-layers. Therefore, the electrons coming from the bulk will re-scatter back to the bulk and never escape from the surface, and only electrons originating from the surface escape it to be detected [2].

However, UPS techniques that use conventional EUV sources generally cannot be used to observe molecular dynamics. This is because even the-state-of-the-art synchrotron radiation sources emit light in "long" duration pulse of several tens of picoseconds, and helium lamps have no pulse structure. Thus, these light sources cannot be used to observe chemical reaction dynamics on sub-picosecond time scales. Fortunately, recently developed high-harmonic-generation (HHG) techniques can provide coherent EUV pulses with up to several hundred eV photon energy, and with femtosecond or even sub-femtosecond pulse duration [3, 4, 5]. High-harmonic generation is a high-order nonlinear process driven by an intense ultrafast pulse focused onto a noble gas medium. The strong electric field of the ultrafast pulse strips valence electrons from the atoms. The freed electrons are then accelerated by the strong electric field to very high speed. When the electric field reverses its direction as the electric field of the lightwave oscillates, these electrons turn around and recollide with the atomic core. The kinetic energy gained during the electric field

acceleration is then emitted as EUV photons. Since the complete generation process happens within one optical cycle of the infrared ultrafast pulse, the generated EUV pulses are typically shorter than the driving infrared pulse.

Therefore, by using these ultrashort EUV pulses, molecular dynamics on metal surfaces can be investigated by using so-called “pump-probe” techniques. Generally, a pump-probe experimental setup uses at least two laser pulses – one “pump” beam and one “probe” beam incident on the same spot on the surface. The pump beam initiates the physical phenomenon under study. Then, the probe beam is sent onto the surface with a time delay with respect to the pump beam, to “probe” the system status at that moment. This process is similar to taking stroboscopic pictures of the phenomenon at various times after it starts. The pump and the probe pulses should both be faster than the changes of the system; otherwise, these “snap-shots” will be blurred. In this work, an intense ultrafast infrared pulse will be the pump beam to trigger a surface system to evolve, and a EUV pulse will be used to probe the status of the system through, using the technique of EUV photoemission spectroscopy.

The use of ultrafast laser pulses to initiate a chemical reaction also results in a new and unique type of femtosecond laser-driven chemistry or “femtochemistry”. Surface chemical reactions driven by intense ultrafast laser pulses are different from conventional heat-mediated chemical reactions, in that the product yield from ultrafast laser-driven reactions is often much higher for a given amount of deposited energy. Also, otherwise unaccessible reaction pathways become possible using ultrafast pulse excitation. These findings suggest that the underlying mechanisms for these chemical reactions are different for ul-

trafast laser driven reactions. Non-equilibrium or “hot” electrons are created by sudden energy deposition – these hot electrons are likely the driving mechanism for these reactions, replacing the role of phonons in conventional surface chemistry. Furthermore, these hot electrons can nearly instantaneously reach effective temperatures of several thousand degrees while the phonons in the lattice remain cold. This “two temperature” situation differs for conventional phonon-mediated chemical reaction conditions, where the electrons and phonons have equal temperatures.

In this chapter, I give a brief overview describing the current status of the field of ultrafast surface chemistry.

1.1 Desorption induced by intense ultrafast pulses

Molecular desorption from a metal surface is one of the most basic phenomena in surface chemistry. When the temperature of a metal surface increases, atoms or molecules adsorbed on a surface will desorb. When an adsorbate-covered metal surface is irradiation by a continuous-wave (cw) laser or a nanosecond pulse laser, the desorption rate of adsorbates is a linear relation to the laser fluence. The traditional wisdom treats this phenomenon as a heat transfer process that transfers energy from the metal surface to the adsorbates through photon scattering with the adsorbates. The typical time scale for these processes is in the range of nanoseconds. Due to this “long” time scale, the metal surface and the adsorbates maintain an thermal equilibrium state throughout the desorption process. In particular, the electron temperature and the lattice temperature of the metal surface are equal to each other at all times during the heating process. Desorption happens solely due to phonon scattering from the lattice to the adsorbates, with no role for the surface

electrons.

However, desorption induced by femtosecond or picosecond laser pulses can no longer be explained by the photon scattering mechanism, because the desorption character is drastically different from the conventional case. In the case of an ultrafast laser pulse incidents on a metal surface, the desorption rate increases nonlinearly to the input laser fluence

$$Y \propto F^n \tag{1.1}$$

where Y is desorption yield, F is the laser fluence, and n is an experimental fitting parameter for the power-law – for example, for O_2/Pt(111), $n = 5.6 \pm 0.7$ [6]; for NO/Pd(111), $n = 3.3$ [7]. Furthermore, compared to the conventional thermal desorption, the desorption cross-section – the number of molecules desorbed per laser photon incident – induced by femtosecond pulses is exceptionally high. For example, NO and O_2 both exhibit roughly comparable desorption yields on Pd(111) in the case of conventional heating (nanosecond pulses irradiation), with a cross-section $\sigma_{thermal}$ of $\sim 10^{-22}$ cm^2. But when excited by femtosecond pulses, the NO and O_2 desorption yield increases tremendously, up to 1% desorption of the entire adsorbate coverage can be desorbed with each laser pulse incident. This corresponds to an effective desorption cross-section of $\sigma_{fs} \sim 10^{-18}$ cm^2 – a 4 order of magnitude increase [7].

In addition to the observation of a nonlinear increase in desorption yield with intensity, there are other unique characteristics of the femtosecond desorption process. The translational and vibrational energy distribution of the desorbed molecules was found to be characteristic of temperatures several times that of the lattice temperature. The desorp-

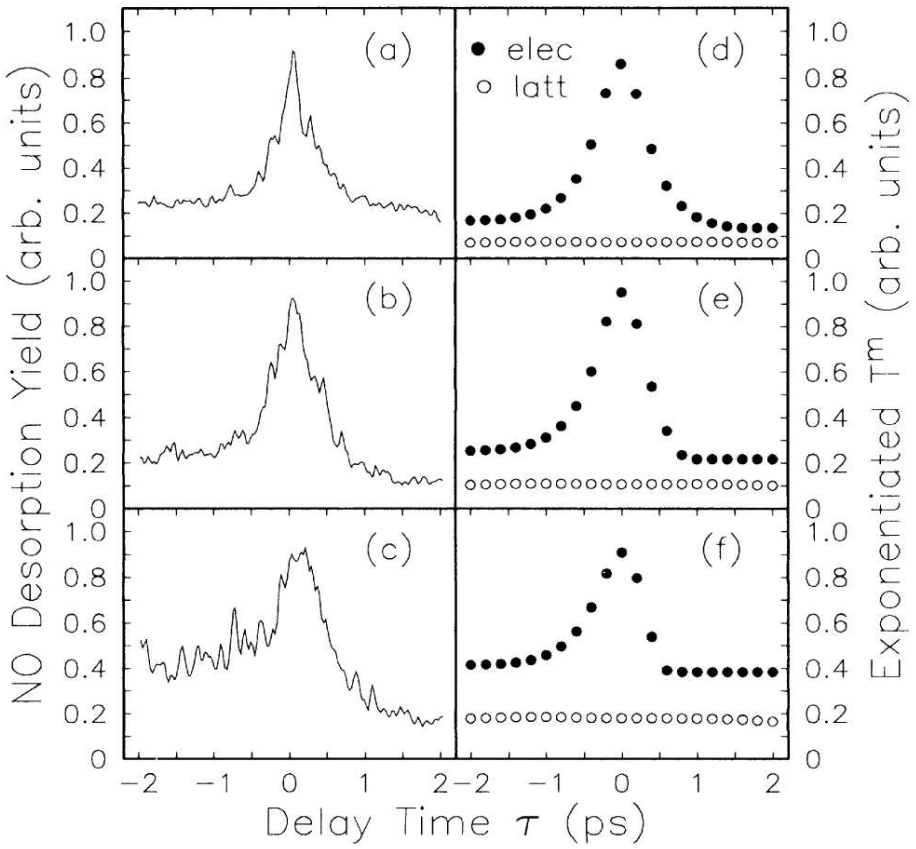

Figure 1.1: Desorption yield of two-pulse auto-correlation for NO on Pd(111) surface as a function of the time delay between the two ultrafast pulses. The laser fluences of the two pulses are varied as (a) 1.7 and 1.8 mJ/cm^2, (b) 1.6 and 2.2 mJ/cm^2, and (c) 1.3 and 3.0 mJ/cm^2. (d)-(f) Calculated temperatures of the surface electrons and the lattice phonons. (figure reproduced from Ref. [10])

tion angular distributions of the ejected molecules is also strongly forward peaked ($\cos^n\theta$, n$\gg$2), compared with a conventional $\cos^2\theta$ distribution [7, 8, 9].

In an attempt to understand the new mechanisms behind femtosecond laser desorption, correlation experiments have been used [10]. In this scheme, two ultrafast pulses are incident colinearly on the metal surface. The time-delay between these two pulses can be varied. Since the desorption yield for femtosecond laser desorption is nonlinear, the laser fluence of each pulse can be set low enough to avoid strong desorption from the

sample by a single pulse, but when the two pulses overlap in time, the desorption yield increases. Measuring the desorption yield as a function of the time-delay between the two pulses yields interesting results, as shown in Fig. 1.1. The full-width-half-maximum (FWHM) of this desorption peak is on the order of 1 ps which is longer than the duration of the pulse, but still short. Thus, the characteristic time scale of the process involved in the nonlinear desorption is $\sim$ps. This fast desorption time scale cannot be explained by the conventional phonon-induced desorption, or even multi-phonon induced desorption. However, calculations have shown that the temperature of surface electrons is heated much faster than the lattice phonons, and the temperature of the surface electrons can reach several thousand degrees, while the temperature of the lattice phonons does not increase significantly. Additionally, the temperature of surface electrons also has a decay time similar to that of the desorption peak, in contrast to the long (several tens of picoseconds) decay time of the lattice phonons [10, 11, 12]. Therefore, "hot" surface electrons created by the incident femtosecond laser is likely to be the underlying mechanism behind this novel desorption phenomenon.

1.2 Surface chemistry induced by femtosecond pulses

Chemical reactions on metal surfaces can also be induced by laser light. Similar to the case of desorption, conventional chemical reactions on metal surfaces can usually be explained by phonon-mediated mechanisms. For cw or nanosecond pulsed lasers, the reaction yield is generally linear proportional to the incident laser intensity. Furthermore, the product yield depends on the incident laser wavelength; for example, for the $\mathrm{CO} + \mathrm{O_2} + h\nu \rightarrow \mathrm{CO_2} + \mathrm{O}$ on platinum (111) single crystal, the $\mathrm{CO_2}$ yield is undetectable for

laser wavelengths longer than 550 nm with nano-second pulses [13, 14].

On the other hand, in the case of sub-picosecond laser pulse excitation, the results are very different. For the CO/O/Pt(111) case, it is possible to induce reactions with 800 nm light, and the production yield increases nonlinearly with pulse width and laser fluence; i.e. when the laser fluence at 800 nm increases by a factor of two, the CO_2 production increases by considerably more than a factor of ten [12, 15]. Additionally, the branching ratio of the desorption yield increases dramatically when sub-picosecond pulses are used: the desorption ratio of O_2 to CO_2 is about 10 for femtosecond pulses, in sharp contrast to the ratio of 0.5 found using nanosecond irradiation [12, 14]. To understand this new observation, two-pulse correlation techniques are also employed to investigate if these new phenomena can be accounted for by the involvement of hot surface electrons. For CO_2, the cross correlation desorption peak has a FWHM of 1.8 ps, indicating the surface electrons play an important role to this new type of reactions [12].

In additional to the nonlinear effects seen with femtosecond pulses, previously prohibited chemical reactions become possible in the case of ultrafast pulse excitation. This observation is exciting in that it hints that by using ultrafast laser pulses, surface chemistry can be manipulated. This control over surface reactions is a long standing goal of the field. CO/O/Ru(0001) is a good example of this control [16]. It is known that CO cannot be thermally oxidized on the ruthenium surface because the CO molecules desorb more easily from the surface than the O atoms, giving no opportunity for the oxidation to happen. However, when the ruthenium surface is irradiated by ultrafast pulses, hot surface electrons induced by the ultrafast pulses now transfer to an non-occupied level of the oxygen

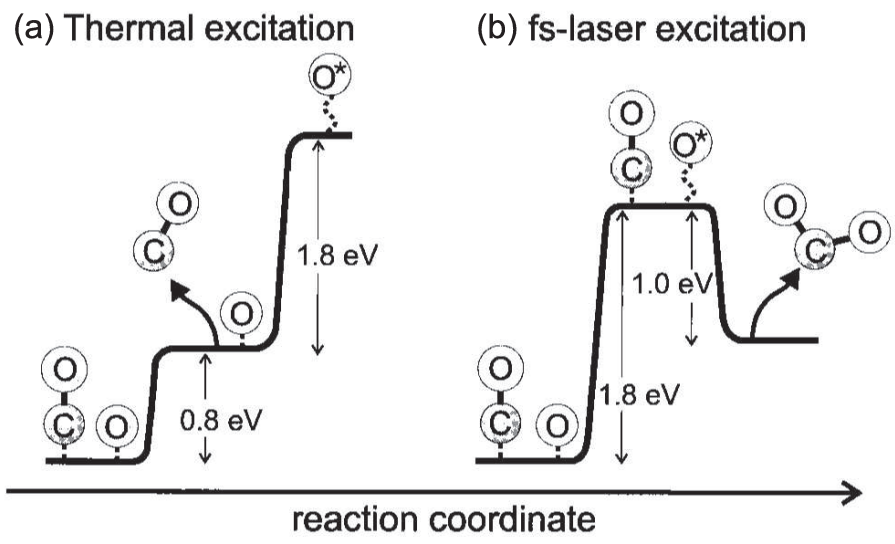

Figure 1.2: Illustration of the CO/O/Ru(0001) reaction. (a) CO has a much lower desorption barrier comparing to oxygen, which prohibit CO oxidation with the O atom when excited thermally. (b) Under femtosecond pulse excitation, the 1.8 eV barrier for O activation is overcome by coupling from the hot electrons, and CO_2 can be formed. (figure reproduced from Ref. [16])

atom, transferring kinetic energy to the center-of-mass of the oxygen atom and causing the oxygen atom to move and react with the CO molecules. This process is shown in Fig. 1.2.

1.3 Two-photon photoemission spectroscopy

Section 1.2 discussed that the interaction of femtosecond lasers with surfaces results in a variety of new physical phenomena. However, femtosecond lasers can also help study dynamic processes on surfaces. In particular, two-photon photoemission (2PPE) spectroscopy is the most versatile tool for studying electronic dynamics on metal surfaces.

The basic experimental setup for 2PPE is very similar to that for the two pulse desorption experiment described in Sec. 1.1, except that photoelectrons emitted from the sample surface are detected, rather than desorbed molecules. Valuable electronic dynamics infor-

mation can be obtained by measuring the kinetic energies of these photoelectrons. These data constitute photoelectron energy spectra corresponding to different time delays between the two incoming pulses. For the 2PPE experiment shown in Fig. 1.3(a), the photon energy of the first ultrafast pulse is generally not high enough to liberate electrons into the vacuum; however, together with the second pulse, the combined photon energies are large enough to overcome the work function of the surface. Therefore, when the first ultrafast pulse arrives, electrons in the valence band are excited to an "intermediate" state – located between the Fermi edge and the vacuum level – by the first pulse, and the excited electrons will stay at these intermediate levels with a lifetime τ. If the second ultrafast pulse arrives within this lifetime τ, electrons residing in this intermediate level will be ejected from the surface. Therefore, electron dynamics – and in particular the intermediate life time τ – can be measured by observing how the photoelectron energy spectra change with respect to the time delay between the two ultrafast pulses.

1.3.1 Image-potential states

Many interesting physical systems can be studied using 2PPE. For example, image-potential states have been extensively studied by 2PPE. An image-potential state is an energy state located just below the vacuum level of the metal surface, where the image-potential state electron is hovering above the metal surface, but is loosely bound. The binding force can be understood by considering the image charge of opposite sign positioned behind the metal surface at a distance equal to the electron. The image charge is actually a mathematical equivalent of the charge redistribution accumulated on the metal surface. Since the electron is loosely bound by the surface, the wavefunction of the image-

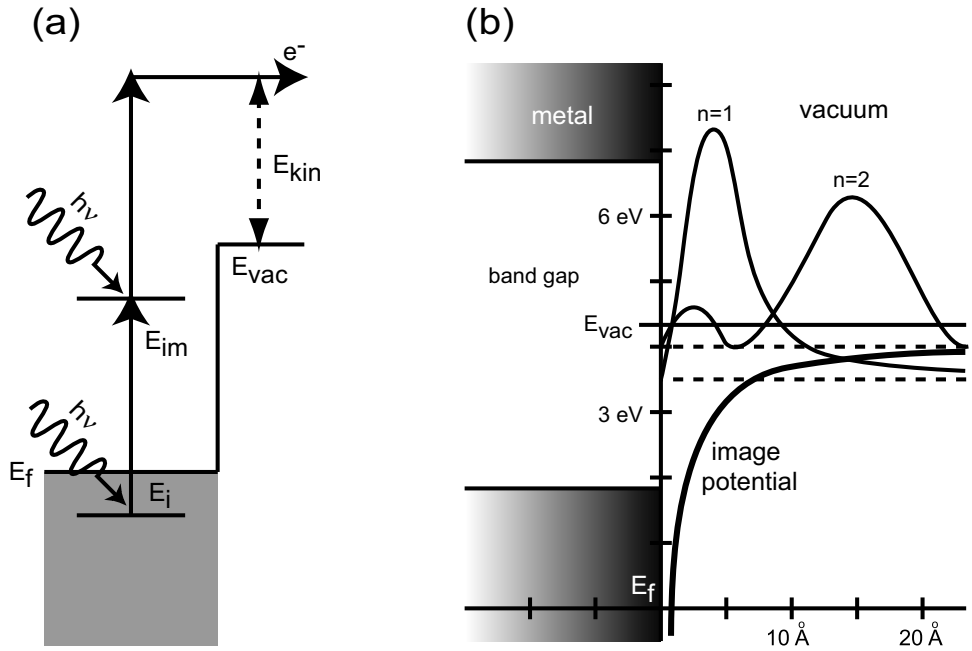

Figure 1.3: (a) Schematic energy diagram illustrating the process of two-photon photoemission. (b) Image-potential in front of a metal surface. The figure shows the wavefunction probabilities and the energy levels of the $n = 1$ and 2 image-potential states. The figure also shows the energy band gap of the metal surface, prohibiting the image-potential state electron from penetrating back into the metal surface. (figure reproduced from Ref. [17])

potential state electron can extend up to several ten Å from the metal surface, as shown in Fig. 1.3(b). Since these electronic wavefunctions exist nearly completely in the vacuum, these electrons spend most of their time in the free space, and the chance to scatter with the surface for relaxation is greatly reduced. Therefore, the image potential states are expected to be long lived relative to bulk states in metal at comparable excess energies. Image-potential states provides an opportunity to understand the dynamics of a two-dimensional electron gas in a vacuum.

Since the nature of this coulomb potential binding the electron to the surface is that of attraction to an "image" charge, the energy level structure is similar to that of the hydrogen atom; i.e. an electron and a proton. The image-potential $V(z)$ can be expressed as [17]

$$V(z) = \frac{-e^2}{4\pi\varepsilon_0}\frac{1}{4z} \tag{1.2}$$

where z is the distance from the metal surface. This differs from the hydrogen atom potential by only a factor of 4 in the denominator and the one-dimensional nature of the potential. Therefore, the image states are similar to the Rydberg states, and the binding energy (with respect to the E_{vac}) of the n^{th} image state is

$$E_b(n) = \frac{\mathrm{R_y}}{16n^2} = \frac{0.85}{n^2}\,\mathrm{eV} \qquad n = 1, 2, \cdots \tag{1.3}$$

A second reason for the long relaxation time of the image potential states is that the energy levels of these states usually lie within the projected surface band gap of a metal. This further pushes the electronic wavefunctions away from the surface. Therefore, the electron has even fewer opportunities to scatter with the metal surface and relax. In general, for a high order image-potential state ($n > 1$), the wavefunctions extend much farther away

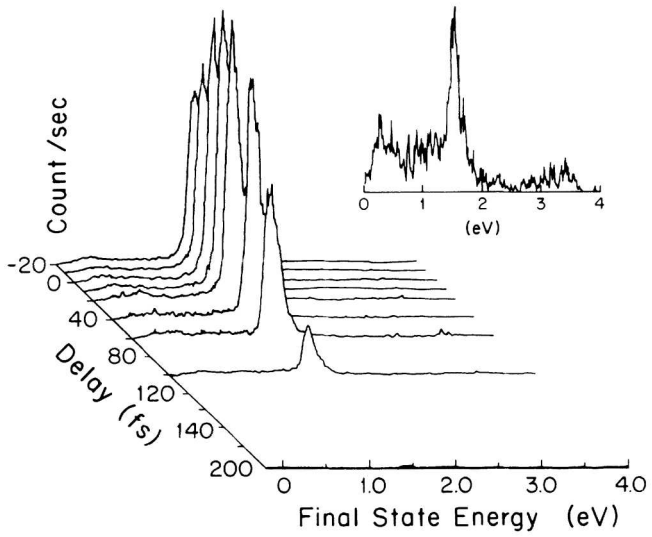

Figure 1.4: Two-Photo photoemission spectra showing the the image-potential state of an Ag(100) surface at various time delays. The signal is maximized at 0 fs time delay, and gradually decreases with positive time delay. Inset ($\times 100$ vertical scale): the background spectra at $+200$ fs time delay due to 2PPE by the single beam excitation (both pump and probe). (figure reproduced from Ref. [19])

from the metal surface, and the relaxation time for these states can be as long as several hundred femtoseconds.

Inverse photoemission techniques can also be used to measure the relaxation lifetime of image-potential states, by populating the image states and measuring the intrinsic linewidth Γ, which is related to the lifetime τ via the uncertainty principle $\Gamma \cdot \tau = \hbar$. This method is particular useful in measuring the $n = 1$ image-potential state, for the typical relaxation time of the $n = 1$ state is rather short, i.e. $\Gamma = 16$ meV or the lifetime $\tau = 41$ fs for the $n = 1$ state on Cu(111) [18]. However, for the higher order image-potential state, the lifetime is much longer, which results in a much narrower intrinsic linewidth. Hence inverse photoemission suffers from the minimum energy resolution of the electronic detectors to resolve the lifetime for these higher order states.

The first measurement of the lifetime of the image-potential state by using 2PPE was done on Ag(100) for the $n = 1$ state. The lifetime was estimated to be in the range of $15 - 35$ fs, measured with a 55 fs pulse width ultrafast pulses [19]. This is shown in Fig. 1.4, where the measured lifetime accuracy was hindered by the long pulse width of the laser pulses for the $n = 1$ state. For the $n = 1$ state on Ag(111) an upper limit for the lifetime of 20 fs is estimated [20]. The lifetime of the $n = 2$ state of the Ag(100) is considerably longer and could therefore be measured more precisely as 180 ± 20 fs [21].

1.3.2 Electron inelastic decay dynamics on an adsorbate covered surface

The previous section concludes that when electrons are excited to the image-potential states of a clean metal surface, the relaxation lifetime of these electrons can be very long (~ 100 fs). This is due to the loosely-bound characteristic of these states; with the wavefunctions of the excited electrons located far away from the metal surface (~ 20 Å). When adsorbate molecules are introduced to cover the clean metal surface, electrons can also be excited to an unoccupied resonance of these adsorbate molecules. However, these resonance states of the adsorbates are different from the image-potential states that they are very "localized". The electrons are now no-longer able to extend far away from the surface; rather, they are confined within the adsorbate molecules (several Å). Therefore, electrons in these resonance states have plenty opportunities to scatter with the decay channels inside the metal, resulting in a short inelastic decay time (several fs) for these excited electrons.

It would be useful to understand the inelastic decay dynamics of electrons in this situation because, as mentioned in Sec.. 1.1, desorption induced by femtosecond pulses is

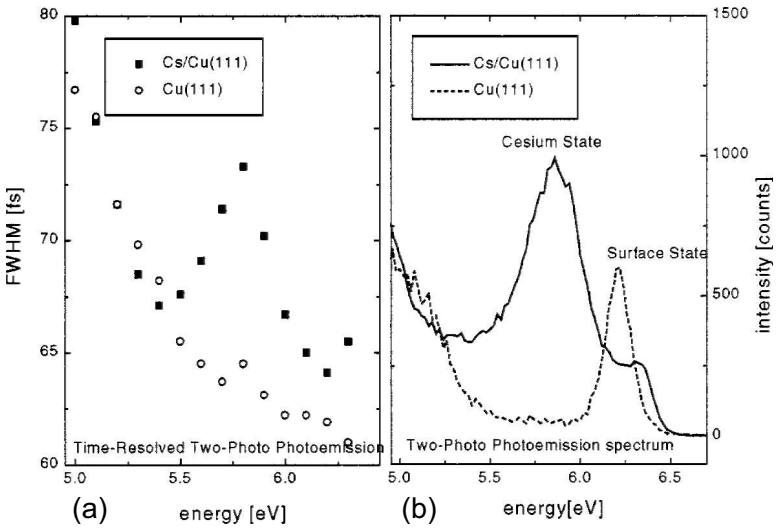

Figure 1.5: (a) Comparison of the full-width-half-maximum inelastic decay times between a Cs covered (0.8 ML) Cu(111) surface and a clean Cu(111) surface shows a remarkable time differences around the cesium unoccupied state between the Fermi edge and the vacuum level of Cu. Data are taken by time-resolved 2PPE. (b) 2PPE spectra of a Cs covered and a clean Cu(111) surfaces clearly shows a Cs induced peak appears at 5.8 eV. The pronounced peak at 6.2 eV of the clean surface (dashed spectrum) arises from the occupied Shockley surface state. (figure reproduced from Ref. [22])

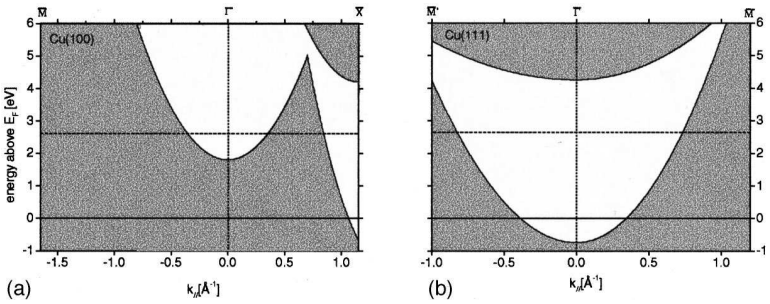

Figure 1.6: Projected surface band structure for (a) Cu(100) and (b) Cu(111). The dashed line indicates an energy level of an excited alkali state at 2.6 eV above E_f. The momentum distance to real bulk states from the band gap center is much smaller for Cu(100) than for Cu(111). (figure reproduced from Ref. [22])

generally explained by hot electrons occupying these adsorbate states. Fig. 1.5(b) compares 2PPE spectra of a clean copper surface (dashed line), and a Cs covered Cu(111) surface (solid line) [22, 23, 24]. It clearly shows that a Cs induced peak appears in the Cs covered spectra at 5.8 eV energy. This peak is attributed to an unoccupied cesium state that lives between the Fermi edge and the vacuum level.

M. Bauer *et al.* observed an exceptionally long inelastic decay time for this Cs state when adsorbed to Cu (111) surface [22]. As shown in Fig. 1.5(b), the decay time of the excited electron for the Cs covered Cu(111) surface is 74 fs, but the decay time of excited electrons in the same energy range for a clean copper surface is only 63 fs. The time difference between these two measurements corresponds to the inelastic decay time of this unoccupied state induced by the Cs atoms, where the excited electrons can be occupied. Hence the decay time of this unoccupied Cs state is estimated to be 11 ± 3 fs [23, 25].

However, when a Cs atom adsorbs on the (100) surface of copper, this inelastic decay time is reduced to 6 ± 4 fs. This discrepancy is generally explained by the difference in the band gap of the two Cu surfaces. Fig. 1.6 shows the projected surface band structures

for the Cu(100) and Cu(111) surfaces.

It has been known that for an image-potential state, in the first approximation, the lifetime is inversely proportional to the penetration of the wavefunction of the electron into the bulk [26]. Therefore, the closer the image-potential states are located to a band gap edge, the shorter the lifetime. On the other hand, for image-potential states, they exhibit quite a strong, nearly free-electron-like dispersion. This is because electrons in the image-potential states are rather loosely bound above the surface and the excited electrons are free to propagate along the other two dimensions of the surface. For a fixed excitation energy, the excited electrons are, however, harder to couple to the bulk states at high $k_{\|}$ value due to the restrictions of momentum conversation. This prohibits the excited electrons from relaxing into the bulk, resulting in a long decay time.

For the unoccupied states of the alkali atom at low coverage, no dispersion of this resonance state can be observed due to the localized property of these states. Therefore, in contrast to image-potential states, the decay process of the localized alkali excitation into the bulk states can in principle – within the requirement of energy conservation – also occur at quite high values of $k_{\|}$. Thus, at sufficiently high $k_{\|}$ values, real substrate states become accessible for decay. Therefore, the decay time of adsorbate resonances is typically very short. Furthermore, the increased inelastic lifetime from Cu(100) to Cu(111) can be explained by the position of the projected surface band gap. The band gap at $k_{\|} = 0$ down-shifts by approximately 3 eV from Cu(100) to Cu(111), as shown in Fig. 1.6. Because of such a large band gap for Cs/Cu(111), it reduces the decay channels for the electrons in the Cs resonance; and therefore, the relaxation time increases to 11 fs.

1.3.3 Atomic motion studied by 2PPE

Adsorbate atomic motion on metal surfaces can also be observed using 2PPE pioneered by H. Petek and his coworkers [27]. When Cs adsorbed on a Cu(111) surface, the band gap of the copper surface is between -0.85 and 4.1 eV (relative to the Fermi energy E_f). This inhibits the decay of the electron on the Cs atom, as discussed in the previous section. Therefore, the relaxation time for the excited Cs electrons is exceptionally long (~ 11 fs) [22, 28]. For the Cs/Cu(111) system, an intrinsic occupied surface state (*SS*) is located at -0.39 eV below the Fermi edge, and an unoccupied Cs anti-bonding state (*A*) is located at 3.1 eV (in the limit of zero Cs coverage). According to the theory [29], the exact energy level of the anti-bonding state *A* is strongly affected by the distance between the cesium atom and the copper surface $R_{\mathrm{Cu-Cs}}$, and when $R_{\mathrm{Cu-Cs}}$ increases, the energy level of *A* decreases. By using this property, 2PPE spectra are taken in which the pump creates the adsorbate motions and the probe tests its evolution. By subtracting the reference 240 fs spectrum, the 2PPE background component excited by the two separated, non interacting pulses is removed so that the correlation effects are much more prominent. As shown in Fig. 1.7(a), the maximum value of the photoemission signal shifts to lower energies with longer delays, indicating the cesium atom is moving away from the copper surface.

Figure 1.7(b) shows the energy shifts of *A* at various time delays, by which $R_{\mathrm{Cu-Cs}}$ can be deduced by inverting the time-dependent orbital energy $E_A(\Delta)$ via the calculated dependence of the $6s + 6p_z$ orbital energy on n $R_{\mathrm{Cu-Cs}}$. The results are shown in Fig. 1.7(c), indicating a motion of the Cs atom of about 0.3 Å in 180 fs. Furthermore, the excited potential energy surface of the Cs atom can be extrapolated from this data. A fit of the

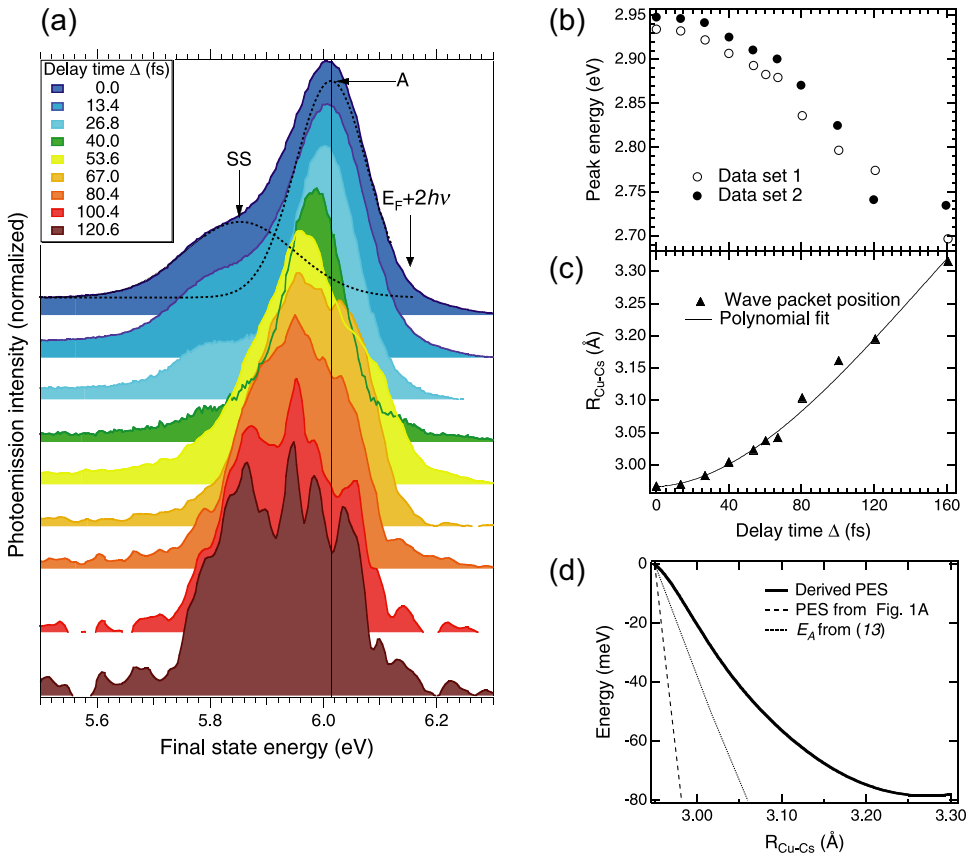

Figure 1.7: (a) The 2PPE difference spectra give information on the dynamic surface electronic structure. The 2PPE signal corresponds to one-photon absorption from both the pump and the probe beams, with the delay Δ set to an integral number of optical cycles. Dashed lines and solid vertical line indicate the Gaussian peak deconvolution of *SS* and *A*, and energy of *A* at $\Delta = 0$ fs, respectively. (b) $E_A(\Delta)$ from two independent experiments for $\theta_{\mathrm{Cs}} \sim 0.09$ ML. (c) The wave packet position $R_{\mathrm{Cu-Cs}}(\Delta)$ and its polynomial fit. (d) Dashed and solid lines, respectively, represent the predicted and derived excited state PES near the ground-state equilibrium geometry, and the dotted line represents the calculated anti-bonding state energy dependence on $R_{\mathrm{Cu-Cs}}$. (figure reproduced from Ref. [27])

$R_{\mathrm{Cu-Cs}}(\Delta)$ to the fourth-order polynomial gives a continuous function $R(\Delta)$, which is differentiated to obtain the acceleration of the Cs atom $a = \partial^2 R(\Delta)/\partial\Delta^2$. The force acting on the Cs atom, where $F = ma$, is then integrated, $U = -\int F dR$, to derive the experimental PES (Fig. 1.7(d))

This experiment demonstrated that the 2PPE can be used to measure the atomic motion on a surface – however, this technique is not universal enough to apply to other systems. The success of using 2PPE techniques in measuring atomic motion relies on the exceptionally long lifetime of the Cs anti-bonding state (*AA*) on Cu(111) resulting from the metallic band gap. As mentioned above, the typical lifetime of an excited electron in an intermediate state is rather fast (< 10 fs), and in general is not long enough to observe most atomic motions on surfaces.

1.4 Direct measurement of hot surface electrons induced by ultrafast pulses

Experimental data and theoretical modeling both suggest that the laser photons are mostly adsorbed in the substrate within a skin depth (100 Å) of the surface, rather than being absorbed in the adsorbate layer, thus eliminating multi-photon adsorption as a significant contribution to the nonlinear phenomena observed in Sec. 1.1 and 1.2 [31]. Due to the low heat capacity of electrons, theories had proposed that surface electrons can be highly excited by ultrafast pulses, while the lattice remains relatively cool. However, direct experimental confirmation of these highly excited surface electrons was not available until the work of J. Boker *et al* [30, 32, 33]. In his experiments, he heated a gold film with 1.84 eV photons to generate hot surface electrons. A second laser pulse was

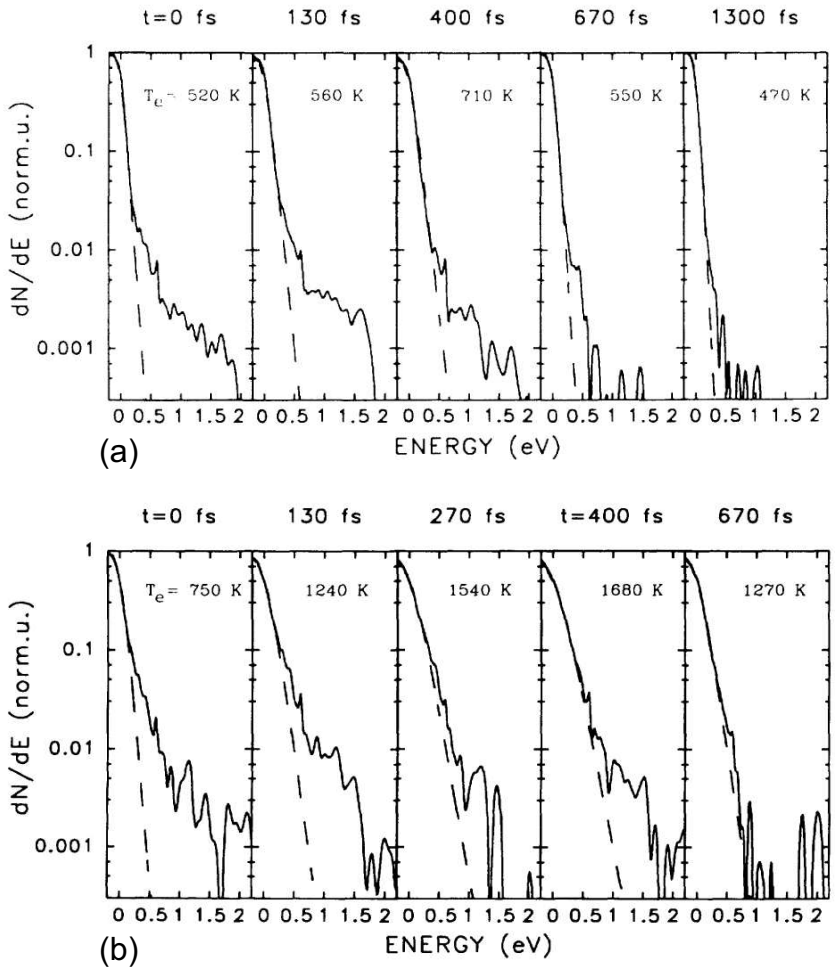

Figure 1.8: Electron energy distribution function versus energy (reference to the Fermi-edge) taken with the gold film excited by (a) 120 $\mu\mathrm{J/cm^2}$ and (b) 300 $\mu\mathrm{J/cm^2}$ absorbed laser fluence at various time delays. The dashed line is the best Fermi-Dirac distribution fit with the corresponding electron temperatures are shown above the figures. All the figures are drawn in log scale to better shown the hot electrons distribution above the Fermi-edge. (figure reproduced from Ref. [30])

frequency-doubled to 337 nm and subsequently frequency-mixed again with the 674 nm to generate 5.52 eV photons. The work function of the gold film is only 5.1 eV, and hence the 5.52 eV photons will have high enough photon energy to photoeject electrons close to the Fermi-edge.

Figure 1.8 shows the energy spectra near the Fermi-edge of the gold film at various pump-probe time delays. By first normalizing the spectrum to the joint density of states of the gold film, the resulting spectra fits nicely with a Fermi-Dirac distribution function at various temperatures. The results indicate that the surface electrons can be excited by ultrafast pulses to very high temperatures (thousands of K), and this temperature cools rapidly through relaxation with the lattice in a relatively short time (within 1 ps). In addition, for long time delays, the data can be fitted nicely by the Fermi-Dirac function. However, for time delays within the first one picosecond in particular, significant discrepancies happen at the energy region above the Fermi-edge where “hot” or nonthermal electrons exist. Because of the rapid excitation process, these hot electrons cannot be described by a Fermi-Dirac energy distribution, which is only valid when the physical system is in thermal equilibrium.

The creation of these hot electrons can be explained by the the rapid heating of ultrafast pulses, which rapidly increase the energy of the excited electrons by a value corresponding to the photon energy. Since the electron relaxation time is longer than the excitation pulse, the hot electrons will take some time before they can equilibrate to a Fermi-Dirac distribution. When these highly-excited hot electrons tunnel to the unoccupied states of the adsorbates, they subsequently provide energy for the nonconventional “femtochemistry”

observed on metal surfaces.

1.5 Ultrafast optical methods for surface dynamics investigation

Purely optical methods can also be applied to investigate chemical dynamics on metal surfaces. These methods are particularly useful to understand the bonding character of adsorbates, and the vibrational modes of the adsorbate-surface interaction. In this section, two methods will be discussed that exemplify current developments in these investigations.

1.5.1 Probing desorption dynamics with surface second harmonic generation

In Sec. 1.1, two pulse cross-correlation techniques were used to identify if desorption on metal surfaces is due to photo-induced or hot-electron-induced heating. This was done by observing the cross-correlation width of the desorption peak. However, the timing information of how long it takes for adsorbates to actually desorb from the metal surface is not probed using this technique. J. A. Prybyla *et al*. have demonstrated that it is possible to measure this desorption time directly by using surface second harmonic generation. They estimated the upper limit of the desorption time of CO adsorbed on Cu(111) to be 325 fs when excited by an 2 eV photon energy, 100 fs pulse-width and 4.5 mJ/cm^2 fluence pulse [34].

Figure 1.9(a) shows how the second-harmonic probe signal depends on a continuous CO dosing rate (the ambient pressure is $P_{\mathrm{CO}} = 5 \times 10^{-8}$ torr). In general, the second-harmonic signal decreases as the CO coverage increases on the copper surface, with the second-harmonic signal becoming constant when the copper surface reaches the saturation coverage. Then, a 100fs, 4.5 mJ/cm^2 laser pulse desorbs the CO molecules from the

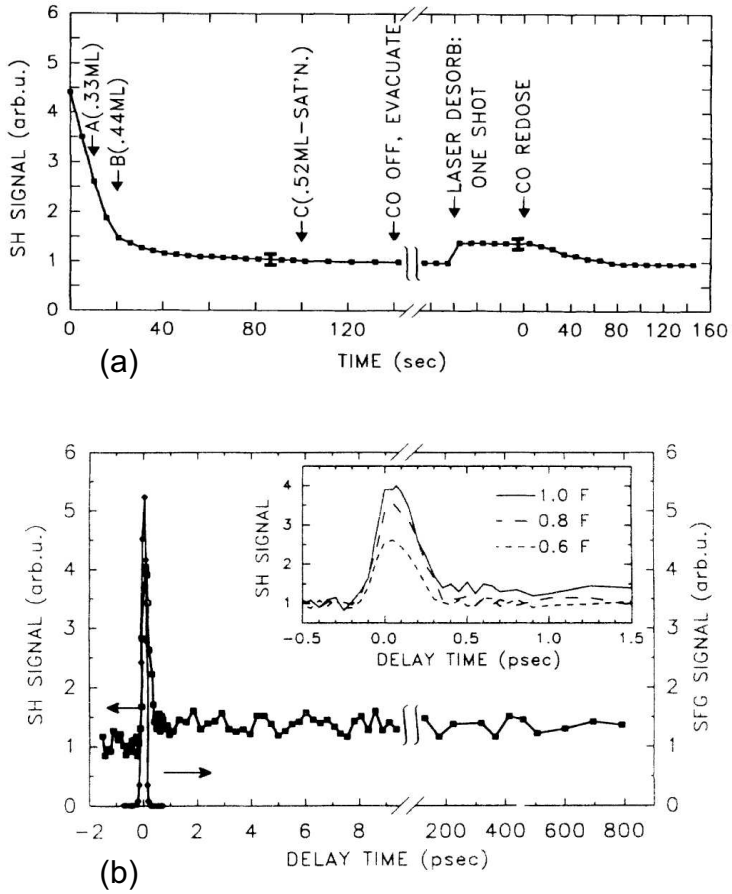

Figure 1.9: (a) Second harmonic signal versus CO exposure where the Cu(111) surface is under an ambient pressure of $P_{\mathrm{CO}} = 5 \times 10^{-8}$ torr. A single laser shot with fluence of 4.5 mJ/cm^2 to desorb CO molecules from the copper surface. Notice that the second harmonic signal decrease when the surface has higher CO coverage. (b) Second harmonic probe signal versus time delay after CO desorption induced by an ultrafast pump pulse with fluence $F = 4.5$ mJ/cm^2. The autocorrelation of the pump pulse is also shown in the figure. Inset: Same data (solid line) on expanded time scale, along with two other fluences. (figure reproduced from Ref. [34])

copper surface. Because of the reduction of the CO coverage, the second-harmonic signal increases, as expected. After CO molecules re-dose the surface to the saturation coverage, the second-harmonic signal again reduces to the previous saturation level.

A pump-probe geometry has been setup to observe the desorption time-scale for the CO/Cu(111) system, and Fig. 1.9(b) shows the corresponding results. The spike in the second-harmonic signal near zero time delay is due to the sum-frequency response of the pump-probe autocorrelation. The probe second-harmonic signal then falls to a constant baseline at a time delay of 350 fs, which is persistent and at the same level of the Fig. 1.9(a). In general, the second-harmonic response is due to both the desorption of CO molecules from the surface and to electronic excitation of the surface. As soon as the electronic excitation response is over, a constant baseline means the desorption event is also over, implying that the upper limit for such the time scale of a desorption process is about 350 fs.

1.5.2 Time-resolved vibrational sum-frequency generation

Section 1.3 discussed that 2PPE is a very useful tool in determining the transient electronic properties and even adsorbate atomic motions. On the other hand, atomic/molecular vibrational information is also valuable in understanding chemical reactions. Vibrational information, however, has not yet been obtained through this method or photoemission related techniques. Other methods are needed.[1] The vibrational information can be obtained by using surface sum-frequency generation (SFG) on CO/Ru(111), as demonstrated by G. Ertl and his co-workers [16, 35, 36]. On metal surfaces, since the inversion symmetry

[1] In chapter IV, I will show that time-resolved ultraviolet photoemission spectroscopy can be used to obtain vibrational information.

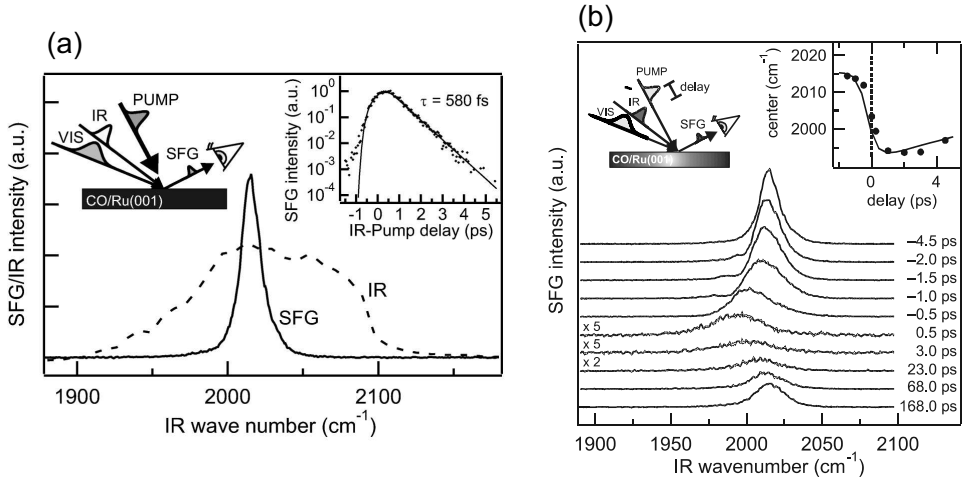

Figure 1.10: (a) SFG spectrum of the C-O stretching vibration of CO/Ru(111) at 340 K and the spectrum of the 150 fs broadband IR pulse (dashed line). Left inset: illustration of time-resolved vibrational sum-frequency generation. (see text) Right side: free induction decay of this vibration exhibiting exponential decay with $\tau = 580$ fs, indicating a homogeneous linewidth of 9.2 cm^{-1}. (figure taken from Ref. [35]) (b) Transient SFG spectra of the C-O stretch vibration after excitation with 800 nm/100 fs pump pulses with a fluence of 55 J/m^2, starting at a temperature of 340 K and coverage of 0.33 ML. (figure reproduced from Ref. [36])

of the metal lattice is broken on the surface, the second-order non-linear susceptibility is nonvanishing at the metal interface of centro-symmetry materials [37, 38]. Hence, sun frequency generation can occur at surfaces, and the measured nonlinear susceptibilites are related to the molecular dynamics at the surface.

The left inset of Fig. 1.10(a) illustrates the basic idea behind time-resolved vibrational sum-frequency generation (fs-SFG). An ultrafast pulse illuminates the adsorbate-surface system to excite an adsorbate vibrational mode. The excited adsorbates then either desorb from the surface, or vibrate under a free induction decay time to release its vibrational energy to the metal surface. Another pair of laser pulses subsequently probes the surface, one of the two pulses is spectrally filtered to 4 cm^{-1} at 800 nm, and hence corresponds

to a long pulse (>ps). The other pulse is a broad band infrared pulse (spectrum shown in Fig. 1.10(a)) with a pulse width of 150 fs. The broad band infrared pulse serves as a "white light" source to scan for the frequency of the excited C-O stretching vibrational mode, with the narrow band 800 nm pulse used for sum-frequency-generation of the SFG signal. Since the resulting SFG signal ($\omega_{SFG} = \omega_{VIS} + \omega_{IR}$) results from the multiplicity of the two pulses spectrally, it is also a narrow band signal, and hence it can be used to identify any spectral shift of the C-O stretch mode due to ultrafast excitation. Temporally, since the SFG generation only happens when the two pulses arrive on the surface, the pulse width of the broad band infrared pulse determines the time-resolution of the probe SFG. Therefore, adsorbate vibrational dynamics can be probed with femtosecond resolution.

The transient dynamics of CO on a Ru(111) surface, excited by 800 nm/110 fs pump pulses, is shown in Fig. 1.10(b), where the sample temperature is at 340 K, and the surface is re-dosed using CO background pressure of $P_{\mathrm{CO}} = 5 \times 10^{-6}$ mbar. The C-O stretch vibration displays a very strong transient red-shift, as well as a broadening and decrease in integrated intensity. The red-shift is the result of anharmonic coupling of the C-O stretch to low-frequency frustrated modes [39]. The intensity of the SFG signal at $\tau_{\mathrm{delay}} = 168$ ps is roughly half of the initial intensity, demonstrating that a large number of CO molecules desorb after excitation by the pump pulse.

1.6 Conclusion

This chapter has presented a synopsis of work to date of observing adsorbate dynamics on metal surfaces. These techniques have revealed much valuable information to help understand how adsorbates behave on metal surfaces on molecular time scales. The ulti-

mate goal of tracing a complete chemical reaction process from the start to the end and identifying all the intermediate states and their corresponding reaction time scales remains to be done. Therefore, the development of new techniques to reveal complete adsorbate dynamics is increasingly important in the field of surface chemical physics. In this thesis, I explore the potential of "Time-Resolved extreme Ultraviolet Photoemission Spectroscopy" (TR-UPS) to elucidate surface chemical reaction dynamics. Preliminary results will be discussed that demonstrate the effectiveness of this technique for observing molecular motion on surfaces.

CHAPTER II

Time-Resolved Extreme-Ultraviolet Photoemission Spectroscopy

In conventional surface analysis, x-ray photoemission spectroscopy (XPS)[1] and ultraviolet photoemission spectroscopy (UPS) are standard methods for analyzing metal surfaces. These methods have proven to be powerful in characterizing metal surfaces, and UPS is especially important for obtaining information about molecules adsorbed on metal surfaces. Photons in the extreme ultraviolet and soft x-ray regimes (50 to 200 eV) are of particular importance in probing metal surfaces. This is due to the fact that the mean free path of photoemitted electrons excited by these photons is extremely short in metals (only about 5 to 10 Å); hence, only electrons originating from the top several mono-layers will be detectable [2]. These photons can be generated using synchrotron radiation or laboratory-size x-ray and ultraviolet light sources.

A long standing goal of chemical physics has been to follow a chemical reaction from beginning to end, while identifying all the intermediate steps. However, conventional UPS techniques are incapable of doing this due to the limitations of the light source used. State-of-the-art – or so called third generation – synchrotrons cannot provide light pulses

[1] In chemistry literature, XPS often is referred as Electron Spectroscopy for Chemical Analysis (ESCA).

shorter than tens of picoseconds duration, despite the high photon flux that can be obtained. Since molecular motion (vibrational, rotational, and translational) on metal surfaces is estimated to occur on sub-picosecond time scales, the development of innovative ultrafast light sources that provides EUV pulses with femtosecond duration will provide crucial tools for future investigations.

Several approaches for generating ultrafast EUV light are currently being pursued, including "slicing" synchrotron radiation bunches with femtosecond lasers, Thomson scattering from an electron beam [40, 41, 42], free-electron lasers (FELs) [43, 44, 45], and high harmonic generation techniques. FELs should be capable of generating EUV pulses with sub-picosecond pulse width and extremely high intensity. Practical implementations are still lacking, however, as these technologies are extremely difficult and expensive [46].

A very successful approach to obtaining ultrafast EUV pulses is high harmonic generation. Harmonic generation has a long history – optical frequency doubling was first demonstrated by using a ruby laser and a quartz crystal in 1961 [47]. Since then, techniques for up-converting photons to higher energies have attracted significant attention. In the last decade, the use of harmonic generation for EUV generation has been a topic of extensive investigation, with the demonstration of very high ($> 100^{th}$) order nonlinear processes [48].

2.1 High Harmonic Generation

Ultrafast laser technology has progressed rapidly during the last two decades. In particular, the invention of the ultrafast Ti:Sapphire laser is of great importance [1, 49]. Not only is it an all solid state laser system and therefore relatively easy to use, but furthermore,

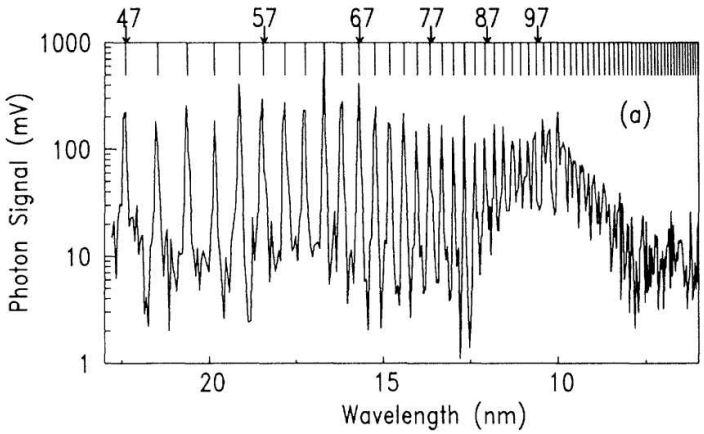

Figure 2.1: High harmonics generated in neon gas at 40 torr with a 1 ps duration, 1.053 μm Nd laser pulse at an intensity of 1.5×10^{15} W/cm^2. (figure reproduced from Ref. [50])

the laser pulses generated by Ti:Sapphire oscillators can straightforwardly be amplified using subsequent laser amplifiers. Therefore, table-top size, sub-terawatt class Ti:sapphire laser systems have been constructed and are in use in many laboratories around the world. When these intense laser pulses are focused into a gas medium, the interaction between the strong optical field and the gas atoms produces strong nonlinear-optical effects. One of these effects is the production of optical photons with frequencies corresponding to the odd harmonic orders of the original pulse. The wavelengths of these high harmonic generated (HHG) photons spread across the ultraviolet, the extreme ultraviolet, and the soft x-ray regions of the spectrum. Furthermore, since the high harmonic generation process is a coherent process, the generated photons are highly coherent. This coherent property is important for many physical experiments.

A typical high harmonic generated spectrum produced by an intense ultrafast pulse focused into a noble gas media is shown in Fig. 2.1. The major features of the spectrum are a plateau at low photon energy, and a “cutoff” corresponds to the maximum achiev-

able photon energy. Beyond the cutoff energy, the intensity of the HHG falls rapidly. The emitted spectrum is not continuous, but features discrete harmonic peaks whose energies correspond to the odd harmonic orders of the driving laser. The high harmonic generation process can be explained using a strong field laser-atom interaction model, in which the linearly polarized electric field suppresses the electric field binding electrons to the interacting gas atom [51, 52, 53]. This allows the atom's valence electrons to tunnel out of its attractive potential and into free space, as shown in Fig. 2.2(a). The freed electrons are then accelerated to a very high kinetic energy by the strong electric field of the ultrafast pulse. After a half optical cycle, the ultrafast pulse reverses its electric field, and the electrons are forced to reverse their course. They may then recombine or scatter with the atomic core if their trajectory approaches the parent ion. The high impact energy of this collision causes them to release this kinetic energy into a high energy photon, as shown in Fig. 2.2(b). Since the electrons undergo this process in a very short timespan, the duration of the generated pulses is equally short, on the order of a half cycle of the driving pulse, although the total emission may consist of a train of such pulses. Furthermore, since the electrons from different atomic cores undergo coherent acceleration from the driving pulse, the generated photons are coherent in nature.

Due to the total symmetry of the gas atoms, the generated photons are the odd harmonics of the driving pulse, and extend to the cutoff frequency ω_{max}. Theory predicts a ω_{max} corresponding to the acquired kinetic energy plus the atomic binding energy

$$\hbar\omega_{max} \simeq I_p + 3.2U_p \tag{2.1}$$

where I_p is the ionization potential of the gas atom, and U_p is the cycle-averaged kinetic

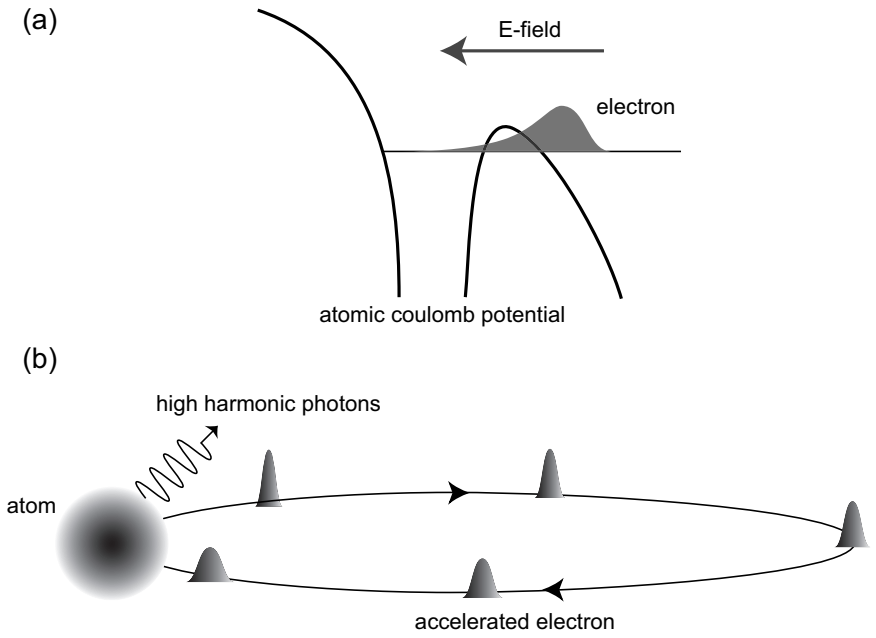

Figure 2.2: In the semi-classical picture, (a) the atomic coulomb potential is disturbed by the laser electric field, and the electron wave packet tunnels through the weaken potential barrier to escape. (b) The electron wave packet enters the free space "continuum" and continue to accelerate in the laser field. On the subsequent half cycle, the electron is decelerated and turns around to be accelerated towards the parent ion. The electron with high kinetic energy then scatters with the parent ion to generate high harmonics.

energy of the electron in an electric field E_0 and frequency ω_0, generally called the pondermotive potential. U_p can be written out as

$$U_p = \frac{e^2 E_0^2}{4m\omega_0^2} = \frac{2\pi c r_e I_L}{\omega_0} \tag{2.2}$$

where I_L is the laser field intensity, and $r_e = e^2/4\pi\epsilon_0 mc^2$ is the classical electron radius. To achieve as high a cutoff energy as possible, noble gases, with their higher ionization potentials, are typically used in the high-harmonic generation process. For example, helium's ionization potential is 24.5 eV, and for a laser intensity of 10^{15} W/cm^2 with a 800 nm wavelength, $\omega_0 = 2.4 \times 10^{15}$ rad/s and $r_e = 2.8 \times 10^{-13}$ cm, so $U_p \simeq 60$ eV. Therefore, using Eq. 2.1, the theoretical maximum generated photon energy is about 220 eV for those conditions. Currently, the record for high harmonic generation is the 229^{th} harmonic (2.7 nm or 450 eV) [3].

To generate "bright" high harmonic pulses, harmonic photons generated at different points in the nonlinear medium have to interfere constructively; otherwise, the generated photons will convert back to the fundamental wavelength. Therefore, extending the medium length does not automatically result in higher output flux. To illustrate this point, for second-order harmonic (2ω) generation in a nonlinear medium, the generated photon intensity can be written as:

$$I_{2\omega} \propto \frac{\sin^2(\Delta k\, L/2)}{(\Delta k\, L/2)^2} = \mathrm{sinc}^2\left(\frac{\Delta k\, L}{2}\right) \tag{2.3}$$

where L is the length of the non-linear media, and

$$\Delta k = 2k_\omega - k_{2\omega} = \frac{2\omega}{c}\left(n_\omega - n_{2\omega}\right) \tag{2.4}$$

where k_ω (n_ω) and $k_{2\omega}$ ($n_{2\omega}$) are the wave vector (index of refraction) of the nonlinear medium at wavelengths ω and 2ω, respectively.

Since Eq. 2.3 is a sinc function, it reaches its maximum when $\Delta k = 0$. Therefore, in order to achieve maximum output intensity for a given harmonic, the wave-vectors (2 of k_ω and a $k_{2\omega}$) of the fundamental and harmonic light must cancel out. Eq. 2.4 expresses this "phase-matching" condition for harmonic generation.

For second order harmonic generation, the phase matching condition is easy to achieve, either by temperature-controlling the non-linear medium, or by using a nonlinear crystal and rotating the crystal to the so-called "phase-matching" angle. The idea of both techniques is to achieve equal values for both n_ω and $n_{2\omega}$, in order to satisfy the phase-matching condition. However, phase-matching harmonic generation for high-orders is not so trivial since one cannot use the material birefringence. Furthermore, in the case of HHG, the medium is unavoidably adsorbs much of the generated signal. Therefore, high harmonic generation generally suffers from low output photon flux.

In a typical high harmonic generation setup, a pulsed gas nozzle creates a well-defined region of noble gas inside a vacuum chamber. The gas nozzle pulses synchronously with the incoming focused laser pulses to generate the harmonic light. The reason to use a pulse valve to generate harmonic light is to avoid absorption from the noble gas. However, with such a design it is difficult to achieve high fluxes of the harmonics since harmonic photons are generated in a very limited region with varying pressure.

An innovative design has been implemented in our laboratory using a hollow-core capillary to achieve phase-matching conditions for high harmonic generation. Fig. 2.3

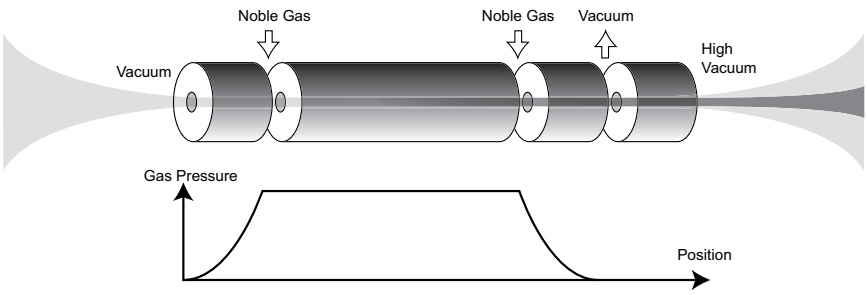

Figure 2.3: Schematic diagram of the hollow-core fiber used to generate the 27^{th} harmonic (42 eV) probe pulse in this experiment. The driving ultrafast beam is drawn in light color and the generated high harmonic beam is in dark color. The fiber has four sections, and the long one is the main harmonic generation region. The noble gas is introduced to the capillary through the gap between the first and second, second and third sections (from the left). The design of having the first and the third short sections sandwiched between the second long section is to maintain a constant pressure at the second section where the high harmonic generation happens. The fourth short section is optionally installed for differential pumping purpose. The inner diameter for all the fibers is 150 μm. The capillary length of all the short sections is 1 cm, and the length for the long section is 8 cm.

shows a schematic illustrating the high-harmonic capillary setup. The long center piece of the hollow core capillary is filled with noble gas. The wave-vector k of the laser beam can be written in the following form when it is traveling inside the capillary [4]

$$\begin{aligned} k(\lambda) &\approx \frac{2\pi}{\lambda} + \frac{2\pi P(1-\eta)\delta(\lambda)}{\lambda} + (1-\eta)n_2 I \\ &\quad -P\eta N_{atm} r_e \lambda - \frac{u_{11}^2 \lambda}{4\pi a^2} \end{aligned} \tag{2.5}$$

where the terms, from left to right, correspond to the contributions from vacuum, neutral gas dispersion, non-linear refractive index, plasma dispersion, and waveguide dispersion. The symbols P, η, N_{atm}, $\delta(\lambda)$, r_e, n_2, I, a and u_{11} represent the pressure in atmospheres, the ionization fraction, the number density at one atmosphere, the neutral gas dispersion, the classical electron radius, the nonlinear refractive index, the laser pulse intensity, the radius of the capillary, and $u_{11} = 2.405$ is the first zero of the Bessel function J_0. The

important point here is that the wave-vector k depends on the pressure P, driving pulse intensity I, and the capillary radius a; therefore, the magnitude of the wave-vector k can be controlled by changing these parameters. The phase matching condition for the q^{th} harmonic generation becomes

$$\begin{aligned} \Delta \mathrm{k} &= k_q - q k_f \\ &= q k_0 \left[n(\lambda_q) - n(\lambda_0) \right] \\ &\approx q \frac{u_{11}^2 \lambda_0}{4\pi a^2} + N_e r_e (q\lambda_0 - \lambda_q) - \frac{2\pi N_a}{\lambda_a} [\delta(\lambda_0) - \delta(\lambda_q)] \end{aligned} \tag{2.6}$$

Therefore, phase-matching for high-harmonic generation can be achieved by "confining" noble gas molecules in a capillary. The high harmonic flux generated in this geometry is estimated to be 10^8 photons/pulse/harmonic at 42 eV in the experimental setup used in this thesis.

One of the favorable properties of the high harmonic source with a hollow-core capillary is that the spatial mode of the generated harmonic beam is rather Gaussian in shape. This allows experimenters to focus the harmonic beam into a small spot size for the investigation of physical phenomena on a microscopic scale (nm in principle), as will be discussed in Sec. 2.2.1. Another desirable property of the high harmonic beam is its spatial and temporal coherence, as pointed out in the previous paragraph. Although UPS generally does not require a coherent source, coherence is a valuable property in many physical investigations. Since pulses generated by synchrotrons are not coherent, high harmonic generation light is not only a convenient replacement of the synchrotron radiation, but unique properties, such as coherence and sub-femtosecond pulse width.

2.2 Time-resolved extreme ultraviolet photoemission spectrometer

The basic method of obtaining time-resolved information of physical phenomena is well understood and has been implemented in a variety of physical investigations. One basic method used to measure physical transients is the "pump-probe" technique. A laser pulse is introduced into the system, which starts a physical process. Another laser pulse is then sent into the system after some time-delay Δt with respect to the first pulse. This second pulse "probes" the status of the system of that moment. Various signals can be measured, including changes of the material reflection and absorption. After probing the system at several time delays and comparing changes among the spectra, a dynamic picture of the physical process is mapped out. Although the idea of pump-probe spectroscopy is simple, measuring the dynamics of surface chemical reactions had not been performed until now. This can now be done by combining two different technologies (UPS and HHG) into one.

The "Time-Resolved extreme Ultraviolet Photoemission Spectrometer" (TR-UPS) that I have constructed is shown in Fig. 2.4. The system consists of two major components – an ultra-high vacuum (UHV) chamber and a pair of IR pump/HHG probe beam lines.

2.2.1 Pump - HHG Probe beam line

As shown in Fig. 2.4, an amplified Ti:sapphire laser system is used as the light source in this experiment. The laser can generate a laser fluence of 1.5 mJ/pulse at a 2 kHz repetition rate. The pulse width is measured to be 22 fs by frequency resolved optical gating (FROG) [54]. The laser beam is directed to a beam splitter, which separates the laser beam into two different pulses – 80% of the laser beam energy will be used as the

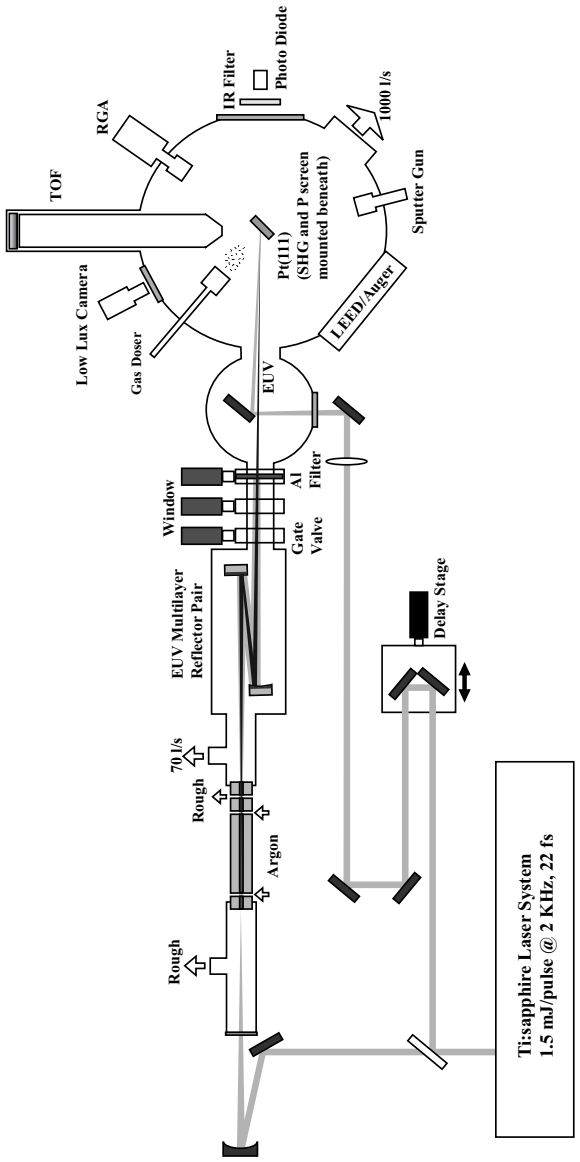

Figure 2.4: Schematic drawing of the time-resolved ultraviolet photoemission spectroscope. The pump beam is the beam line drawn at the lower part of the figure; the probe beam is drawn at the upper part of the figure, and it goes through the hollow-core capillary to generate high harmonics. The main chamber is under ultra-high vacuum condition at all times ($\sim 10^{-10}$ torr), and a gate valve is used to separate the main chamber from the rest of the system. The multilayer mirror chamber and the beam line are under high vacuum ($\sim 10^{-6}$ torr) condition.

probe, and 20% of the energy becomes the pump. The probe energy will be used for the high harmonic generation process to convert photons in the extreme ultraviolet, and the energy of the resulting EUV pulses will be much less then the energy of the pump beam.

The time delay between the pump and probe beams is varied by using a translation stage in the pump beam. A micro-stepping motor with nanometer step resolution is mounted to the translation stage to give a time delay resolution of better than 1 fs.[2] The pump beam is then loosely focused into the UHV chamber and subsequently redirected to the sample. The target position of the pump beam on the sample can be readily adjusted by tweaking the mirror mounts outside the vacuum chamber.

For the probe beam, a hollow-core capillary is used to generate high harmonics. Argon gas is used as the nonlinear media for all the experiments discussed in this thesis. The targeted harmonic used in these experiments is the 27^{th} harmonic of the driving 800 nm ultrafast pulses (42 eV in photon energy or 30 nm in optical wavelength). As discussed in Sec. 2.1, harmonic generation produces a semi-continuum spectrum, so frequency discrimination is needed in order to be used in UPS. Traditionally, curved gratings are used for this purpose; however, this scheme suffers from the fact that the reflectivity of the grating of this wavelength is extremely low and the grating itself is difficult and expensive to fabricate. To make matters worse, in order to maintain the sub-picosecond pulse width of the harmonic, two gratings are needed to form a zero-dispersion imaging system [55, 56]. This further reduces the already low reflectivity of the grating spectrometer. In order to avoid this problem, a pair of multi-layer mirrors is used in our setup. This pair of multi-layer mirrors is made by periodically growing silicon and molybdenum thin-films

[2]The translational stage moves 150 nm to increase or delay 1 fs.

on a super-polished glass substrate to form a Bragg reflector for the incoming EUV photons. The wavelength with the maximum reflectivity is equal to twice the thickness of the Si/Mo stack of the multi-layer mirrors, and the combined reflectivity of the two mirrors is shown in Fig. 2.5. The wavelength of the maximum reflectivity of the multi-layer mirrors is near the 27^{th} harmonic, with a little less than 4% total reflectivity. The adjacent harmonics (25^{th} and 29^{th}) save only 0.5% reflectivity, which effectively filter out these harmonics. The rear multi-layer mirror has a radius of curvature of one meter; hence the multi-layer mirrors also have the benefit of focusing the 27^{th} harmonic onto a small spot of the sample. Fig. 2.6 shows the image of the focal spot of the 27^{th} harmonic. This image is taken by placing a phosphor screen at the sample position, then recording the phosphor fluorescence. The spot size is measured to be 400μm with a Gaussian profile. The spot size is large because of the long focal length of the curved multi-layer mirror used, and because the sample is not placed exactly at the focal position for convenience. Despite this, the EUV spot size is still small enough for use in photoemission experiments. The infrared pump beam spot size is arranged to be several times bigger than the EUV spot size, to ensure that the probing region of the sample is uniformly illuminated.

A 200 nm thick aluminum filter is inserted between the UHV chamber and the beam line. The transmission of this filter at 42 eV is calculated to be 63% [57]. However, due to the formation of an oxide layer on the surface, the transmission is more typically $\sim 10\%$. The aluminum filter is retracted when the experiment is not running, and a gate valve is shut to separate the beam line from the UHV chamber. The aluminum filter serves two purposes. Firstly, the driving 800 nm pulse is completely reflected by the filter, while the

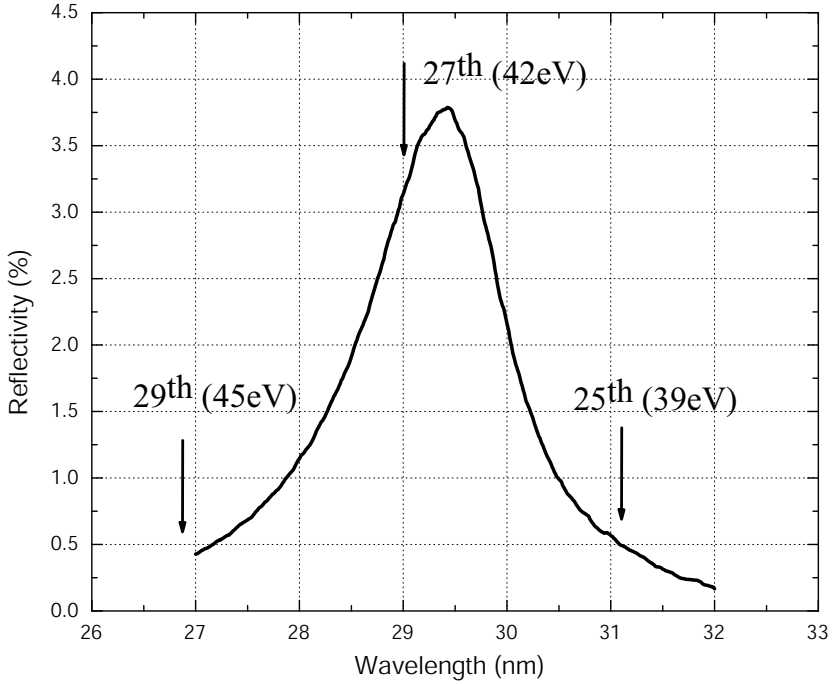

Figure 2.5: Combined reflectivity of the Si/Mo multi-layer mirror pair (2 mirrors) used in the TR-UPS setup. The reflectivity of the mirrors are measured by the synchrotron radiation facility in Lawrence Berkeley laboratory.

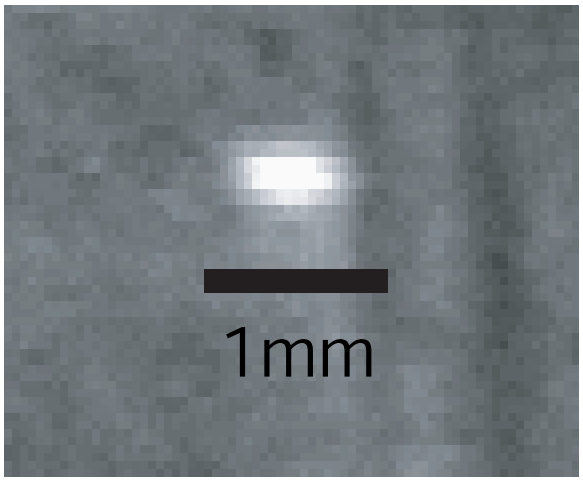

Figure 2.6: The image of the 27^{th} harmonic fluoresce at a phosphor screen. The phosphor screen is mounted beneath the platinum sample, and the phosphor screen was raised to the sample position when this picture was taken. The image was capture by a low-lux, high sensitive camera mounted outside the UHV chamber and looking in through a view port. The spot size of the harmonic is measured to be 400 μm. The spot seems elliptical because the phosphor screen is at 45 degrees with respect to the incoming EUV beam.

harmonics pass through and enter the main chamber. Secondly, the filter is mounted on an air-tight gate valve, which maintains the ultra-high vacuum in the main chamber.

The number of photons that reaches the sample can be calculated using the overall transmission: $10^8 \times 4\% \times 10\% \approx 4 \times 10^5$ photons for the 27^{th} harmonic, with about a 1 eV energy bandwidth.

2.2.2 Ultra-high Vacuum Chamber

The UHV chamber is pumped by a 500 l/s turbo pump (Balzers TMU-520-SG) and a 270 l/s ion pump (Varian VacIon Plus 300 noble diode) to achieve a base vacuum pressure of under 1×10^{-10} torr after a standard UHV bake out. To prevent the earth's magnetic field from penetrating into the vacuum chamber, the chamber is shielded internally by double layers of μ-metal. This prevents the course of photoelectrons from being distorted by external magnetic fields. A platinum(111) single crystal is mounted inside the chamber by spot-welding it onto two parallel tantalum heating wires, which are in turn spot-welded to a manipulator mounted vertically from the top port of the chamber. The manipulator has the capability of performing three-axis translational and azimuthal rotational motion with respect to the platinum sample. In addition, the manipulator's inner tube can be filled with liquid nitrogen, providing cooling of the sample. A high current power supply (HP 6269B) is connected to the manipulator and drives the tantalum wires that heat the platinum sample. A proportional-integral-derivative (PID) temperature controller (Omega CN77000) controls this power supply. A K-type thermalcouple is also spot-welded to the back of the platinum sample for measuring the sample's instantaneous temperature. The measured temperature feeds into the PID temperature controller as a feedback signal to control the

high current power supply. Using this feedback control scheme, the electrical heating can be nicely balanced by the liquid nitrogen cooling; therefore, the sample temperature can be reliably controlled over a wide temperature range, from 77 to 1200 K, and the temperature can be increased or decreased at a rapid rate.

A custom-built time-of-flight (TOF) electronic kinetic energy analyzer is used for detection. Two shielding layers of μ-metal are also installed around the inner wall of the TOF tube to insulate it from the earth's magnetic field. The total tube length is $L_{tube} = 600$ mm and the inner diameter is 40 mm, which provides an electron collection solid angle of $S \simeq 2 \times 10^{-3}$ sterradians. At the end of the TOF tube, a custom-built large area (40 mm) fast-response detector detects the electrons. A double micro-channel plate (MCP) is used at the front of the detector to obtain the gain necessary to detect single electrons. The MCPs amplify the single electron signal by a secondary electron cascade process to detectable signal levels ($\sim$ 100 mV). The detector has timing resolution of about 200 ps. Impedance matching of the whole electron detector allows it to operate with a GHz frequency bandwidth. The key ideas of impedance matching are adapted from the design of A. Stolow [58], and a cone-shape anode design ensures that the fast electronic signal propagates into the coaxial cable with no noticeable reflection. Figure 2.7 shows the output signal when an electron arrives at the detector. The signal has a rise time of less than 1 ns and a pulse width of less than 2 ns. The signal is clean, without noticeable reflection. This is crucial to the detection of multiple incoming electrons. The output signal is subsequently delivered to a high frequency pre-amplifier followed by a constant fraction discriminator (EG&G ORTEC 9327), ensuring that the electron arrival time is independent

of output signal intensity fluctuations. An all solid-state time-to-digital converter (TDC) (ACAM AM-F1) measures the electron flight times, referenced to a start signal from the ultrafast laser system. The real electron flight time is actually referenced to the moment when the EUV pulse arrives at the sample, also the moment when the sample starts to emit electrons. This moment appears on the TOF spectrum as an EUV scattered light peak. This peak is a result of the EUV pulse being scattered/reflected from the sample surface, with the scattered EUV light then triggering the detector. Actually, there is a 2 ns time delay between this EUV peak and the real start time, resulting from the propagation of the EUV light to travel from the sample to the detector. This time difference is neglectable due to the fastest photoelectron needs to take more than 100 ns to reach the detector. By subtracting the time of the EUV "start peak" from the measured flight time, the actual electron kinetic energy E_{kin} can be calculated by the following equation

$$E_{kin} = \frac{1}{2} m_e (\frac{L_{tube}}{t_f})^2 \tag{2.7}$$

where m_e is the electron mass, t_f is the subtracted electron flight time.

If the electron emission is assumed to be evenly distributed over the 2π solid angle (half sphere) for rough estimation, the count rate of photoelectron detection C_R (electrons/second) can be calculated using

$$C_R = \frac{S}{2\pi}(1-R) I \cdot \alpha \cdot D \cdot L_{rep} \tag{2.8}$$

where $S = 2 \times 10^{-3}$ is the solid angle of the TOF, $I = 4 \times 10^5$ is the incoming photon number per pulse, R is the reflectivity of the sample, and $L_{rep} = 2$ kHz is the ultrafast laser repetition rate. $\alpha \simeq 8\%$ is the photoelectric yield of platinum surface at 30 nm [59, 60]. D

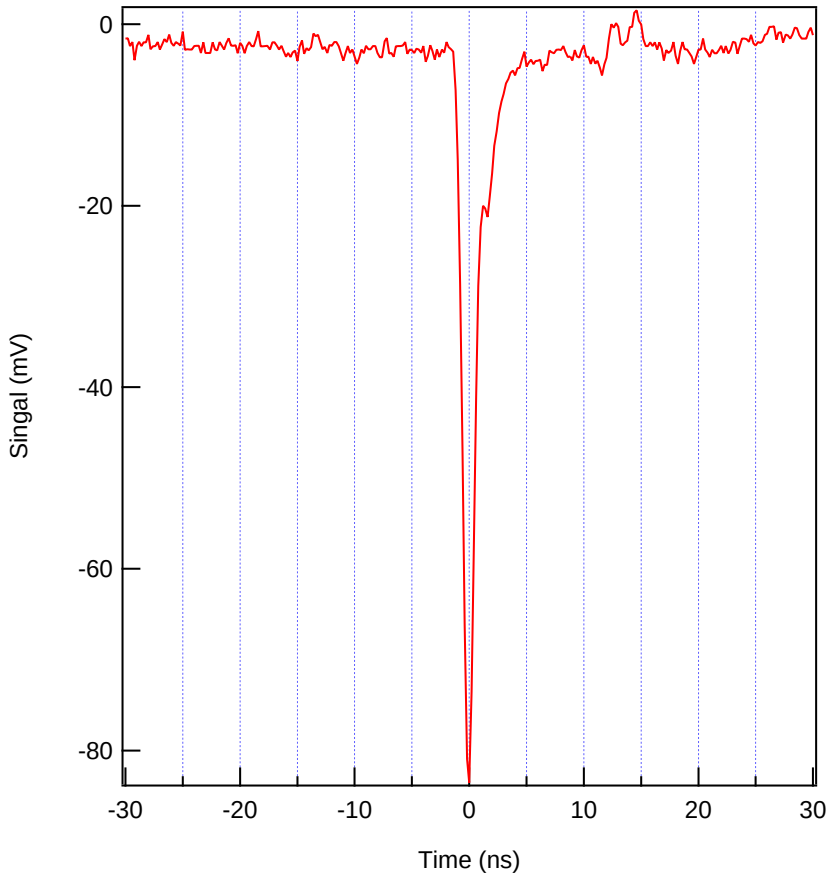

Figure 2.7: The output signal of the impedance matched MCP TOF detector when a single electron hits the detector. The signal is directly measured from the detector with an oscilloscope. It is very important that there is no signal reflection or "ringing" after the main peak for high count rate electron detection.

is the detection efficiency for the MCP detector, and is measured to be $\sim 50 - 85\%$ for the electron kinetic energy range of $0.2 - 2$ keV [61]. For the platinum (111) single crystal, at an incident angle of 45 degrees, $R = 9\%$ [57]. Therefore, the estimated count rate is $C_R \approx 1.5 \times 10^4$ electrons/second, while the experimental count rate is also $C_{Rexp} \approx 1.5 \times 10^4$ electrons/second.

Figure 2.8 shows the inside of the UHV chamber. For standard surface diagnostics, the UHV chamber is equipped with a Low Energy Electron Diffraction (LEED) Spectrometer

and an Auger Electron Spectrometer (AES) (OCI BDL800IR), which monitor the sample surface's condition. The diffraction pattern of the LEED can reveal the local order of the sample surface, while surface contamination can be seen using the AES. A residual gas analyzer (RGA) (Leybold Inficon Transpector) is installed on the UHV chamber for monitoring the ambient chamber gas content. In addition, Thermal Desorption Spectra (TDS) can be taken by the RGA, measuring the partial pressure of a target molecule while the temperature of the sample is steadily raised. A TDS measurement for the O_2/Pt(111) system is shown in Fig. 3.2.

For sample preparation and cleaning, an argon ion sputter gun is installed in the UHV main chamber. The sputter gun can be used to remove the topmost several mono-layers of the platinum sample; sample surface contaminations are simultaneously removed. Rapid thermal annealing can subsequently be performed to reconstruct the surface order.

Finally, a custom-built gas doser is used for precision gas dosing. The major benefit of using a gas doser versus using a gas leak valve is that a doser allows a much higher local pressure to be created around the sample area while keeping the rest of the chamber in high vacuum. This also minimizes the opportunity for gas molecules to adsorb the UHV main chamber wall, preventing prolonged pump down times after gas dosing. In addition, if experimentally required, continuous gas dosing to the sample would not cause serious problems. Maintaining the high vacuum condition of the rest of the system is needed to ensure the functionality of other highly sensitive equipment. For example, the working pressure of the MCP electronic detector must be lower than 1×10^{-6} torr.

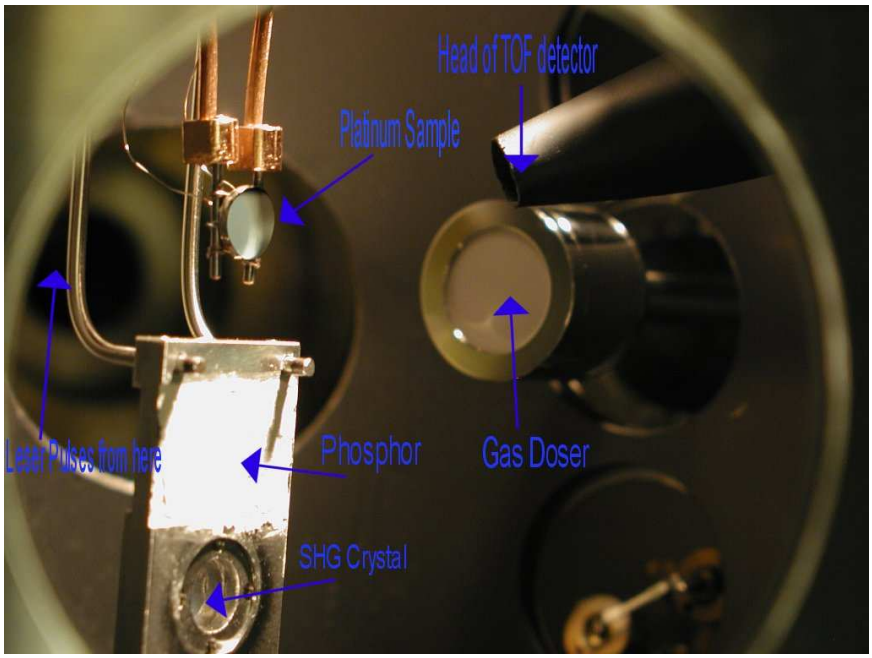

Figure 2.8: Picture shows the internal arrangement of the TR-UPS chamber. In this photo, the sample is turned 90 degrees from the normal position for better viewing. Both of the pump-probe beams are coming in from the flange at the left side of the picture to reach the metal sample.

2.2.3 Finding temporal and spatial overlap

For any pump-probe experiment to be successful, finding the temporal and spatial overlap between the pump and probe beams is critical. In this experiment, the relatively low intensity of the high harmonic generated EUV beam creates a particular alignment challenge. In addition, it is a challenge to find the temporal overlap between an EUV (probe) pulse and an infrared (pump) pulse [62]. Therefore, to routinely run this experiment, an effective method for finding both the temporal and spatial overlap is needed.

To find the temporal overlap, or so-called "time-zero", some of the infrared light used to create the EUV probe beam is allowed to enter the EUV chamber, by retracting the aluminum filter and inserting a thin sapphire window instead. The argon gas of the high-harmonic cell is turned off to reduce the pressure in the beam line. A KDP (second harmonic) crystal mounted underneath the platinum sample is now raised to the sample position, and the time-zero can then be found by looking for the second harmonic cross-correlation signal between the pump and the probe pulses. Since the aluminum filter is only 200 nm thick, the time difference between the generated EUV pulse and the driving infrared pulse reaching the platinum sample is negligible. The time difference due to the removal of the argon gas is also negligible because of the low pressure (~ 50 torr) and short length (8 cm) of the gas interaction region. However, the time difference induced by inserting a sapphire window to the infrared pulse needs to be accounted for. The thickness of the sapphire window is 355 μm, hence the time delay induced by the sapphire can be precisely calculated to be 934 fs. This time difference can be corrected for by moving the translational stage after the cross-correlation is found. Therefore, it is effective to find the

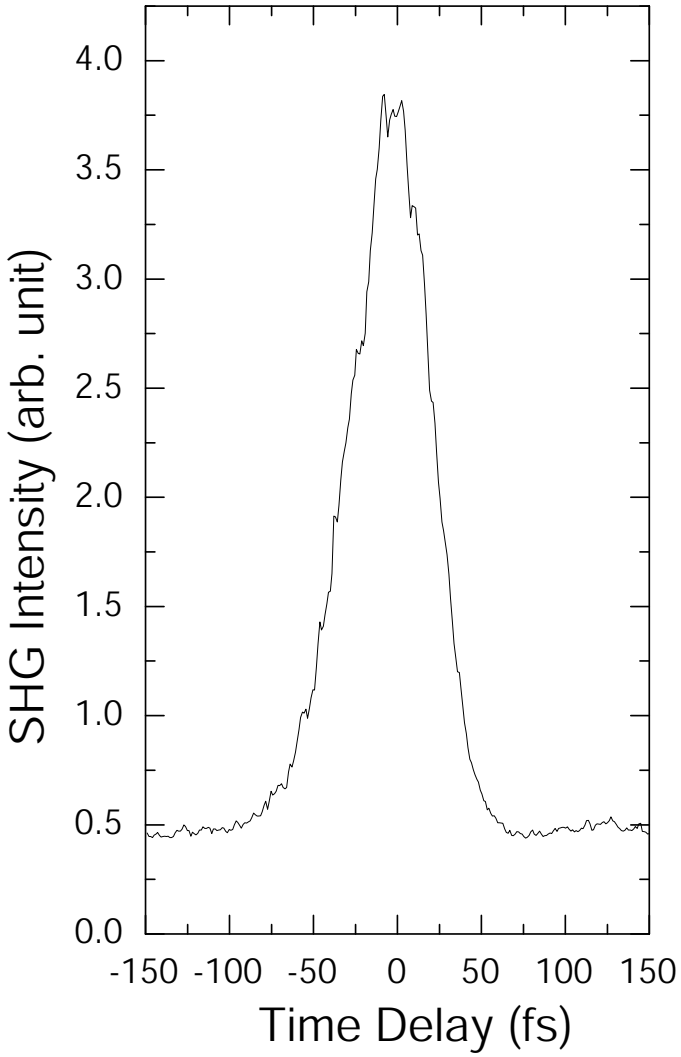

Figure 2.9: Signal of second harmonic generation between the infrared pump and probe pulses. The FWHM of the signal is 62 fs.

time-zero between the probe and pump beam without directly using the EUV pulses. A typical cross-correlation signal for the two beams is shown in Fig. 2.9.

To find the spatial overlap, a phosphor screen (P1 phosphor) mounted beneath the sample is raised to the sample position. The focused EUV spot can be imaged by a highly sensitive, low-lux CCD camera (Minitron 12V1E) mounted outside the chamber. The camera views the phosphorescence through a view port, as shown in Fig. 2.6. Since the

beam pointing of the EUV is fixed and cannot be adjusted, spatial overlap is achieved by moving the infrared pump beam location by adjusting the mirror mounts outside of the chamber. Once the spatial overlap is found, the sample is lowered back to its original position.

2.3 Conclusion

In this chapter, the implementation of the TR-UPS setup was thoroughly discussed and explained. In the following two chapters, the setup will be utilized to measure chemical dynamics of adsorbates on metal surfaces, demonstrating the power of the TR-UPS technique.

CHAPTER III

Probing the transition dynamics of chemisorbed states of O_2 on Pt(111)

3.1 O_2 states on Pt(111) surfaces

Because of its importance and relative simplicity, the O_2/Pt(111) system is considered to be the model system for catalytic chemistry, and has been investigated both experimentally and theoretically in considerable detail. Four different adsorption states of oxygen on Pt(111) have been reported to date: one physisorbed state, two chemisorbed states, and one atomic state. It is important to review some of their properties before going further on investigating dynamics of oxygen molecules on Pt(111).

3.1.1 Physisorbed State

The physisorbed state of molecular oxygen can be stably deposited on a platinum surface when the surface temperature is below 30 K. In the case of physisorbtion, charge transfer or bond hybridizaton do not occur between the oxygen molecular bonds and the platinum d-band. The force holding the oxygen molecule to the platinum surface is a van der Waals attraction; hence, the physisorbed oxygen molecules do not reside on any specific sites on the platinum surface. Multiple layers of physisorbed oxygen molecules can

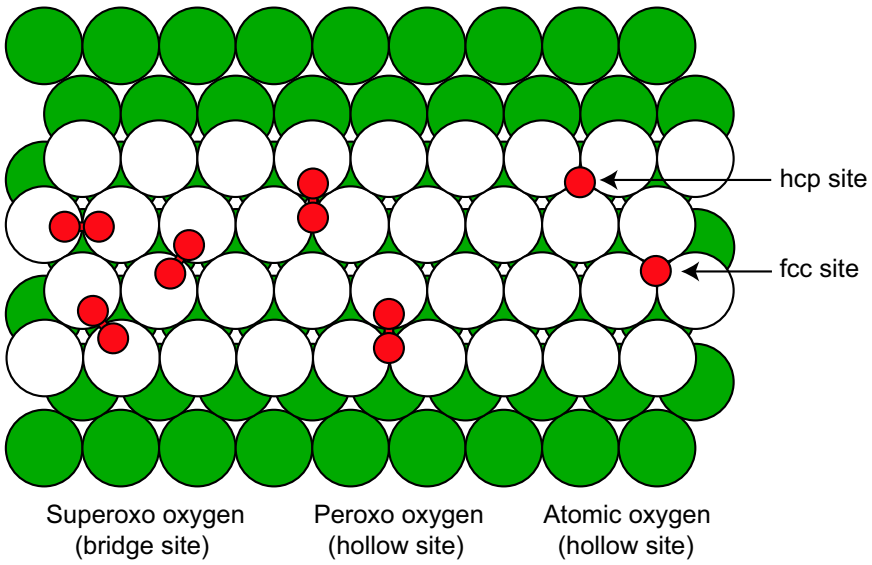

Figure 3.1: Schematic diagram of the surface configuration of oxygen on Pt (111), for the superoxo (O_2^-), peroxo (O_2^{2-}), and atomic (O) oxygen states.

reside on the metal surface, and these layers can be considered as a "condensed" phase of molecular oxygen. The electronic properties of these molecules are very similar to those of the gas-phase free oxygen molecules.

3.1.2 Superoxo and peroxo chemisorbed states

There are two different chemisorbed oxygen molecular states for the platinum (111) surface: superoxo oxygen (O_2^-), and peroxo oxygen (O_2^{2-}). When oxygen molecules are deposited on a platinum (111) surface at a temperature of about 77 K, thermal agitation of the oxygen molecules is stronger than the van der Waals attraction, and oxygen can no longer be physisorbed on the platinum surface. Instead, oxygen molecules attach to the platinum surface by chemisorption. Current wisdom is that during the chemisorption process, electrons transfer from the the platinum d-band to the molecular $1\pi_g^*$ orbital of the oxygen molecules, and the oxygen molecules become negatively charged. Therefore,

the electronic configuration of the oxygen changes considerably, especially for molecular orbitals with low binding energies.

"Superoxo" oxygen resides on a bridge site between two platinum surface atoms, with the intermolecular axis between the two oxygen atoms parallel to the surface (perpendicular to the surface normal). The O-O bond length of the superoxo state is calculated to be 1.39 Å using density functional theory, which is in good agreement with experimental measurements [63, 64]. The adsorption energy of the superoxo molecular oxygen is estimated experimentally to be -0.4 eV/molecule [65]. The adsorption bond between the superoxo oxygen and the platinum surface is formed by **one** electron transferred from the platinum surface to the now half-filled oxygen $1\pi_g^*$ orbital.

The "peroxo" chemisorbed state resides on the fcc three-fold-hollow site of the platinum surface. The intermolecular axis also nearly parallels the surface, but with a slightly tilted angle. The O-O bond length for the peroxo state is calculated to be 1.43 Å, and in agreement with experimental estimates [63, 66]. The adsorption energy of the peroxo molecular oxygen is experimentally measured to be -0.5 eV/molecule [67]. The adsorption bond between the peroxo oxygen and the platinum surface is formed by **two** electrons transferred to the molecule, resulting in a fully filled oxygen $1\pi_g^*$ orbital. The adsorption energies and bond length information for the different oxygen states on the platinum surfaces are summarized in Table 3.1.

Several properties of these two forms of chemisorbed molecular oxygen states differ. The peroxo oxygen is slightly more tightly bound to the platinum surface than superoxo. In the peroxo species, one more electron is transferred from the platinum surface to the

	Adsorption Energy (eV/molecule)	Bond Length (Å)
Gas-phase oxygen molecules (O_2)	—	1.21
Superoxo molecular oxygen (O_2^-)	-0.40	1.39
Peroxo molecular oxygen (O_2^{2-})	-0.50	1.43
Atomic oxygen (O) (fcc)	-1.65	—
Atomic oxygen (O) (hcp)	-0.98	—

Table 3.1: Comparisons of the adsorption energies and bond lengths between gas-phase oxygen molecules (O_2), superoxo (O_2^-), peroxo molecular oxygen (O_2^{2-}), and atomic oxygen (O) on fcc and hcp sites.

$1\pi_g^*$ orbital, forming two hybridized bonds between the peroxo oxygen molecule and the platinum surface. Increasing charge occupation in the $1\pi_g^*$ orbital strengthens the connection between the oxygen molecule and the platinum surface; the $1\pi_g^*$ orbital of the oxygen molecule is, however, an anti-bonding orbital with respect to the oxygen intermolecular bond. Therefore, the intermolecular bond connecting the two oxygen atoms is weaker when the oxygen is adsorbed on the peroxo state as opposed to the superoxo state; this property can be confirmed by the fact that the bond length of the peroxo oxygen is slightly longer than that of the superoxo oxygen. In fact, both of the oxygen molecular chemisorbed states (superoxo and peroxo) have a longer bond length (1.39 Å and 1.42 Å) compared to the free oxygen molecules (1.21 Å). Because of this, the two chemisorbed molecular oxygen states are often called the "intermediate" or "precursor" states of chemical oxidation processes on metal surfaces. For many chemical oxidation processes, dissociation of oxygen molecules into two atomic oxygens is necessary to initiate the process. It is suggested that the oxygen dissociation progresses gradually through weakening of the oxygen intermolecular bond (by transferring the oxygen molecules to these intermediate states) and finally to complete dissociation [68, 69, 70].

Another difference between these two chemisorbed states is that the superoxo oxygen tends to cluster on the adsorption sites, whereas the peroxo oxygen tends to be isolated. This property has been confirmed by observing the states through the technique of scanning tunneling microscopy (STM) [71]. This could indicate that intermolecular interactions, either attractive or repulsive, between the adsorbates can be a crucial factor in stabilizing these two chemisorbed states on the platinum surface. The clustering effect of the superoxo oxygen can explain why, at the same surface temperature, superoxo oxygen tends to dominate with high oxygen coverage and peroxo oxygen tends to dominate with low oxygen coverage. In addition, observation from STM measurement shows that both the chemisorbed states are stable, and diffusion of chemisorbed molecules after adsorption is not observed. This stability also indicates that superoxo oxygen clustering is not due to diffusion of chemisorbed molecules, but to the existence of a mobile precursor state upon adsorption [71].

STM work has also demonstrated that it is possible to use the STM tip to manipulate an oxygen molecule, moving it between these two chemisorbed states (superoxo and peroxo) from the bridge to hollow site, or vice versa [72]. The STM tip can be positioned directly above the oxygen molecule either in the bridge or the hollow site. After applying a very small current (nA) to the STM tip, the oxygen molecule gains energy to overcome the barrier of the potential energy surface, and finally stably resides on another adsorption site without perturbing other neighboring oxygen molecules.

3.1.3 Atomic Oxygen

Atomic oxygen can be formed on Pt(111) by dosing oxygen molecules at above 150 K surface temperature. At this temperature the oxygen molecules dissociate before becoming adsorbed to the platinum surface. Atomic oxygen can also be formed by dosing oxygen molecules at lower surface temperatures and subsequently heating the platinum surface to above 150 K for a short period of time to dissociate adsorbed oxygen molecules [73, 74]. Oxygen atoms are energetically favorable to reside at either the fcc or the hcp threefold hollow sites (fcc sites have no platinum atom directly beneath in the second surface layer) [71]. Theoretical calculations have estimated that the adsorption energy is much larger in the fcc hollow sites ($E = -1.65$ eV/molecule) and considerably smaller in the hcp hollows ($E = -0.98$ eV/molecule) [70].

3.2 Experimental results of O_2/Pt (111)

3.2.1 Thermal Desorption Spectroscopy

Thermal desorption spectroscopy (TDS) [1] is a well-known and commonly used technique for characterizing chemical reaction processes on surfaces. The idea of TDS is to adsorb the molecules under study to the metal surface at a low non-reactive temperature. The temperature of the metal surface subsequently increases at a constant rate to a temperature well above the temperature where the adsorbates react and desorb. By measuring the yield of the desorbing molecular species and the corresponding desorbing temperatures, information about adsorption energy of the adsorbates, activation energy, and the reaction channels of the chemical reactions can be extracted. For oxygen on platinum (111), TDS

[1] Some literature refers to temperature programmed desorption spectroscopy

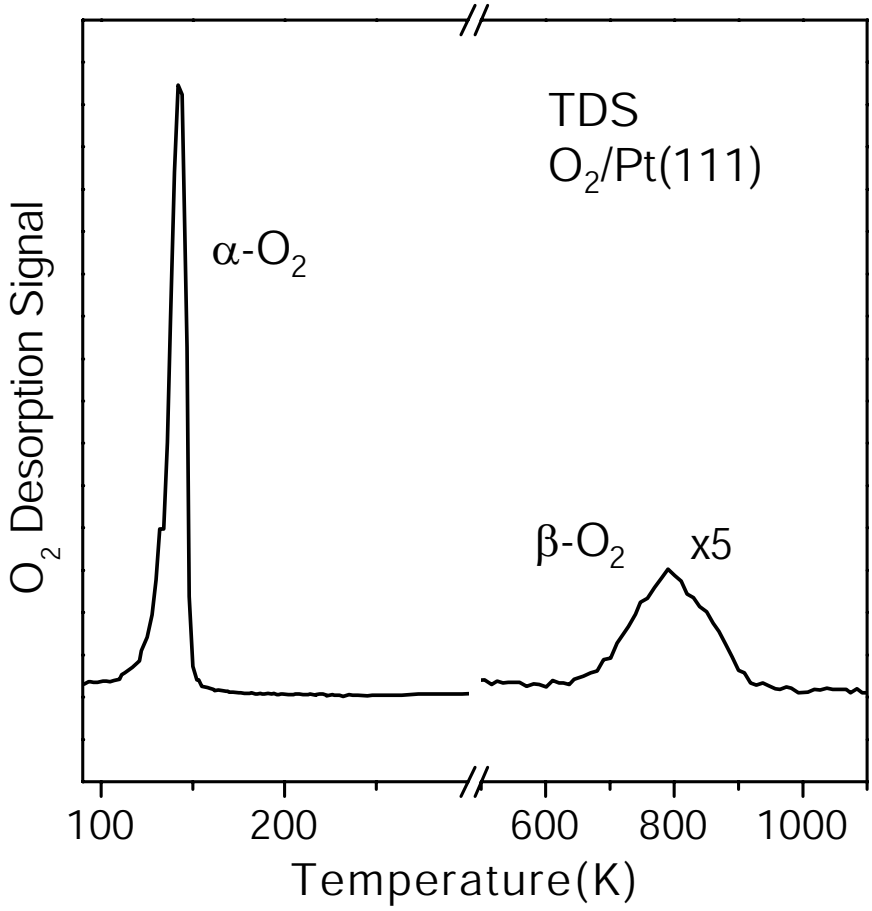

Figure 3.2: TDS for Pt(111) covered with O_2: the rate of temperature increase is 3 K/sec from 77 K to 300 K; then 10 K/sec from 300 K to 1100 K

can help us understand the oxygen chemisorbed states and their corresponding properties.

Figure 3.2 shows the TDS spectrum of O_2^- on Pt (111) taken using our setup. Oxygen was initially dosed onto the platinum sample at 77 K, to saturation coverage. Two distinct desorption peaks can be observed in the TDS spectrum: An intense $\alpha - O_2$ peak at 145 K, and a weaker high temperature $\beta - O_2$ peak (the symbols of α and β are used for identification purposes only; the oxygen molecules desorbing from these two peaks are the same). A reasonable explanation for the TDS spectrum of O_2/Pt is as follows: As discussed in

the previous section, superoxo oxygen (O_2^-) dominates at the bridge site at high coverage when oxygen is dosed to full coverage at liquid nitrogen temperature. When the surface temperature is heated above 145 K, a large fraction of oxygen molecules desorbs from the platinum surface, since the oxygen molecules have gained enough energy to overcome the energy barrier for desorption. Once some of the oxygen molecules desorb, the oxygen coverage becomes much lower on the platinum surface, and there will not be enough oxygen molecules left on the surface to cluster at adjacent bridge sites. The oxygen molecules now tend to move from the bridge site to the three-fold-hollow sites to lower their total energy, leading to a state transition from the superoxo (O_2^-) into the peroxo (O_2^{2-}) state for the remaining oxygen molecules. When the surface temperature increases above 200 K, the intermolecular bond of the adsorbed oxygen molecule will gain enough energy to be broken. This causes the oxygen molecule to dissociate into two identical oxygen atoms (O), and the two oxygen atoms absorb on two different three-fold-hollow sites on a platinum surface. Since the atomic oxygens have a much higher adsorption energy, they will remain on the platinum surface until the surface temperature reaches temperatures higher than 800 K. Finally, the atomic oxygen will desorb recombinatively to form oxygen molecules and leave the platinum surface.

3.2.2 Static photoemission spectra of the different oxygen states

From the knowledge gained from TDS investigation, we can now selectively prepare the oxygen adsorbed on the platinum surface preferentially for a certain oxygen state. Experimentally, saturation coverage leads to superoxo oxygen as dominant state. Therfore, to prepare superoxo oxygen, oxygen can simply be dosed onto a platinum surface to the sat-

uration coverage at liquid nitrogen temperature, so that most of the oxygen molecules will cluster and reside on the bridge sides of the platinum surface. By heating the platinum surface to 145 K, a partial desorption of molecular oxygen increases the occupation of three-fold-hollow sites for the oxygen molecules, and leads to a predominance of the peroxo chemisorbed state. At temperatures above 145 K, oxygen molecules will gain enough energy to dissociate into oxygen atoms; therefore, heating the sample to room temperature is the preferable way of obtaining atomic oxygen [14, 63, 65, 69, 72, 75].

Static photoemission spectra have been taken using our TR-UPS setup by blocking the pump pulses to avoid excitation for the clean Pt(111) surface, O_2^- /Pt(111), O_2^{2-}/Pt(111), and O/Pt(111). Comparing the spectrum of the clean Pt(111) surface to the other oxygen covered spectra reveals that the intensity of the platinum d-band, where the binding energy is close to the Fermi-edge, is strongly reduced for the latter spectra. This surface sensitivity is expected – when oxygen molecules adsorb on the platinum surface, the electrons emitting from the platinum are scattered back into the platinum due to the presence of the oxygen molecules.

At a binding energy of about 6 eV (referenced to the Fermi level), an oxygen-related feature appears in the oxygen covered spectra. This feature has been observed previously by others using synchrotron radiation sources, where it has been assigned to the occupied oxygen $1\pi_g^*$ orbitals of the free oxygen molecule [66]. The position of this feature appearing at about 6 eV binding energy agrees with calculations of density functional theory [70, 76] that the oxygen molecule absorbed at the three-fold-hollow site has a higher density-of-states at this energy. At the EUV photon energy of 42 eV used in our setup, this

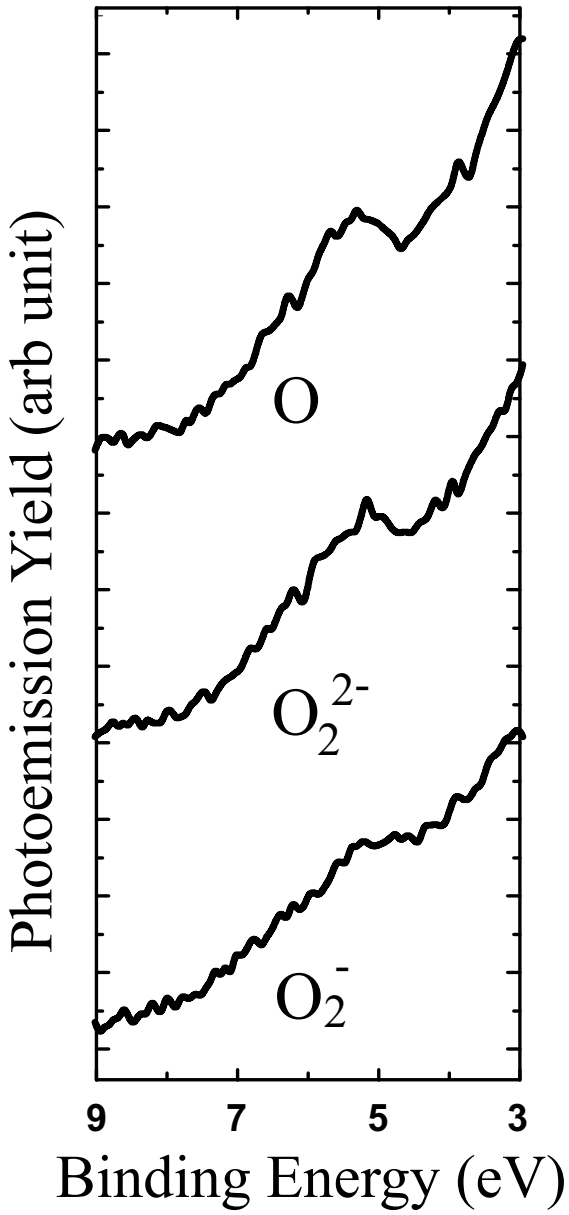

Figure 3.3: Static photoemission spectra taken for the superoxo (O_2^-), peroxo (O_2^{2-}) and atomic (O) oxygen states on Pt(111).

feature is particularly sensitive to the chemical bond character of the oxygen chemisorbed configuration. Close-up photoemission spectra are shown in Fig. 3.3 for the superoxo (O_2^-), peroxo (O_2^{2-}) and atomic (O) oxygen states on Pt (111) around the binding energy from 3 to 9 eV. In qualitative agreement with results by Puglia and co-workers [63], we observe a change in the spectral shape of the $1\pi_g^*$ orbital between the superoxo and peroxo states, but no significant difference in this energy region between the peroxo oxygen and the atomic oxygen states. This change is due to the different degree of hybridizaton of the particular oxygen state to the platinum d-band. Comparatively, the spectrum of the superoxo oxygen remains relatively flat in this energy region, similar to the clean platinum surface, while the spectrum of peroxo and atomic oxygen has a "peak" at about 6 eV binding energy. The spectra of peroxo oxygen and atomic oxygen have similar features in this region because the peroxo oxygen resides in a geometry similar to the atomic oxygen, and also the peroxo oxygen is considered to be the "precursor" state in the process of molecular dissociation. In the following experiment to probe the oxygen dynamics, this peak will be used as a valuable "signature" to indicate whether the oxygen is changing its chemisorbed configuration, by observing the change of this peak after the O_2/Pt system is triggered by an intense ultrafast pulse.

3.2.3 Oxygen desorption induced by intense ultrafast pulses

Desorption by intense femtosecond laser pulses of O_2/Pt(111) has been studied previously by photo-desorption yield measurements [14, 77]. In particular, a nonlinear dependence of desorption yield with increasing laser intensity has been reported. In fact, this nonlinear dependence has been reported for many adsorbate/metal systems and proposed

as the result of direct coupling between excited hot surface electrons and adsorbates, without conventional heating from the surface lattice, or phonons [78]. In Mazur's desorption work [77], he proposed that after the sample was excited by an ultrafast pulse, a new "configuration" for the adsorbed oxygen molecules is created. The oxygen molecules could settle in a configuration that differs from a "fresh" platinum surface. This new configuration might complicate further subsequent laser desorption and deposition cycles result in a decreasing desorption yield. Figure 3.4 shows femtosecond-induced desorption yield traces for two adjacent desorption cycles with oxygen redosing in between. This observation indicates that a surface modification other than complete oxygen depletion occurs, resulting in a diminished number of free adsorption sites in subsequent desorption cycles. One reasonable explanation is that the high intensity laser pulse not only desorbs the oxygen from the platinum surface, but the oxygen molecules are also dissociated into oxygen atoms. These oxygen atoms then block the adsorption site. In general, nonreversible effects, such as dissociation, are not desirable for time-resolved photoemission experiments and should be minimized. Each photoemission spectrum at each time delay needs to be accumulated through many pump-probe excitations. Hence, a large advantage is realized if the system under study reverts to its original state before another excitation cycle starts. Otherwise, reversible and irreversible changes are superimposed making data interpretation difficult. Therefore, in all of our experiments, we used a low (10-15 $\mu\mathrm{J/mm}^2$) pump fluence to minimize nonreversible processes, such as desorption and dissociation. From extrapolation of control experimental data, we estimate that significant irrversible oxygen desorption requires a time scale of more than an hour for the pump excitation levels used

in our time-resolved work.

3.2.4 Probing O_2/Pt(111) by TR-UPS

We start by adsorbing a saturation layer of molecular oxygen onto the platinum surface at liquid nitrogen temperature (77 K). Photoemission spectra were taken at different time delays between the pump infrared pulse and the EUV probe pulse. Significant changes were observed in the spectra as a function of time delay between the pump and the probe in two different energy regions: at the Fermi edge, and at a binding energy of 6 eV reference to the Fermi level, where the oxygen-induced feature ($1\pi_g^*$) appears.

Figure 3.5 shows the transient modifications at the Fermi edge as observed at different delays. At time zero (i.e., when the pump and probe pulses arrive temporally coincident at the surface), the shape of the Fermi edge is modified by a "step" at energies above the Fermi edge with a width of about 1.5 eV, corresponding to the energy of the exciting photons. Some evidence of this feature is still visible at 150 fs delay. Within another 100 fs, or 250 fs after the pulse pulse arrives, this nonthermal contribution has completely disappeared. At longer time delays, no further changes in this energy region were observed. The experimental distribution at time-zero is best reproduced by an excitation level of about 6% (at a photon energy of 1.5 eV). Referring to the insert of Fig. 3.5, the solid line is the calculated distribution for this excitation level, convolved with the estimated detector resolution of 370 meV. For reference, a spectrum taken with solely with the probe EUV beam (ground-state distribution) is fitted to a Fermi-Dirac distribution at 100 K, which is also convolved with the detector resolution.

Figure 3.6(b-e) shows the pump-probe spectra at various time delays, focusing on

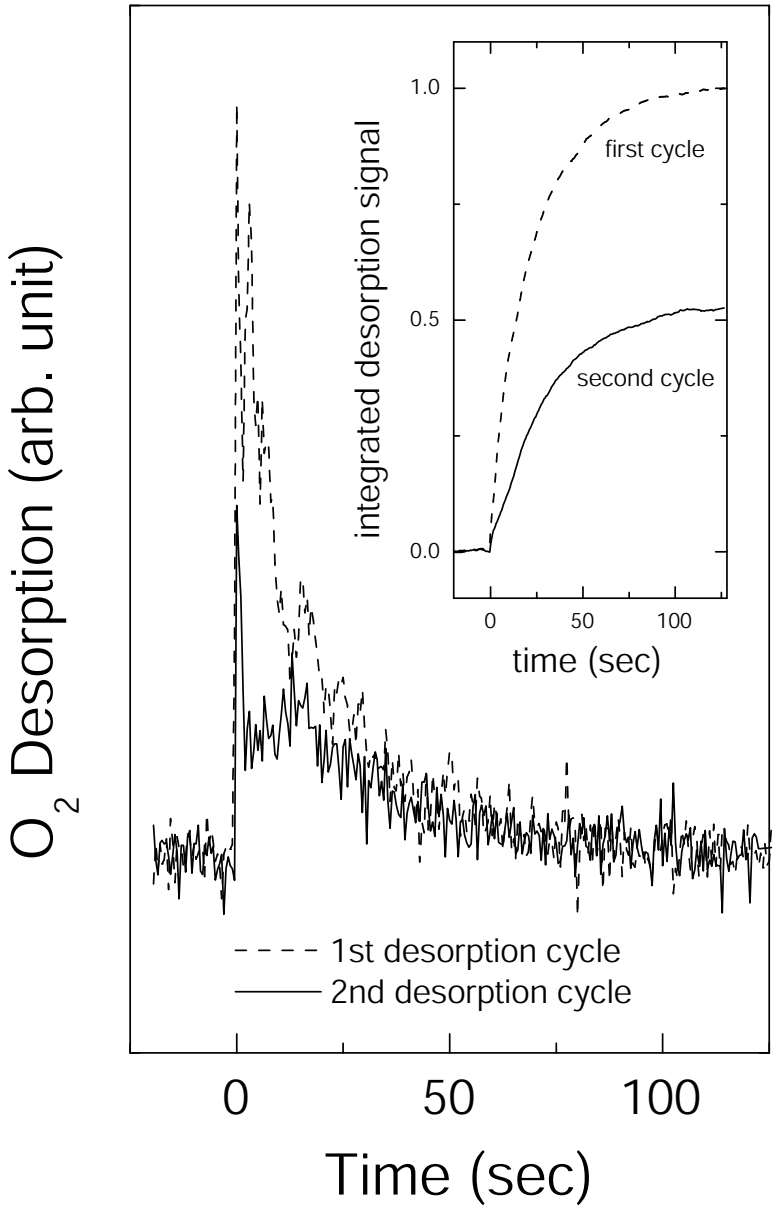

Figure 3.4: Femtosecond laser-induced desorption for the two adjacent desorption cycles with oxygen redosing between the two laser excitations. Insert shows the integrated desorption signal for the two cycles.

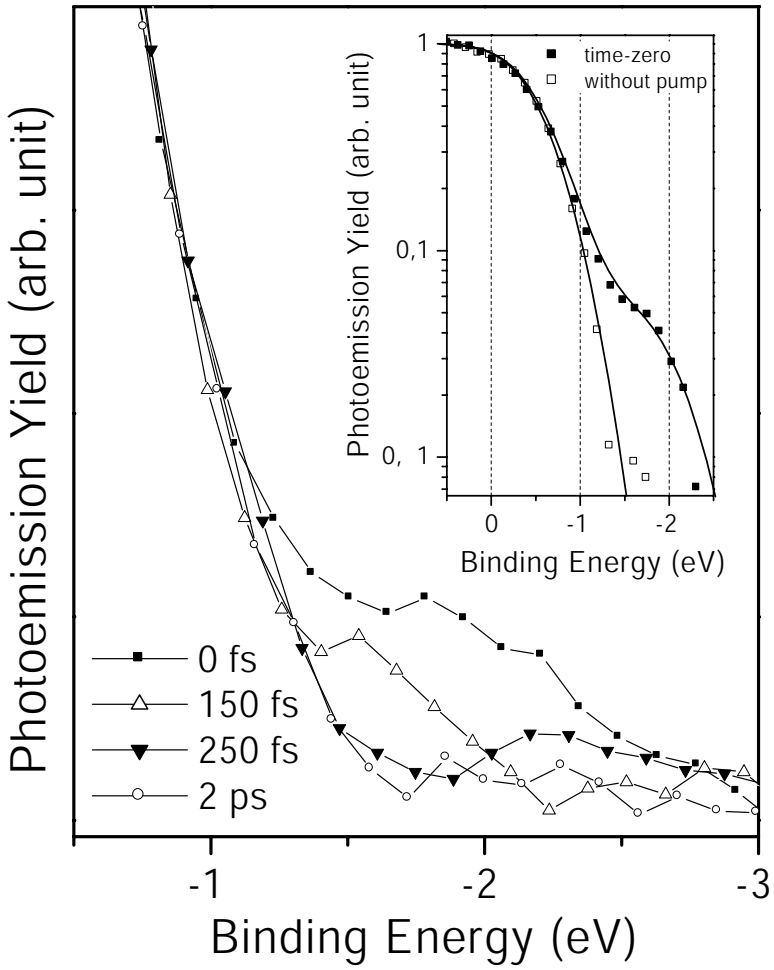

Figure 3.5: Electron energy distribution at Fermi edge of O_2/Pt(111), for time delays of 0 fs, 150 fs, 250 fs, and 2 ps. Nonequilibrium hot electrons can be seen at 0 and 150 fs; however, at 250 fs, the energy distribution has thermalized. Inset: Fermi edges at 0 fs time delay (black square) and static spectrum without pump pulses excitation (hollow square), plotted in log scale. The electron distribution at 0 fs time delay can be fit to a 100 K Fermi-Dirac distribution with 6% of the electrons excited by the pump photon energy (1.5 eV).

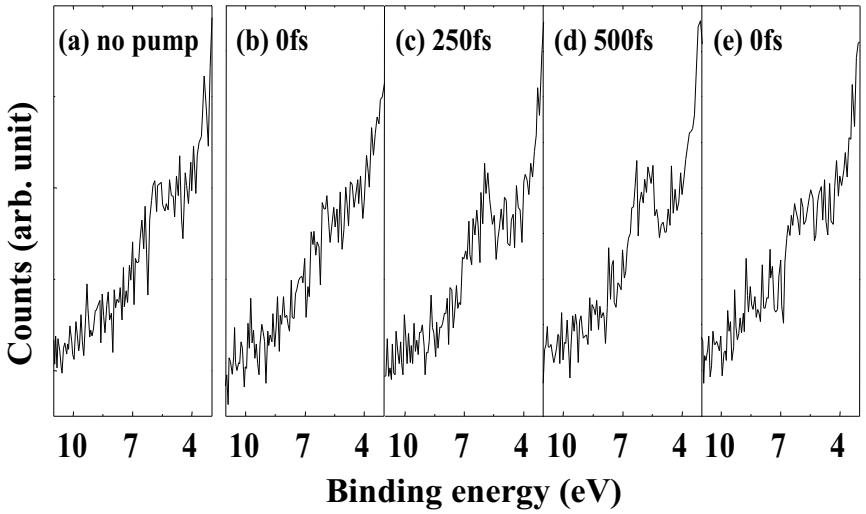

Figure 3.6: Time-resolved high-resolution photoemission spectra from a saturation layer of molecular oxygen adsorbed on a Pt(111) surface at liquid nitrogen temperature: (a) no pump beam; (b) with pump beam, zero time delay between pump and probe; (c) 250 fs time delay between pump and probe; (d) 500 fs time delay; (e) repeat of (b), taken immediately after (d).

the higher binding energy part of the valence band spectra. For comparison purpose, a photo-electron spectrum without pump beam excitation was taken in the very beginning, as shown in Fig. 3.6(a). In these spectra, the feature appears at around 6 eV binding energy corresponding to the oxygen $1\pi_g^*$ orbital hybrized with the platinum surface, as discussed in previous paragraphs. Figure 3.6(b) shows the spectrum obtained at zero time delay; no significant changes are visible when compared to the static spectrum. This contrasts with the changes above the Fermi-edge at zero time delay, as shown in Fig. 3.5, where the non-thermal distribution happens at zero time delay. However, at 250 fs time delay – well after the 55 fs pump pulse has been adsorbed and the nonthermal distribution at the Fermi edge has disappeared – a significant peak-like structure emerges out of the background. This peak-like structure is even stronger at a pump-probe delay of 500 fs, and it persists for

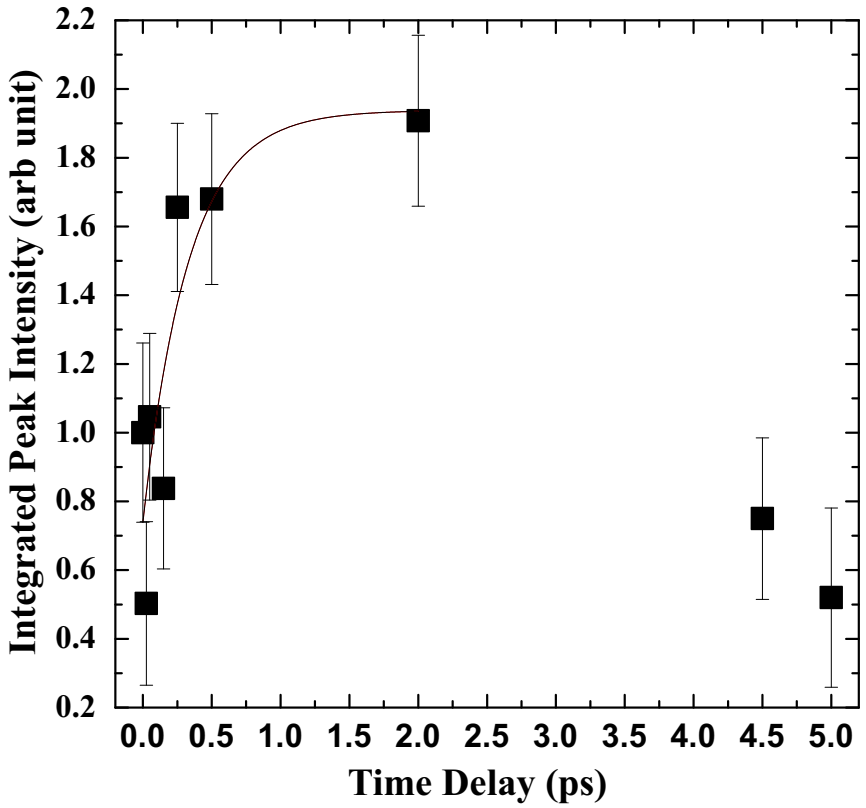

Figure 3.7: Integrated amplitude of the characteristic 6 eV peak feature as a function of pump-probe delay. A fit to the data indicates an onset time of 550 ± 140 fs.

several ps. Although our spectra were taken sequentially in this experiment with increasing time delays, this observed feature is not a permanent change of the sample through continuous pump pulse excitation, but rather a transient change. This can be verified by taking another spectrum at zero time delay immediately after the 500 fs spectrum is taken. This final time-zero spectrum is identical to the spectra of (a) and (b), which are taken at the beginning of the pump-probe scans. Therefore, in this experiment, the observed changes are definitely reversible, and a transient modification of the adsorbate bonding is monitored with femtosecond timing resolution for the first time.

By repeating this experiment to acquire more detailed scans, we are able to extract

the characteristic population and relaxation rates of this transient (meta-stable) excited adsorbate state. Figure 3.7 is a plot of the integrated strength of this transient peak as a function of time delay. The data points can be fitted by an exponential growth function:

$$y = y_0 + Ae^{(\frac{x-x_0}{t_0})} \tag{3.1}$$

where t_0 is the rise time of the exponential increase function. By using this fitting equation to the extracted data, we estimate that the observed peak has an exponential rise time $t_0 = 550 \pm 140$ fs. Together with the information at longer time delays, we know that the signal decays within about 5 ps after the pump pulse arrives.

3.2.5 Permanent modification of O_2 on Pt(111)

In addition to the reversible change observed in the valence band structure, over the time scale of several hours of continuous pump pulse excitation, we also observe a long-term nonreversible change of the surface state induced by the ultrafast infrared pump pulses. Figure 3.8 shows a series of spectra taken during a period of 2 hours of irradiation by the ultrafast infrared pump pulses. During the first hour of the pump pulse irradiation, after a saturation coverage of oxygen was adsorbed to the platinum surface, no significant changes in the spectrum are observed. However, further irradiation from the ultrafast infrared pulse pulses alters the 6 eV binding energy feature from a shoulder-like structure to a peak-like structure. This peak-like structure is similar to the spectra of the peroxo and atomic oxygen states on the platinum surface of their static spectrum; it is also similar to the transient peak appearing in the pump-probe scans. This differs from the transient feature, which disappears when the time delay returns to zero. By continuing ultrafast

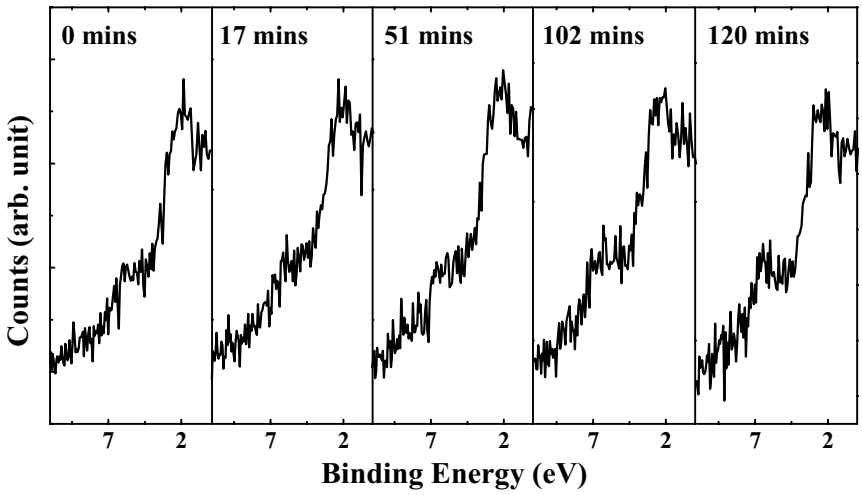

Figure 3.8: Spectra taken during pump beam irradiation of the sample over a period of 2 hours. During the first ≈ 50 min, the spectra are unchanged. However, after ≈ 100 min, the characteristic 6 eV peak gradually increases and is permanently present on the subsequent spectrum taken.

infrared pump pulses irradiation over several hours, this feature remains after the pump pulses have stopped, indicating the sample condition does not return to its original state. This feature in the photoemission spectrum seems to represent a stable configuration of the O_2/Pt(111) system, resulting from continued irradiation by the ultrafast infrared pump pulses over several hours.

3.3 Discussion

The reaction pathways of surface chemical reactions induced by an intense, ultrafast infrared pulse could possibly proceed in following order:

1. Creation of a nonthermalized or “hot” electron distribution at the metal surface results from the energy adsorption of the excited ultrafast pulse.

2. Internal energy redistribution between the hot electrons to achieve a thermalized

configuration.

3. Adsorbate excitation caused by the energy transfer mediated by hot electrons from the metal surface.

4. Modification of the adsorbates-surface chemical bond character leads to translational and rotational motions of the adsorbates.

5. Thermalization between the electrons and the surface photons.

6. Traditional "phonon induced" chemical surface reaction caused by the elevated phonon temperature, but this step happens in a much longer time scale ($\sim$ps).

In the pump-probe experiment, the transient feature of the photoemission spectrum observed above the Fermi edge could be assigned to the step 1; while the transient peak observed at the higher binding energy side of the valence band could be assigned to the step 3. Furthermore, knowledge of the adsorbed fluence as well as the measured excitation rate of the electron gas allow us to reconstruct steps 2, 4 and 5.

3.3.1 Nonthermal surface electrons on Pt(111) surface

3.3.1.1 Nonthermal surface electrons observed in the experiment

Laser energy adsorbed by the adsorbate layer (in this case, a saturated layer of molecular oxygen) is extremely low; therefore, direct excitation from the ultrafast infrared pump pulse is highly unlikely [78, 79]. The energy of the incident infrared pulse is adsorbed entirely by the electrons on the top ~ 100 Å thick of the platinum (111) surface. Because of the extremely short ($\sim$ 65 fs) and intense ($> 10^{12}$ W/mm^2) excitation, this energy

results in a extremely nonthermal energy distribution of the electron gas. This nonthermal distribution can be observed at the spectrum taken at zero time delay, that shows a transient "step" above the Fermi-edge. The adsorbed fluence of 1 mJ/cm^2 results in an estimated excitation of about 6% of the electrons at the platinum surface [80]. Comparable excitation levels have been reported for heating a 300 Å thick gold film [32] and a Pt(110) surface [81] by ultrafast pulses. The fact that the transient nonthermal feature of the "hot" electron step at the Fermi-edge disappears within the first 250 fs after the zero time delay is in agreement with the measurement of the Pt(110) surface [81]. In contrast, significantly longer lifetimes of the nonthermal contribution (up to 400 fs) have been reported for gold. This time difference between the platinum and the gold surfaces can be explained as a much slower electron thermalization process in noble metals in comparison to transition metals, because of a reduced electron-electron scattering rate at the relevant energies [82, 83]. The measurement is extremely surface sensitive because the 42 eV EUV probe photons we used can only liberate electrons from the top 5 Å of the platinum surface due to the short electron penetration depth at these kinetic energies.

3.3.1.2 Two temperature model and nonthermal surface electrons lifetime

Knowledge of the absorbed fluence allows us to calculate the time evolution of the electron and lattice temperatures. Due to its low heat capacity, the surface electrons are heated quite efficiently by ultrafast infrared pulses. Although the electron distribution immediately after the excitation is nonthermalized and technically cannot be fully described quantitatively by a simple temperature, nevertheless the calculated electron temperature is a useful indicator of the actual excitation degree of the surface electrons.

Thermalization of the electron distribution occurs within 250 fs, followed by subsequent cooling of the hot electrons due to coupling to the surface lattice phonons (electron-phonon coupling). The electron-phonon effective collision time is actually of the same order as the electron-electron scattering time. It is, however, quite inefficient with respect to collisional energy exchange, because of the typical phonon energies required for the energy transition (about some tens of meV), where significant excitation of the surface lattice occurs on a much longer time scale than the electron dynamics. In addition, the higher heat capacity of the lattice limits the maximum lattice temperature to a much lower temperature than that of the electrons. On the other hand, since only the electrons at the top ~ 100 Å of the platinum surface are excited by the ultrafast pulses, thermal diffusion between the electrons at the metal surface and the electrons at the bulk also has a significant effect on the thermalization process.

The interplay between ultrafast pulses, hot electrons, and the lattice (phonons) can generally be calculated by a simplified model, or so-called "two-temperature model" [84]. A set of coupled equations is used to determine the electron temperature (T_e) and the lattice temperature (T_p) as a function of time:

$$C_e \frac{\partial}{\partial t} T_e = \frac{\partial}{\partial z}(\kappa \frac{\partial}{\partial z} T_e) - g(T_e - T_p) + \widehat{F} \tag{3.2}$$

$$C_p \frac{\partial}{\partial t} T_p = g(T_e - T_p) \tag{3.3}$$

where $C_e = \gamma T_e$ and C_p are the electron and lattice heat capacities, respectively. $\kappa = \kappa(T_e/T_p)$ is the thermal conductivity and g is the electron-phonon coupling constant. The

Electron specific heat γ	$748\ \mathrm{J/m^3K^2}$
Thermal conductivity κ_0(77 K)	$71.6\ \mathrm{W/mK}$
Electron-phonon coupling constant g	$6.76 \times 10^{17}\ \mathrm{W/m^3K}$
Lattice heat capacity C_p (77 K)	$2.69 \times 10^6\ \mathrm{J/m^3K}$
Absorbed laser peak intensity I_0	$1.71 \times 10^{14}\ \mathrm{W/m^2}$
Pulse width τ	$55\ \mathrm{fs}$
Optical penetration depth λ (800nm)	$12.56\ \mathrm{nm}$

Table 3.2: Parameters of platinum(111) used in the calculation of electron and lattice temperatures

term $\hat{F}$ is used to describe the femtosecond pump pulse in the form of

$$\hat{F} = \frac{I_0}{\lambda} e^{-4log(2)t/\tau - z/\lambda} \tag{3.4}$$

where I_0 is the adsorbed laser peak intensity, λ is the optical penetration depth, and τ is the pump pulse width. All the parameters used in this simulation are listed in Table 3.2.

The calculated result is shown in Fig. 3.9, and the measured nonthermal electron integrated intensity is shown in parallel for comparison purposes. For a platinum surface excited by a 10 $\mu\mathrm{J/mm^2}$ and 55 fs ultrafast pulse, we predict the maximum electron temperature to be 1082 K at 35 fs after zero time delay, i.e., immediately after the laser pulse (55 fs) has totally arrived. The same value for the maximum temperature (about 1000 K) can be calculated from the measured excitation of the electron gas of 6% [80]. In contrast, the calculated maximum temperature of the lattice is 174 K, and is reached at 1.2 ps after the ultrafast pulse excitation. At this long time scale, the electron and lattice temperatures are equilibrated and the condition of the sample heating is similar to conventional thermal surface chemical reaction, at which the electron and lattice temperatures are equal.

Figure 3.9 shows that at long delays (> 1 ps), the calculated lattice temperature is a little higher than the electron temperature. This is a numerical simulation artifact that is

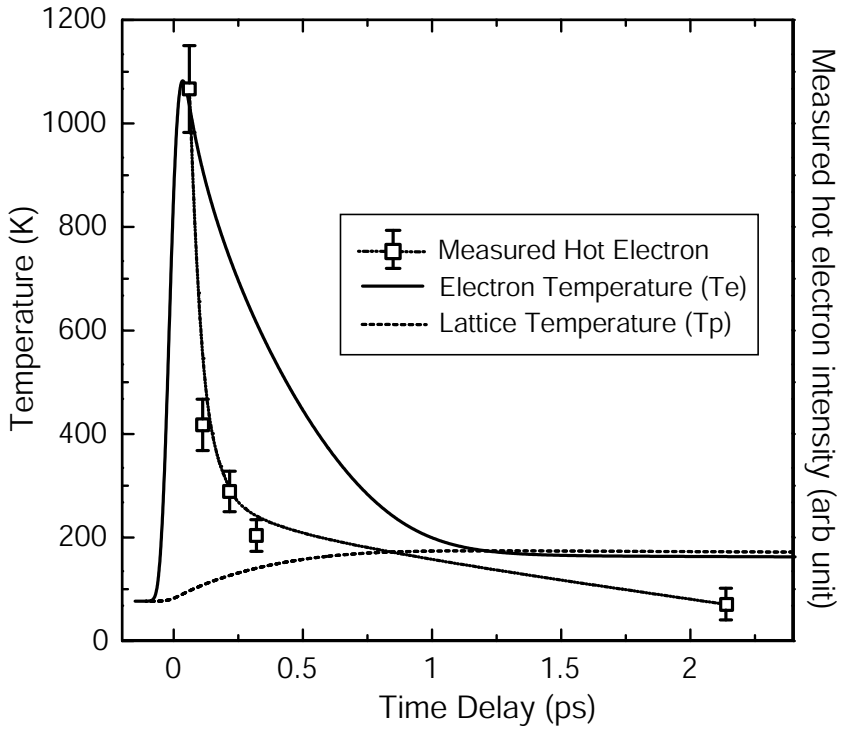

Figure 3.9: Calculated electron temperature (T_e) and lattice temperature (T_p) using the "two-temperature model" at the platinum (111) surface excited by a 10 $\mu\mathrm{J}/\mathrm{mm}^2$, 55 fs ultrafast infrared pulse. The measured nonthermal electron integrated intensity (square) is also shown in the figure for comparison purposes.

caused by the simple two-temperature model. This artifact happens because only electron heat diffusion is considered in Eq. 3.2, and the lattice thermal diffusion is completely neglected due to the fact that the electron thermal diffusion is significantly more efficient than the lattice thermal diffusion. The optical excitation of the surface electrons only happens within the optical penetration depth of the platinum surface, and at around several picoseconds after the optical excitation the temperature of the surface electrons is still much higher than the bulk. Therefore, the surface electrons keep loosing energy to the bulk electrons to achieve thermal equilibrium for the whole crystal. However, most of the energy initially adsorbed by the surface electrons has been transferred to the surface lattice by this time. The surface lattice has to give back its stored energy to the surface electrons, which continue to loose energy to the bulk electrons. Therefore, the surface lattice temperature is slightly higher than the surface electron temperature to maintain an energy gradient to give up energy from the surface lattice to the surface electrons for thermal diffusion. True equilibrium will happen at a very long time delay, when the whole sample achieves thermal equilibrium and no gradients remain.

The two-temperature model is often criticized for being too “simple” to describe the actual ultrafast electron heating process. Since the rapid heating of electrons by an intense ultrafast pulse will cause the surface electrons to become highly excited, the excited electrons cannot be described by a “temperature” that can only be defined when the electrons are in thermal equilibrium, especially in the first several hundred femtoseconds after the excitation. In fact, more complicated models are needed to accurately describe the nonthermal electrons excited by ultrafast laser pulses. However, by integrating the nonthermal

electrons measured in Fig. 3.5, Fig. 3.9 compares the measured nonthermal electron integrated intensity with the calculated electron temperature. This comparison does show that the de-excitation rate of the calculated electron temperature is quantitatively similar to the measured nonthermal electron intensity. Therefore, the two-temperature model provides insight into understanding the role of surface hot electrons in femtochemistry on metal surfaces.

Hot-electron temperature at longer time scales can, in principle, be obtained by measuring the slope of the Fermi-edge from the pump-probe spectrum. However, due to the resolution limitation of our detector and the limited statistics of our measurements, the gradual tilting of the slope of the Fermi-edge cannot be distinguished from our spectrum, and we are not able to further compare the two-temperature model with the actual measurement at a longer time scale.

3.3.1.3 Excitation of O_2 by nonthermal surface electrons

As discussed in Sec. 3.2.4, a transient feature appears at about 6 eV binding energy on the time scale of about half a picosecond on our measured spectra. This raises a question of how this transient change is created. There are three possible mechanisms to explain the transient effect observed, including: (1) pure electronic artifact, (2) phonon-mediated oxygen state transition, and (3) nonthermal electron-mediated oxygen state transition.

Figure 3.10 compares the integrated intensity of the measured transient feature to the calculated electron and lattice temperatures by the two-temperature model. Figure 3.10(a) clearly shows that the maximum intensity of the transient feature is delayed about 1 ps with respect to the time when the maximum electron temperature is reached. Also, the oxygen

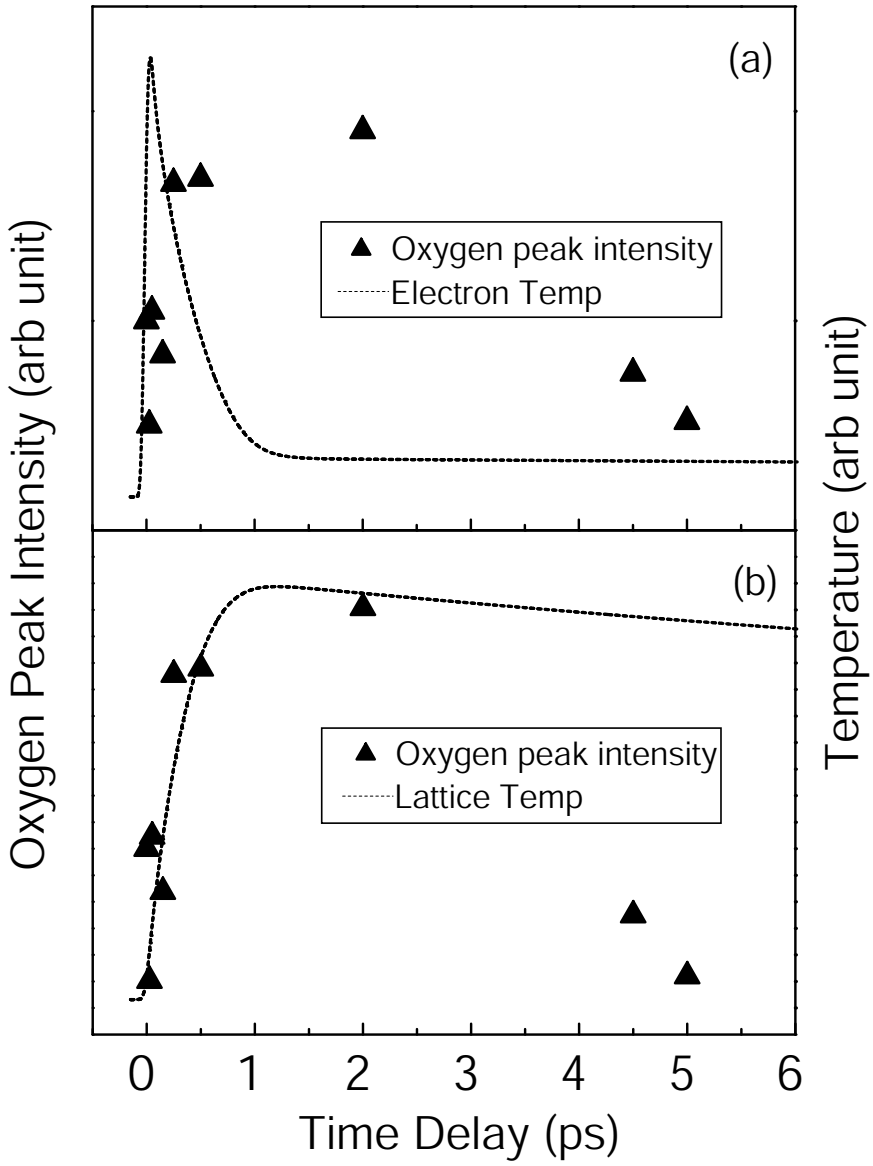

Figure 3.10: Integrated intensity of the peroxo signature peak compared to the rescaled (a) electron and (b) lattice temperature.

peak relaxes at about 5 ps, by which time the surface electrons have long been cooled for several picoseconds. Therefore, if the transient feature is a pure electronic excitation of case (1), the peak-like transient feature should have a rise and relaxation time similar to that of the nonthermal surface electrons. Hence, the possibility that the observed transient feature is a purely electronic artifact is not likely.

For case (2), it might seem possible that the transient feature could be a phonon mediated process, since the lattice temperature has a rise time similar to that of the transient feature. However, the lattice temperature actually takes a very long time to cool down when compared to the relatively short relaxation time ($\sim$ 5 ps) of the oxygen peak, as shown in Fig. 3.10(b). Therefore, if the observed transient feature was actually driven primarily by phonon excitation, as in conventional surface chemistry, the relaxation time of the oxygen peak would be much longer than the 5 ps that we observed. It ought to be comparable to the lattice relaxation time. Furthermore, comparable rise time between the lattice temperature and the transient feature actually indicates that the excitation process cannot be phonon-mediated. The reason is because a finite time delay is actually required between the rise times of the lattice temperature and the transient feature, since a finite coupling time is needed to transfer energy from the lattice to excite the adsorbates, as required by the frictional model [85]. Therefore, the nonthermal electrons at the platinum surface are most likely to be directly driving the changes in the oxygen configuration.

By excluding the first two possible mechanisms, the transient feature is most likely mediated by the nonthermal surface electrons of case (3).

3.3.2 Mechanism of O_2 excitation

3.3.2.1 Identification of the transient feature

From the discussion of Sec. 3.2.2, the difference in the photoemission spectrum at 6 eV binding energy between superoxo and peroxo chemisorbed states is assigned to the difference in the electron occupancy of the $1\pi_g^*$ orbital of the oxygen molecules. For superoxo, the $1\pi_g^*$orbital is half-filled; whereas for peroxo, the $1\pi_g^*$ orbital is fully occupied. This difference changes the density of state of the oxygen molecules and causes the photoemission spectra of peroxo chemisorbed state to have a peak-like feature at the 6 eV binding energy below the Fermi-edge [63, 70]. Together with the discussion from the previous section, the appearance of this transient feature possibly reflects a state transition for the chemisorbed oxygen molecules mediated from the coupling of the nonthermal surface electrons on the platinum surface.

As mentioned in Sec. 3.1.2, the $1\pi_g^*$ orbital of the oxygen molecule is important to the interaction between the adsorbed oxygen molecules and the platinum surface. Since the $1\pi_g^*$ orbital is "anti-bonding" in nature, the bond length between the two oxygen atoms is slightly longer for the peroxo oxygen (fully filled) than the superoxo oxygen (half-filled). However, the $1\pi_g^*$ orbital also is hybridized with platinum d-band; thereby it is "bonding" in nature with respect to the oxygen molecule and the platinum surface. This causes the peroxo oxygen to bond more tightly to the platinum surface. Therefore, as is widely accepted in conventional investigations, the spectral changes we observed in the pump-probe measurements could not merely reflect electronic transients. It is very likely to reflect modifications to the chemisorbed state of the oxygen initiated by changes at the surface-adsorbate bonding.

The similarity between the static spectrum of the peroxo oxygen, the static spectrum of the atomic oxygen (Fig. 3.3), and the transient pump-probe spectrum at about 500 fs time delays (Fig. 3.6) reveals two possibilities for the nature of this transient state transition of the adsorbed oxygen molecules. The initial superoxo oxygen (O_2^-) on the platinum surface can be excited by the ultrafast pulses into either: (1) two transient dissociated atomic oxygen atoms, or (2) an excited peroxo oxygen (O_2^{2-}).

In fact, these two possible processes are closely related, or even identical to a certain extent. Previous calculations using density functional theory [69, 86] have suggested that the peroxo oxygen can actually be considered to be a "precursor" state in the process of dissociation to two oxygen atoms. According to calculations, superoxo oxygen has a comparatively higher energy barrier to dissociate; however, after the superoxo oxygen transfers to the site of peroxo oxygen and subsequently changes its bonding character through charge transfer with the platinum d-band, the energy barrier for dissociation is reduced. The reduction of the energy barrier for dissociation can be explained by the weakening of the intermolecular bond between the two oxygen atoms when an additional electron is tunneled to the $1\pi_g^*$ orbital from the platinum d-band. Moreover, this charge transfer will cause the oxygen molecule to move from its original bridge site to the three-fold-hollow site, due to the creation of an extra bond to the platinum surface.

Complete dissociation into two oxygen atoms is not possible because the transient features are observed in the pump-probe scans are in fact reversible. If the transient feature is identified as two fully dissociated oxygen atoms, these two oxygen atoms will need to recombine back into an oxygen molecule in a short period of time (~ 5 ps). In addition,

atomic oxygen has the highest binding energy to the platinum surface of all the adsorption states. Thus it is very unlikely that the stable oxygen atoms would recombine back into a less-stable molecular configuration. Moreover, the probability for two separate atomic oxygens to get close enough for recombination would be rather low if the two dissociated oxygen atoms adsorb at two non-adjacent three-fold-hollow sites (2x2 structure).

Finally, a reversible replenished desorption process is also unlikely. The reason is that significant oxygen re-adsorption to the depleted oxygen sites in the time interval between the ultrafast pulses (1 ms) requires an oxygen ambient pressure of higher than 10^{-3} torr[2], but the chamber pressure is kept in the 10^{-10} torr range during the whole experiment. Lateral oxygen diffusion to replenish the depleted oxygen sites is also not possible because the following test was performed to ensure that lateral diffusion rate is low in the experimental surface temperature (77 K): An oxygen covered surface was first depleted by intense ultrafast pulses. Then, the sample sat still for several minutes to allow possible lateral diffusion to happen. Intense ultrafast pulses were reintroduced onto the depleted spot, but no further oxygen desorption could be detected on the second laser desorption. In addition, pictures taken by STM on an oxygen covered platinum surface cannot identify any possible oxygen redistribution after the oxygen dosing, indicating oxygen lateral diffusion is insignificant [71].

In conclusion, the transient feature that appears in the pump-probe scans can be identified as the superoxo molecular oxygen state (O_2^-) is transferring into a highly-excited peroxo molecular oxygen state (O_2^{2-}) or equivalently, a transient dissociated oxygen atomic

[2]1 Lamuire (L) $\equiv 10^{-6}$ torr·sec. In general, dosing 1 L of molecules will deposit a surface to the saturation coverage. For 1 ms, pressure of 10^{-3} torr will be required.

state (O), in a half-picosecond time scale.

3.3.2.2 Excitation rate of molecular oxygen

By comparing the peak height observed in the pump-probe spectra with that observed in the static spectrum of the atomic oxygen, the actual excitation rate of molecular oxygen by the pump ultrafast pulse can be estimated. As discussed in Sec. 3.2.2, heating an superoxo oxygen covered platinum sample to different surface temperatures can transform the oxygen into the peroxo and the atomic oxygen states. For both the TDS and UPS static spectrum, conventional lattice heating is used to transform the superoxo oxygen to the peroxo and atomic oxygen, and hence the transformed peroxo and atomic oxygen coverage on these two cases should, in principle, be the same.

The total amount of adsorbed oxygen on the platinum surface is proportional to the combined area of the the α and β peaks from the TDS spectrum. By comparing the ratio of the total areas of the α and β peaks, we estimated that the dissociation ratio $d = 25\%$, in which 25% of the oxygen molecules of the saturated layer are dissociated thermally. Then, by comparing the intensity ratio i of the characteristic peak of the peroxo oxygen pump-probe spectra to the static atomic oxygen spectrum, the total excitation rate induced by the ultrafast pump pulses is equal to $i \times d$. The ratio of the peak intensities between the peroxo transient and the atomic static spectra is measured to be $i = 70\%$. Therefore, the total excitation rate of the peroxo oxygen state is about $70\% \times 25\% = 18\%$. At first glance this number seems to be surprisingly high. However, even higher excitation rates for molecules due to femtosecond laser pumping have been reported. For example, complete depletion of the adsorbed oxygen molecules by a single intense ultrafast pulse

has been reported to the system of O_2/Pt(111) [12], in which the fluence used was several orders of magnitude higher than in our experiment.

3.3.2.3 Energy transfer mechanism from nonthermal electrons to adsorbates

The excitation mechanism of the adsorbate – the coupling between the excited surface electron and the adsorbate – can be described on the microscopic scale by means of direct electron (hole) transfer process between the excited surface electron into the LUMO (HOMO) of the adsorbate.[3] The schematic drawing for the orbitals of superoxo and peroxo oxygen is shown in Fig. 3.11 [12, 87]. Several schemes of transfer processes have been proposed to explain the desorption processes induced by ultrafast pulses for adsorbates. In particular, for O_2/Pt(111), it has been proposed that the transition is due to the excited surface electron coupling to the unoccupied $3\sigma_u^{+*}$ level [77]; for O_2/Pd(111), hole transferring into the occupied part of the $1\pi_g^*$ level is an important process [88].

In the present case, we propose that an excited surface electron is transferred from the platinum surface to the unoccupied $1\pi_g^*$ orbital of oxygen, in which the orbital orientation is parallel to the platinum surface. There are two justifications:

1. Excitation to the $1\pi_g^*$ orbital is the most direct way to achieve the required charge configuration for the peroxo oxygen, in which its $1\pi_g^*$ orbital has one more electron when compared to the superoxo oxygen [69].

2. For the superoxo oxygen, the $\pi_{\|}$ orbital, which the $1\pi_g^*$ hybridized with the platinum d-band, is only half-filled and is located right at the Fermi-edge. Therefore, the observed high excitation level for this state transition can be explained because the

[3] LUMO = Lowest unoccupied molecular orbital, HOMO = Highest occupied molecular orbital

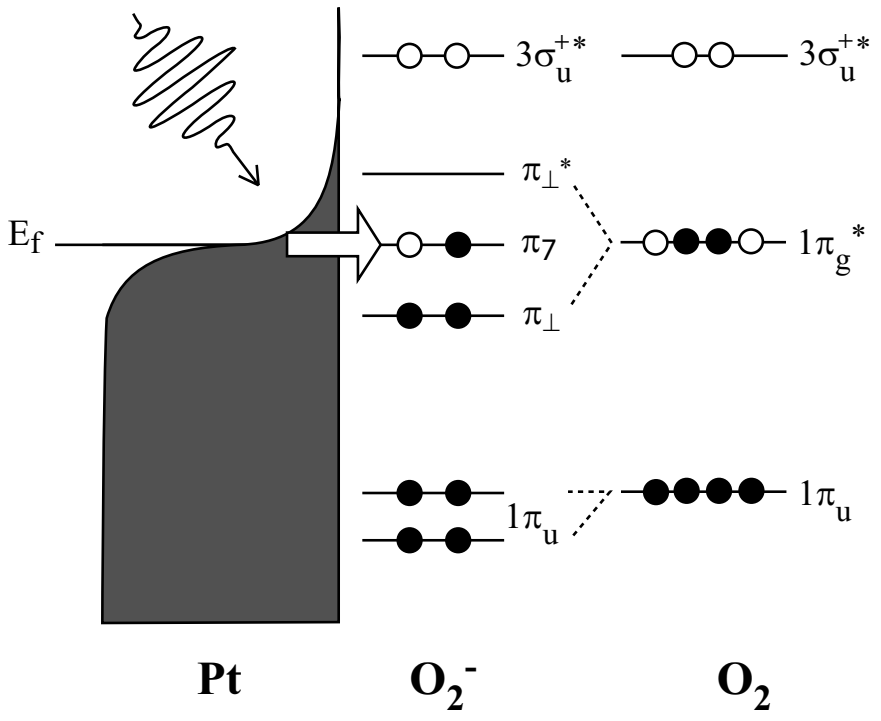

Figure 3.11: Because of the increased population of the surface electrons above the Fermi level induced by the ultrafast pump pulse excitation, the surface electrons will start to tunnel to the $1\pi_g^*$ orbital of the oxygen molecule and this leads to energy transfer to the oxygen center-of-mass.

excited surface electrons has the highest population at the Fermi-edge, and hence the transition probability for the excited surface electrons tunneling into the the $\pi_{\|}$ orbital can be very high. In contrast, since the $3\sigma_u^*$ orbital lies > 1 eV above the Fermi-edge, much fewer surface electrons will be able to reach this energy level for the same pump pulse intensity. If the electron transition into the $3\sigma_u^*$ is the correct mechanism, much higher laser intensities would be expected and be necessary to achieve the electron temperature needed [13].

3.3.2.4 Possible molecular motion during state transition

From the previous discussion, it becomes clear that excitation rate of the adsorbed oxygen by surface electrons reaches its highest level at the maximum temperature of surface electrons, which is several tens of femtoseconds after the pump pulse. After that, the excitation rate gradually decreases as the surface electrons cool. Therefore, the appearance of the transient peak-like feature at about 500 fs, which has a significant delay relative to the maximum electronic excitation of the oxygen molecules, does not reflect the electronic excitation level. Rather, this transient feature result from changes in the chemisorbed state accompanied by motions of the oxygen molecule. In general, the adsorption sites are the local minima of the potential energy surfaces (PES): for the superoxo oxygen, it is the bridge site, and for the peroxo oxygen, it is the hollow site. In addition, the PES defines the route for the transition between two chemisorbed states [69, 70]. For superoxo state to peroxo state, the oxygen will need to move from the bridge site to the hollow site (see Fig. 3.1). In order to move from the bridge site to the hollow site with the correct molecular orientation and configuration, the oxygen molecular motion could involve rotational

and vibrational motions. The oxygen molecule is pulled by the extra bond created when the hot surface electron transfers to the LUMO state of the oxygen molecule.

Theoretically, the rise time of the transient feature can be related to an effective coupling time τ_e between the surface electrons and oxygen center-of-mass motion by using a "frictional model" for the description of substrate-adsorbate interaction [85]. The typical value of the coupling time τ_e for direct energy exchange between the electron gas and the adsorbate lies in the range of a few 100 fs to several ps, in good agreement with our observations [8, 16, 89].

3.3.2.5 Decay channels for the excited state

The decay of the transient feature in several picoseconds can be interpreted as the actual lifetime of the meta-stable intermediate oxygen state. In case of the peroxo oxygen transformation, the decay can occur through molecular kinetic energy relaxation scattering with the surface electrons and phonons.

For our experiment, since the excited oxygen state (peroxo) is observed to relax to its ground state (superoxo) in about 5 ps, relaxation to the superoxo oxygen must be the dominant channel; however, it might not be the only possible decay channel. Typically, several different decay channels are present for conventional thermal excitation; For example, desorption and dissociation often co-exist. For excitation by ultrafast pulses, desorption and dissociation for the adsorbates are always observed together [8, 16, 89]. Therefore, the permanent feature shown in the photoemission spectrum of Fig. 3.8 after several hours of ultrafast excitation could likely result from the cumulative effects of slow oxygen desorption and dissociation. Since peroxo oxygen tends to be the preferred configuration for

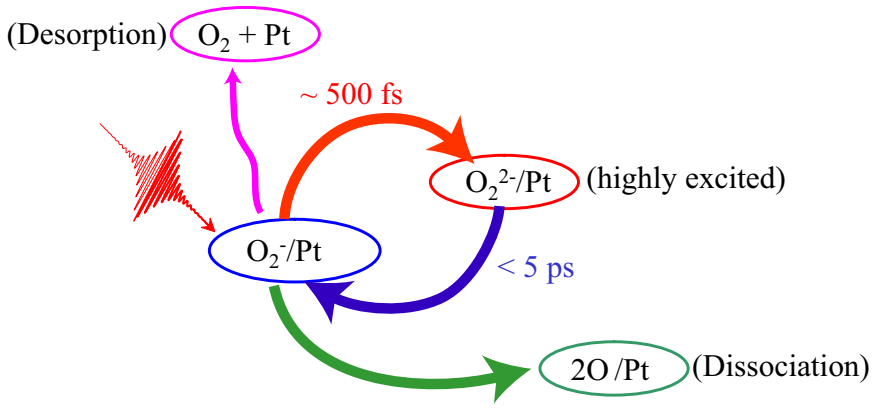

Figure 3.12: Possible reaction diagram of how oxygen molecules react after excited by an intense ultrafast pulse on the platinum surface

chemisorbtion at low surface coverage [75], a reasonable explanation for the permanent feature in valence band may result from slow desorption of oxygen over time and slowly increase the stable peroxo population on the platinum surface. Another explanation could be slow dissociation into oxygen atoms by the ultrafast pulses after extended pumping. However, it is unlikely that surface contamination causes this permanent feature, since the chamber is maintained in ultra high vacuum during the data taking, and the contaminant is not likely to contribute to the 6 eV peak that we observed.

3.4 Conclusion

After a lengthy discussion, a complete picture of how oxygen molecules adsorbed on Pt(111) surface response after the platinum surface is excited by an intense ultrafast pulse is illustrated in Fig. 3.12 [90, 91]. The oxygen molecules, originally residing on the bridge site as superoxo state (O_2^-) with one extra electron transferred from the platinum, are excited by the hot surface electrons to gain another electron from the platinum surface. After 500 fs, an extra chemical bond between the oxygen and platinum surface is created

due to the excess electron, and this pulls the oxygen molecule to the hollow site (peroxo O_2^{2-}). In about 5 ps, the excited oxygen will relax back to the bridge site (superoxo O_2^{-}) by giving up the excess electron to the platinum surface. In addition, slow desorption and dissociation happens on a longer time scale and ultimately reduces the molecular oxygen coverage.

CHAPTER IV

Probing adsorbate oscillation on metal surfaces

To date, studying molecular oscillations on metal surfaces has mainly been done in the energy domain. In order to measure vibrational modes of molecules absorbed on metal surfaces, energy loss techniques are typically used. In general, electron energy loss spectroscopy (EELS) is commonly used to measure the vibrational energies of normal modes in the higher energy range; for low energy modes, the technique of helium atom scattering is used instead because the high mass of the helium atom helps to resolve the small energy loss resulting from the scattering process. These techniques have successfully measured the vibrational frequencies of adsorbates, i.e. the metal-adsorbate vibrational mode energies and frustrated rotational mode energies, etc. However, it is not possible using these techniques to measure instantaneous excitation/de-excitation processes as a result of external "triggers" to molecules. For example, when a laser pulse irradiates molecules deposited on a metal surface, vibrational modes of the adsorbates can be triggered either due to the traditional phonon-induced (cw or nanosecond pulses), or hot surface electron-induced (femtosecond pulses) excitation. Moreover, it is unlikely that scattering experiments can measure how long the adsorbates will take for the vibrational process to start

after the excitation, and the time scale of the corresponding damping process. Therefore, time-domain measurements are needed as a complement to scattering experiment in order to reveal more information about dynamics.

Molecular vibrations are also very important for surface chemical reactions where molecules approach each other to react through various degree of vibrational motions, and electronic rearrangements. Therefore, in order to better understand some of the underlying mechanisms of surface chemistry, time-domain techniques are necessary to follow reactions at the molecular level in a step-by-step fashion.

Currently, time domain measurements are still very difficult due to a lack of appropriate techniques with both high surface sensitivity and high time-resolution (fs). In this chapter, we will demonstrate that by using the TR-UPS technique, and by varying the polarization of the incoming EUV probe pulses, it is possible to measure the vibrational frequencies of adsorbates on metal surfaces.

4.1 Photoelectric current affects by molecular symmetry and EUV polarization

In photoemission spectroscopy (PES), the transition probability of the photoelectric current produced in the PES process results from the excitation of electrons from an initial state with wavefunction ψ_i to a final state with wavefunction ψ_f by a photon field having the vector potential $\vec{A}$ (the direction of $\vec{A}$ is the same as the polarization $\vec{E}$ of the laser field). Hence, the transition probability (or photoelectron emission probability) w can be formulated using the Fermi-Golden Rule (or the first Born approximation) which assumes that the wavelength of the radiation is large compared to the dimensions of the excitation

volume [92],

$$w \propto \frac{2\pi}{\hbar} \left|\langle\psi_f|\hat{\mu}|\psi_i\rangle\right|^2 \delta(E_f - E_i - \hbar\omega) \tag{4.1}$$

where $\hat{\mu} = e\vec{r}$ is the permanent electric dipole moment and $\vec{r}$ has the same direction of the polarization of the laser field $\vec{E}$. Certain assumptions about the wavefunctions ψ_i and ψ_f can be legitimately applied in our case to simplify the transition matrix element $\langle\psi_f|\hat{\mu}|\psi_i\rangle$. The two wavefunctions (ψ_i and ψ_f) here are the full wavefunctions describing all the electrons in the system, and hence Eq. 4.1 is an equation for the many-body problem. For the first approximation, we can simplify this complicated many-body equation to a simple "one-electron" equation by neglecting effects caused by other electrons. The simplification for the initial and final state wavefunctions is explained in the following. For the final state, the adsorbate molecule is in the excited state with one less electron in the atomic core, plus a free electron with kinetic energy E_{kin}. Therefore, it is reasonable to approximate the initial-state wavefunction as a product of the single electron orbital $\phi_{i,k}$, from which the electron k will be excited, and write the wavefunction of the remaining electrons as $\psi^k_{i,R}(N-1)$, for the atom with N total electrons. Therefore, the initial-state wavefunction can be simplified to be –

$$\psi_i(N) = C\phi_{i,k}\psi^k_{i,R}(N-1) \tag{4.2}$$

where C is the normalization constant. By following this line of thought, the final state wavefunction ψ_f can also be simplified as a product of single-electron wavefunctions $\phi_{f,E_{kin}}$ of the photoemitted free electron and the remaining $(N-1)$ electron wavefunctions $\psi^k_{f,R}(N-1)$,

$$\psi_f(N) = C\phi_{f,E_{kin}}\psi^k_{f,R}(N-1) \tag{4.3}$$

Therefore, the transition matrix element of Eq. 4.1 can be separated into two terms,

$$\langle \psi_f | \hat{\mu} | \psi_i \rangle = \langle \phi_f | \hat{\mu} | \phi_i \rangle \left\langle \psi^k_{f,R}(N-1) | \psi^k_{i,R}(N-1) \right\rangle \tag{4.4}$$

The first term is the one-electron matrix element, and the second term is the $(N-1)$ electron overlap integral. The second term generally accounts for many other features in the photoemission spectrum, such as the core-level shifts and satellite peaks [92, 93], which are not considered here. Therefore, one can approximate that the remaining orbitals of the initial-state $\psi^k_{i,R}(N-1)$, and the final-state $\psi^k_{f,R}(N-1)$ to be identical. This approximation is often called the "frozen-orbital approximation", causing the second term to be approximated as $\left\langle \psi^k_{f,R}(N-1) | \psi^k_{i,R}(N-1) \right\rangle \approx 1$. The total transition matrix element now becomes very simple and results in a one-electron matrix element –

$$w \propto \langle \phi_f | \hat{\mu} | \phi_i \rangle \propto \langle \phi_f | \vec{r} | \phi_i \rangle \tag{4.5}$$

Since the photoelectric current measured by detectors is directly proportional to the photoelectron emission probability w, according to Eq. 4.5, the photoemission current is simply proportional to the integration of the single-electron wavefunctions of the initial orbital ϕ_i and the final free electron wavefunction ϕ_f, with the polarization of the applied electric field $\vec{r}$.

In this experiment, CO molecules are adsorbed on a platinum(111) surface, where CO is known to adsorb in the upright position (see next section). The CO molecule is a linear molecule and belongs to the symmetry point group of $C_{\infty \mathrm{v}}$. The corresponding character table of the point group $C_{\infty \mathrm{v}}$ is tabulated in Table 4.1. According to Eq. 4.5 and by using the terminology of group theory, for a given polarization $\vec{E}$, the photoelectron emission

$C_{\infty v}$	E	$2C_{\infty}^{\phi}$	$2C_{\infty}^{2\phi}$	$2C_{\infty}^{3\phi}$	$\cdots$	$\infty\sigma_v$	
$A_1 \equiv \Sigma^+$	1	1	1	1	$\cdots$	1	z
$A_2 \equiv \Sigma^-$	1	1	1	1	$\cdots$	-1	R_z
$E_1 \equiv \Pi$	2	$2\cos(\phi)$	$2\cos(2\phi)$	$2\cos(3\phi)$	$\cdots$	0	(x, y), (R_x, R_y)
$E_2 \equiv \Delta$	2	$2\cos(2\phi)$	$2\cos(4\phi)$	$2\cos(6\phi)$	$\cdots$	0	
$E_3 \equiv \Phi$	2	$2\cos(3\phi)$	$2\cos(6\phi)$	$2\cos(9\phi)$	$\cdots$	0	
$E_4 \equiv \Gamma$	2	$2\cos(4\phi)$	$2\cos(8\phi)$	$2\cos(12\phi)$	$\cdots$	0	
$\vdots$					$\vdots$		
$\Gamma_{x,y,z}$	3	$1+2\cos(\phi)$	$1+2\cos(2\phi)$	$1+2\cos(3\phi)$	$\cdots$	1	

Table 4.1: Character table of the symmetry group $C_{\infty v}$. (z is the direction of the principle symmetric axis)

probability $w \neq 0$ only when the direct product of the irreducible representations of the three functions (ϕ_i, ϕ_f, and $\vec{r}$) contains the totally symmetric irreducible representation[1] (Σ^+ in the case of $C_{\infty v}$) [94]. Mathematically,

$$\Gamma_{\phi_i} \otimes \Gamma_{\vec{r}} \otimes \Gamma_{\phi_f} \ni \Sigma^+ \tag{4.6}$$

or equivalently [95],

$$\Gamma_{\phi_i} \otimes \Gamma_{\vec{r}} = \Gamma_{\phi_f} \tag{4.7}$$

where Γ_{ϕ_i} denotes the irreducible representation of the function i. For normal emission of the photoelectrons, the emission direction is along the principle symmetric axis z, which corresponds to the irreducible representation Σ^+, according to Table 4.1. Since irreducible representation Σ^+ is totally symmetric, this simplifies Eq. 4.6 that $w \neq 0$ if the direct products of the $\Gamma_{\phi_i} \otimes \Gamma_{\vec{r}}$ contains Σ^+.

The polarization of the EUV probe pulses then affects the symmetry of $\Gamma_{\vec{r}}$. According to Table 4.1, for p-polarized EUV pulses, where the polarization of the pulses is parallel to the plane of incidence (z in the character table), $\Gamma_{\vec{r}} = \Sigma^+$. For s-polarized EUV

[1] An irreducible representation is a totally symmetric irreducible representation when the characters for all symmetric operations is equal to 1.

$C_{\infty v}$	Σ^+	Σ^-	Π	Δ	Φ	Γ	$\cdots$
Σ^+	Σ^+	Σ^-	Π	Δ	Φ	Γ	
Σ^-		Σ^+	Π	Δ	Φ	Γ	
Π			$\Sigma^+ + [\Sigma^-] + \Delta$	$\Pi + \Phi$	$\Delta + \Gamma$	$\Phi + \mathrm{H}$	
Δ				$\Sigma^+ + [\Sigma^-] + \Gamma$	$\Pi + \mathrm{H}$	$\Delta + \mathrm{I}$	
Φ					$\Sigma^+ + [\Sigma^-] + \mathrm{I}$	$\Pi + \Theta$	
Γ						$\Sigma^+ + [\Sigma^-] + \mathrm{K}$	
$\vdots$							

Table 4.2: Table of the direct product ($\otimes$) of the symmetry group $C_{\infty v}$

pulses, the polarization of the pulses is perpendicular to the plane of the incidence (x or y in the character table) and $\Gamma_{\vec{r}} = \Pi$. Table 4.2 is the direct product table for the symmetry group $C_{\infty v}$. According to this table, for an orbital with σ symmetry ($\Gamma_{\phi_i} = \Sigma^+$), p-polarized EUV pulses ($\Gamma_{\phi_{\vec{r}}} = \Sigma^+$) are needed to have a non-zero photoelectron emission probability ($\Sigma^+ \otimes \Sigma^+ = \Sigma^+$). On the other hand, for an orbital with π symmetry ($\Gamma_{\phi_i} = \Pi$), s-polarized EUV pulses ($\Gamma_{\phi_{\vec{r}}} = \Pi$) are required ($\Pi \otimes \Pi = \Sigma^+ + [\Sigma^-] + \Delta$ contains Σ^+). Therefore, by changing the polarization of the EUV pulses, molecular orbitals with different symmetries can be selectively enhanced or suppressed in the photoemission spectrum. More detail discussion about the relation between the angular pattern of emitted photoelectrons and the laser polarization can be found in Ref. [95].

4.2 Symmetry of the orbitals of CO/Pt(111)

As mentioned in the previous paragraphs, CO is adsorbed on the Pt(111) surface for this experiment. The platinum surface is routinely cleaned with argon sputtering and oxygen annealing. After the platinum surface is cleaned, 5 L of CO is introduced onto the surface through a gas doser to achieve a saturation CO coverage of 0.5 ML. At this coverage, the CO molecules equally occupy the bridge $\nu_b(\mathrm{C-O}) = 232$ meV and atop sites

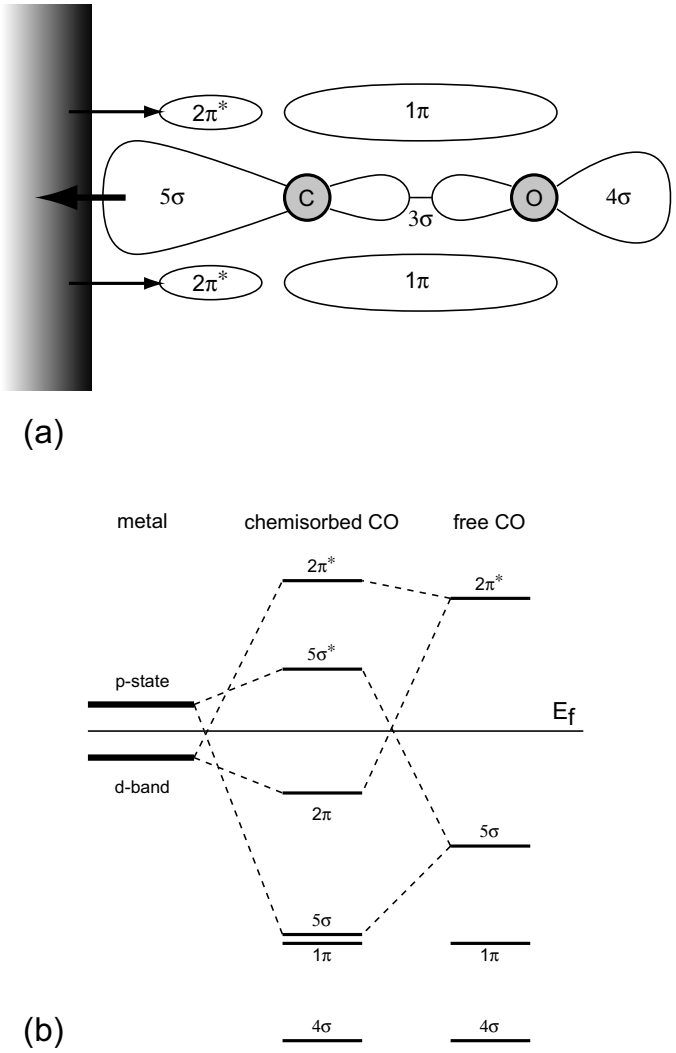

Figure 4.1: Schematic diagram showing the bonding character of a CO molecule adsorbed on a metal surface. (a) The CO-metal bond is provided by the most extended orbital of the molecule which is the 5σ orbital. Charge back donation from the metal into the formerly empty $2\pi^*$ orbitals is indicated by thin arrows. (b) Schematic energy level diagram of the CO-metal system. The energy levels on both sides are for the isolated CO molecule and the metal surface. The middle diagram illustrates the energy levels of an adsorbed CO molecule. Band splitting for the adsorbed CO happens for the 5σ and $2\pi^*$ levels due to hybridizaton with the metal d-band and the p-orbitals. (figures reproduced from Ref. [92])

$\nu_t(\mathrm{C}-\mathrm{O}) = 258$ meV, producing a $c(4\times 2)$ LEED pattern [75, 13]. The CO molecules adsorb in an upright position with the intermolecular axis perpendicular to the metal surface, with the carbon atom at the bottom bonded to the metal surface, while the oxygen atom resides on top. Figure 4.1(a) illustrates the outermost molecular orbitals of the CO molecule and indicates how the CO molecule binds to the platinum surface. The energetically highest occupied orbital and thus also the spatially most extended one is the 5σ orbital which is located mainly on the carbon atom. Therefore, it is intuitively reasonable that the CO molecule tries to attach its "softest" part to the metal surface in the surface chemical bond. The initial step in binding is therefore a 5σ-to-metal charge transfer. This charge transfer is compensated partly by back donation of charge from the metal surface onto the CO molecule. This back donated charge is into an orbital that is a mixture of the $2\pi^*$ of the free CO molecule with the metal d-band [96]. It is interesting to note that in the free CO molecule, the $2\pi^*$orbital is about 1.5 eV above the vacuum level E_v,and the hybridizaton with the metal d-band causes it to locate below E_v [97].

Figure 4.1(b) illustrates the energy levels of the orbitals for free CO molecules and chemisorbed CO molecules on metal surfaces. When CO molecules are brought into contact with a metal surface, the 5σ orbital of the CO molecule interacts with the p-orbital of the metal atoms, splitting the 5σ orbital into a bonding and an anti-bonding state. The resulting bonding state is energetically only slightly higher than 1π orbital, in contrast to its much higher energy position originally. The $2\pi^*$ orbital also interacts with the d-band causing a splitting into a bonding and an anti-bonding state. The bonding state is located well below the Fermi-edge E_f in energy, and hence provides a back donation channel for

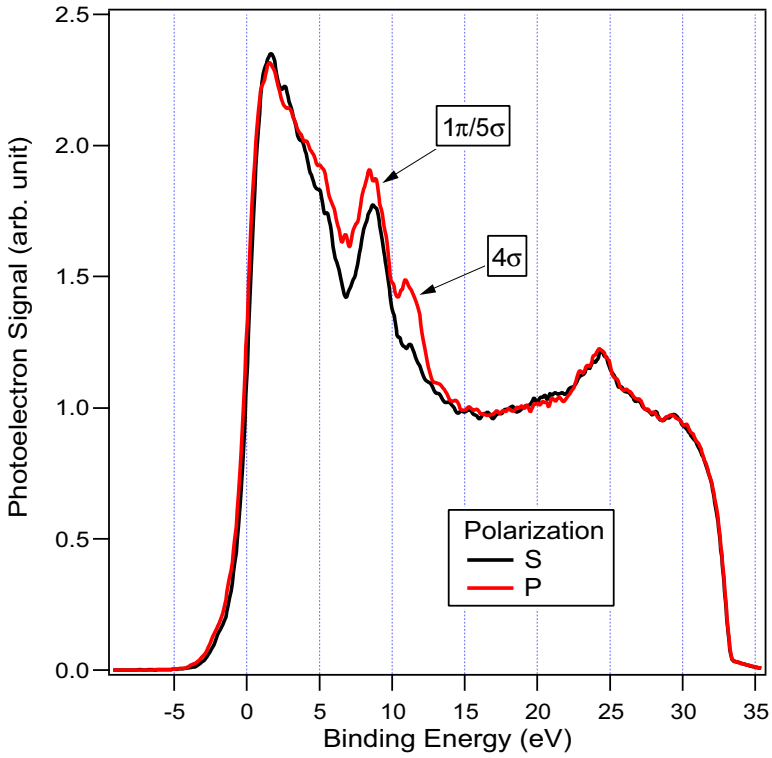

Figure 4.2: Photoemission spectrum of CO molecules adsorbed on a platinum(111) single crystal surface. Spectra are taken with high harmonic photons (42 eV) with different s (black) and p (red) polarizations.

charge transferring from platinum to the CO molecule.

As pointed out in the previous section, the orbital symmetry of the CO molecules results in different photoemission cross-sections depending on the polarization of the exciting EUV light. Figure 4.2 plots the photoemission spectra of CO on Pt(111) using s and p polarized EUV probe pulses without pump beam excitation, i.e. the so-called "static" spectra. The two spectra show significant similarities in both the high and low binding energy regions. However, in the energy range from 5 to 15 eV, noticeable differences are caused by the different polarizations of the EUV probe pulses. Comparing with the energy level diagram of the chemisorbed CO on Fig. 4.1(b), the peak at 9 eV binding energy can be assigned to the $1\pi/5\sigma$ orbital combination – the energy lowering of the 5σ

orbital caused by hybridizaton with the metal d-band, results in a 5σ bonding state that is indistinguishable with the 1π orbital in energy. As shown in Fig. 4.2, there are changes in intensity for the $1\pi/5\sigma$ peak when using different EUV polarizations. However, since the 1π and the 5σ orbitals are so close in energy after adsorption, it is difficult to use this peak to analyze the CO orientation.

There is another peak at a 12 eV binding energy that can be assigned to the 4σ orbital. It has very different emission cross-sections for the two different EUV polarizations. As shown in Fig. 4.2, the 4σ peak is greatly suppressed for s-polarized light, as expected due to the symmetry selection rule explained in the previous section. This kind of complementary behavior of σ and π emissions was first observed by Plummer *et al.* for CO/Ni(111) [98] and has been used to determine the geometry of the adsorbed molecules on metal surfaces [95]. There is still a little reminant of the 4σ peak in the case of s-polarized light. This is because the TOF detector is mounted about 30° off the surface normal. Although the ideal case would be to mount the TOF detector normal to the sample, the off-normal mounting has a negligible affect on the photoemission yield for the 4σ peak and therefore does not affect the overall experiment.

4.3 Resolving oscillations of adsorbed CO molecules

In the previous sections, it has been shown that there is a dependence of the photoelectron emission cross-section on the EUV polarization. Therefore, it is possible to use this property to measure the oscillation period of the adsorbate after excitation by an ultrafast pulse. After the surface is excited by an ultrafast pulse, hot electron tunneling from the substrate to the adsorbate can occur. The excited electrons raise the potential energy surface

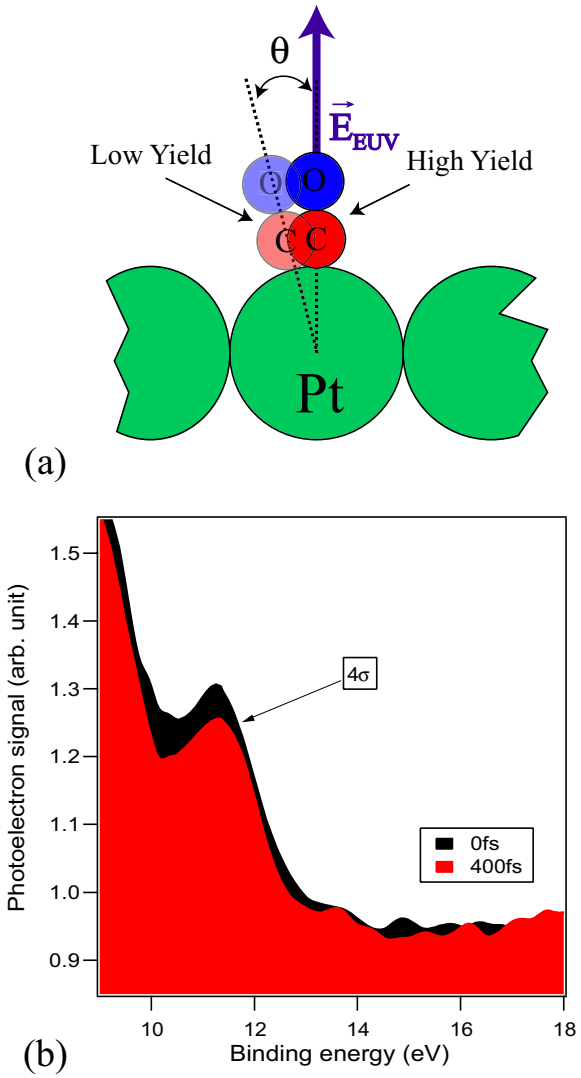

Figure 4.3: (a) Schematic diagram illustrating that when the CO molecules are aligned with the polarization of the EUV pulse, the photoemission cross-section is maximized. After excitation by an ultrafast laser pulse, the CO molecules start to vibrate. When the CO molecules slightly non-parallel to the EUV polarization, the photoemission cross-section is reduced. (b) Pump-probe spectra close to the 4σ peak. These spectra are taken when the polarization of the EUV probe pulses is perpendicular to the platinum surface (p-polarized) , and the polarization of the excitation pump pulses are parallel to the surface (s-polarized) with $15\mu\mathrm{J/mm}^2$/pulse fluence. Spectra of 0 fs and 400 fs time delays are shown for comparison, showing that the the 4σ peak in both height and area at 0 fs time delay are bigger than those at 400 fs time delay.

of the adsorbate and transfer energy to the atomic center-of-mass – causing the molecule to vibrate, or even desorb, depending on the excitation energy. For CO on Pt(111), the $2\pi^*$ orbital is close to the Fermi-edge E_f. Hot electrons can tunnel to $2\pi^*$ orbital to transfer energy, in a process similar to DIET/DIMET. Actually, inverse photoemission spectroscopy (IPES) has measured the $2\pi^*$ orbital to be about 1.5 eV above the Fermi-edge for CO on Ni(111) [99], providing a channel for electronic tunneling to the CO. By fixing the polarization of the laser pulse in one particular polarization, e.g. p-polarized, as illustrated in Fig. 4.3(a), the CO molecules could start to vibrate. According to Eq. 4.5, the photoemission cross-section of a particular orbital is directly related to the overlap between the polarization of the EUV pulses and the "direction" of the wavefunction $\phi_{i,k}$ of that orbital; or in the other words, the photoemission cross-section w of the CO 4σ bond is a function of how well the bond lines up with the laser polarization. By using this simple idea, the oscillation period of the CO molecules can readily be measured by performing a series of pump-probe scans by following the intensity changes of the 4σ peak.

Figure 4.3(b) shows the pump-probe spectra at time delays of 0 fs and 400 fs around the energy region of the 4σ peak. It is clear that the 4σ peak at 400 fs time delay is lower in both height and area when comparing to the 4σ peak at 0 fs time delay. This change is expected because at 0 fs time delay, the CO molecular axis should still be parallel to the polarization of the EUV light, giving a maximum intensity for the 4σ peak. At a time delay of 400 fs, the CO molecules are no longer parallel to the polarization of the EUV light, and the photoemission signal decreases accordingly.

The oscillation period of the CO molecules can be obtained by integrating the area of

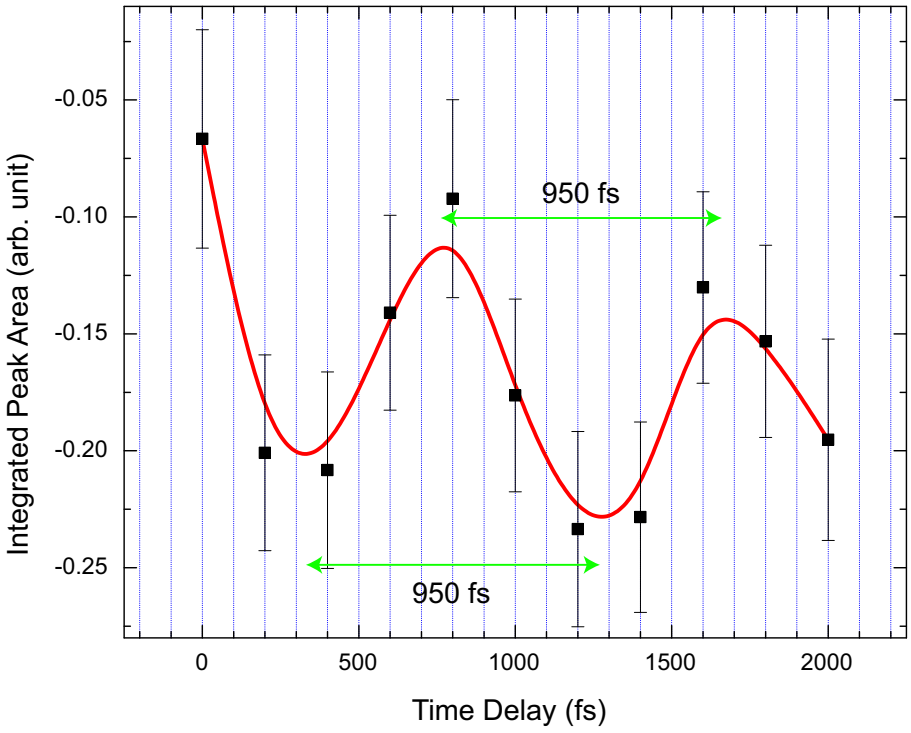

Figure 4.4: Integrated area of the 4σ peak of the CO/Pt(111) plotted at various time delays, showing that the CO molecules are oscillating at the platinum surface after pump pulse excitation.

the 4σ peak as a function of time delay between pump and probe. The spectra at various time delays are first subtracted from a reference spectra at -100 fs, and the remaining signals are then integrated over the binding energy of the 4σ peak. By plotting these integrated areas versus time delay, a nice oscillatory curve is obtained, as shown in Fig. 4.4. The oscillation period is measured to be about 950 fs, when measured either at the maxima or minima of the oscillation signal. Also, in Fig. 4.4 the oscillation signal tends to decrease at longer delay times. This effect is expected since the vibrational energy of the CO molecule can slowly transfer to the platinum surface, reducing its oscillation amplitude accordingly.

Further information can be revealed at the Fermi edge. Fig. 4.5 shows the photoemission spectra at the Fermi-edge at the time delays of 0, 100, 200, and 500 fs respectively. It is obvious that the photoemission yield at 0 fs is significantly higher than for the rest of the photoemission spectra. This indicates that a significant population of non-thermal electrons are created by the pump pulse. These non-thermal electrons are still distinguishable at 100 fs, but by 200 fs, the electron distribution has cool significantly. This is similar to our previous observation on oxygen at Pt(111) – the hot electrons distribution is significantly reduced by about 200 fs.

4.4 Discussion

4.4.1 CO normal modes on a platinum surface

In the gas phase, a molecule can have $3N$ degrees of freedom, which can be divided into three translational, 3 rotational and $3N-6$ vibrational modes (for linear molecules, 2 rotational and $3N-5$ vibrational modes). N is the number of atoms in the molecules.

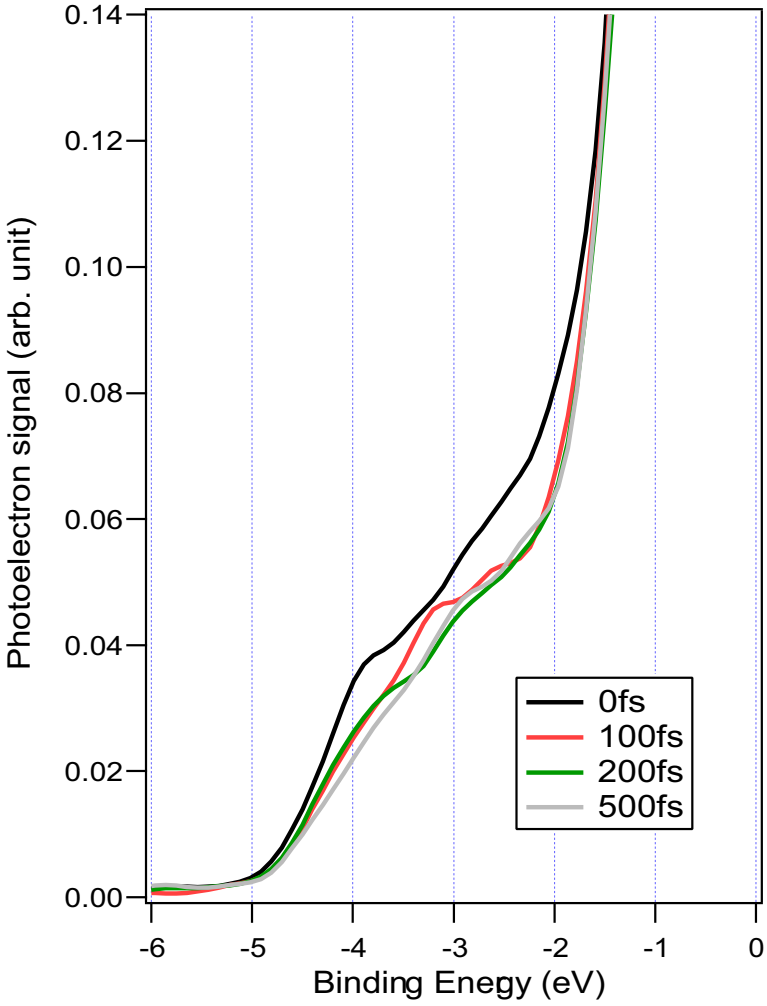

Figure 4.5: Pump-probe spectra near the Fermi-edge, showing that hot electrons are rapidly excited when the ultrafast pump pulses excites the surface. They subsequently relax in about 200 fs. There is a static component resulting from a small residual 29^{th} harmonic.

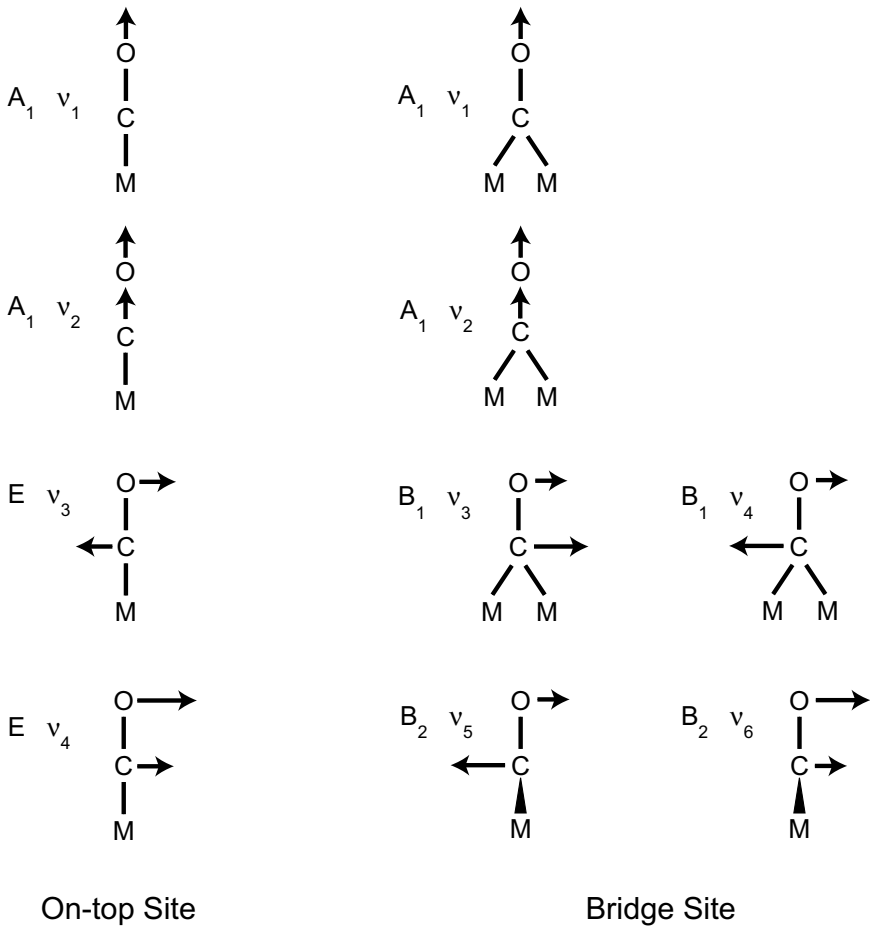

Figure 4.6: Schematic representation of the normal modes of on-top and bridge-bonded CO on platinum surface. The relative length of the arrows represent the movements of the carbon and oxygen atoms. (figure adapted from Ref. [100] and Ref. [101])

When molecules adsorb on surfaces, all translational and rotational motions are restricted, so the $3N$ degrees of freedom are all vibrational modes. These vibrational modes are best classified as 3 frustrated translations, in which the molecule, as a whole, moves perpendicular or parallel to the surface, 3 (2 for a linear molecule) frustrated rotations, and finally $3N-6$ ($3N-5$for linear molecule) vibrational modes.

For classification purposes, point group symmetry can be used to associate the CO adsorption to the top site and the bridge site on the platinum surface. The top site gives the C_{4v} point group, and the bridge site gives C_{2v} point group. Fig. 4.6 shows schematically the form of localized vibrational modes for CO on Pt(111) on the on-top and bridging position. In each case, there are two modes belonging to the totally symmetric A_1representation, which have their dipole moment changes normal to the surface. Hence, ν_1 is closely related to the free molecule C-O stretching mode. ν_2 is a hindered translation mode normal to the platinum surface, which becomes essentially a Pt-C stretching mode. The remaining four modes – the x and y frustrated translations and the frustrated rotations appear as degenerate pairs for the top site CO molecules; but in the bridge site, the degeneracy is lifted and results in two modes, ν_3 and ν_4, in the plane of the bridge site, and two modes, ν_5 and ν_6, perpendicular to the plane of the bridge site.

These vibrational modes can be measured using energy loss methods. In general, infrared spectroscopy (IRS) and electron energy loss spectroscopy (EELS) have been employed successfully for measuring adsorbate vibrational frequencies with energies above 200 cm^{-1} [102, 103]. For vibrational energy lower than this range, a helium atom scattering technique is employed to investigate the low frequency modes [104, 105, 101]. In

	normal node energy (cm^{-1})		oscillation period (fs)	
	on-top site	bridge site	on-top site	bridge site
C-O stretch ν_1	2100	1871	16	18
Pt-CO stretch ν_2	480	361	72	92
CO frustrated rotation ν_3	411 *		81	
CO frustrated translation ν_4	48	59	696	566

Table 4.3: Normal mode energies of CO adsorbed on Pt(111) (* calculated for CO/Ni)

particular, for CO adsorbed on Pt(111) at a low coverage of CO ($\leq 1/3$ mono-layer), CO molecules mainly occupied on the on-top sites. The high frequency C-O stretching mode ν_1 is measured to be 2100 cm^{-1}(258 meV), and the Pt-C stretching mode ν_2 is at a relatively lower frequency, estimated to be 480 cm^{-1}(58 meV) by EELS [75, 106]. When the CO coverage increases to 0.5 mono-layer and above, the bridge sites will start to be filled by the CO molecules. Therefore, the EELS spectrum will start to develop two new additional loss peaks at slightly reduced energies at 1871 cm^{-1} (232 meV) and 361 cm^{-1} (45 meV), corresponding to the C-O stretching mode and the Pt-C stretching mode at the bridge sites respectively. The CO frustrated rotation mode ν_3 has been calculated for CO adsorbed on Ni, and the calculated value is 411 cm^{-1} (51 meV), which is in the same order of magnitude as the ν_2 mode. (For the other two modes calculated for CO/Ni: $\nu_1 = 2088\,\mathrm{cm}^{-1}$ (259 meV), and $\nu_2 = 437\,\mathrm{cm}^{-1}$ (54 meV). These are similar to the measured value of CO adsorbed on Pt, and hence, it is reasonable to believe that the ν_3 of CO/Pt(111) has a similar value) [100]. Finally, for the frustrated translation mode ν_4, helium scattering experiment measured the value to be 48 cm^{-1} (6 meV) for the top site, and 59 cm^{-1} (7 meV) to the bridge site [101, 107].

The oscillation periods of these modes can be calculated from the measured energies. Assuming that all normal modes of the adsorbates are harmonic oscillators, then the vi-

brational energies can be written as

$$E_n = (n + \frac{1}{2})\hbar\omega \tag{4.8}$$

where n is the quantum number of the normal mode, and $\omega = 2\pi/\tau$ is the angular frequency, and τ is the oscillation period. For energy loss experiments, the measured energy is the energy difference between the ground state ($v = 0$) and the excitation state ($v = 1$), and hence, the vibrational period can be converted from the measured energy by

$$\tau = h/E_{measured} \tag{4.9}$$

The energies of the four normal modes of the the CO/Pt(111) and their corresponding converted oscillation periods are tabulated in Table 4.3.

Considering all of the vibrational modes of CO/Pt(111), the oscillation period corresponding to the frustrated translation mode ν_4 ($\tau_4 = 696$ and 566 fs) is the closest one to the period we measured using TR-UPS ($\tau_{\mathrm{TR-UPS}} \simeq 950$ fs). All the other mode periods are more than an order of magnitude shorter in time than the period measured. In fact, the frustrated translation mode ν_4 and the frustrated rotation mode ν_3 should be most sensitive to the polarization of the EUV pulses, due to the fact that these modes directly affect the orientation of CO molecules on the platinum surface, and subsequently affect the orientation of the 4σ orbital. For the frustrated rotation mode ν_3, one would expect another oscillation period on the order of 100 fs should be observed and that this fast period should be superimposed on the slow varying oscillation period of ν_4. However, preliminary study of measuring the variation of the 4σ peak with a finer time resolution does not reveal another oscillation feature, indicating the possibility that the ν_3 mode might not be as easily

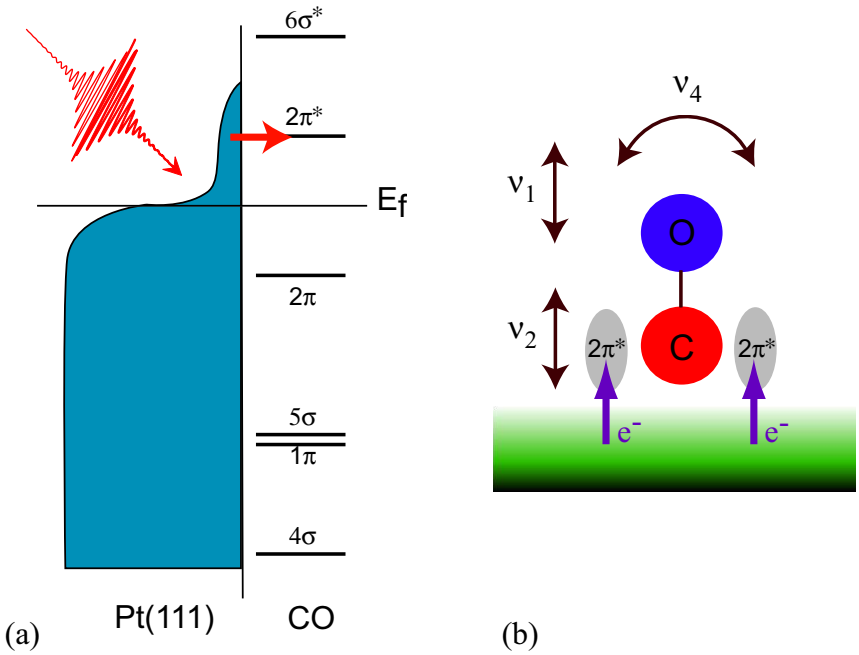

Figure 4.7: (a) When an ultrafast pulse excites the platinum surface, hot electrons are created on the surface. The hot electrons then tunnel to the $2\pi^*$ orbital of the CO molecule. (b) Due to the bonding character to the platinum surface of the $2\pi^*$ orbital, the C-O vibrational mode ν_1 and the CO-Pt vibrational mode ν_2 will be induced. The frustrated translation mode ν_4 could either be directly excited by the hot electron, or subsequently excited due to energy coupling between modes.

excited as the frustrated translation ν_4. In fact, in energy loss spectroscopy, in our knowledge, the ν_3 mode has not been observed experimentally. This might be an indication that the potential energy surface of the CO/Pt(111) system might prohibit the excitation of the CO frustrated rotation mode ν_3 effectively.

4.4.2 Hot electrons mediated excitation

The excitation mechanism of the ν_4 mode related to hot surface electrons that are created and sustained within the first 200 fs after pump pulse excitation. As shown in Fig. 4.4, the oscillation begins immediately after pump pulse excitation, and the 4σ orbital reduces its intensity significantly by a 200 fs time delay. According to the two temperature model

discussed in the last chapter, the surface electrons respond to ultrafast pulse excitation almost instantaneously through directly adsorbing the ultrafast pulse energy which could subsequently raises the electron temperature to several thousand Kelvin, depending on the pump pulse intensity and pulse-width. However, the surface lattice cannot directly respond to the ultrafast pulse excitation, and remains relatively "cold" for picoseconds. If the CO excitation is phonon-mediated, as in conventional surface chemistry, a time delay of picoseconds would be expected before the onset of oscillation. Therefore, once again, the hot surface electrons created by ultrafast pulses play an important role in the CO excitation observed.

For CO on Pt(111), the unoccupied $2\pi^*$ orbital is close to the Fermi-level. Since the photon energy of our pump pulse is 1.5 eV, the hot surface electrons will be excited to 1.5 eV above the Fermi-edge. Therefore, these hot electrons will have sufficient energy to reach this unoccupied CO orbital through tunneling, as shown in Fig. 4.7. In fact, the $2\pi^*$ orbital is an anti-bonding orbital with respect to the bonding between carbon and oxygen atom; on the other hand, occupying the $2\pi^*$ orbital would enhance the bonding strength between the platinum surface and the CO molecule.

Therefore, after the hot surface electron transfers to the $2\pi^*$ orbital of the CO molecules, the potential energy surface (PES) of the CO molecules is suddenly excited through Fanck-Condon excitation. The nuclei of the CO molecules are not positioned at the energy minimum of the excited PES, and the nuclei will be driven along the excited PES to new positions. Therefore, the distance between the carbon atom and the oxygen atom will be increased, and the distance between the CO molecule and the platinum surface will be-

come shorter. Typically, these hot electrons will only stay on the adsorbates for a time scale of about 10 fs, as discussed in the studies of unoccupied state lifetime of adsorbates using two-photon photoemission techniques from Sec. 1.3. After the hot electrons leave the $2\pi^*$ orbital of the CO, the PES will be relaxed to the ground-state, and the carbon and oxygen atoms are now required to reverse their courses. Because of these motions, the energy of the hot electrons is partly transferred to kinetic energy of the nuclei. Hence electron transition processes result in launching vibrations for two normal modes ν_1 and ν_2. This picture is very similar to the DIET/DIMET process of desorption by ultrafast pulse. Hot surface electrons transfer energy to molecular motion through the excited potential energy surface by Franck-Condon excitation, as discussed in the appendix.

The excitation of the frustrated translation mode ν_4 could be due to subsequent mode coupling between the highly excited modes ν_1 and ν_2 with ν_4, or could be due to direct excitation by the hot surface electrons, or even a mix of the two mechanisms. If the former is true, then the coupling time between the normal modes should be fairly "fast" in order to explain the quick onset of the observed oscillation signal. Further investigation on this process will be needed in order to fully understand the excitation mechanism of the ν_4 mode.

Finally, the oscillation period we measured using TR-UPS is about 950 fs, which is longer than the numbers measured by helium atom scattering experiments (696 and 566 fs). In fact, for the technqiue of time-resolved vibrational sum-frequency generation, as discussed in Sec. 1.5.2, a strong transient redshift of the vibrational energy for the C-O stretch mode has been observed after ultrafast pulse excitation, . The vibrational energy

is shifted from $\sim 2020\ \mathrm{cm}^{-1}$ to $\sim 1980\ \mathrm{cm}^{-1}$ and persists for more than 20 ps, as shown in Fig. 1.10(b). They explained this effect is cause by anharmonic coupling of the C-O strech mode to low-frequency frustrated modes [36, 35, 108, 109]. Further investigation is needed to clarify how this energy redshift happens.

4.5 Conclusion

In this chapter, measuring the vibrational period of an adsorbate in the time domain has been demonstrated using the symmetry of the molecular orbitals and the polarization of the EUV ultrafast pulses. In particular, the CO frustrated translation mode ν_4 is measured to be about 950 fs, similar to results obtained using helium scattering techniques in the energy domain. Actually, CO translational motion has been proposed to be very important to the CO oxidation process on metal surfaces, as well as the rotational motions of the O_2 molecules, as reported in the last chapter. Density functional calculations [68, 110, 103] have suggested that in the beginning of the CO oxidation process, oxygen molecules rotate from the bridge site to the hollow site in order to elongate the intermolecular bond between the two oxygen atoms. This results in dissociation into two oxygen atoms with lower dissociation energy. Simultaneously, CO molecules translate and bend towards the oxygen molecules (or atoms) to "attract" one of the oxygen atoms to recombine with it and finally leave the surface as CO_2. If this picture of CO oxidation is correct, then the two measurements that we performed of O_2/Pt(111) and CO/Pt(111) support observation of the first steps in the suspected mechanism of CO oxidation.

CHAPTER V

Future work

In previous chapters, we have demonstrated that TR-UPS is a powerful tool in the investigation of chemical dynamics of adsorbates on metal surfaces. This technique has great potential for revealing many of the intermediate steps of surface chemical reactions and their corresponding time scales. Thanks to this capability, future studies based on TR-UPS may provide significant insights into the mechanisms behind many catalytic processes. The results from these studies may give theorists a better theoretical understanding of catalytic processes on the atomic level. However, to date, both experimental and theoretical studies of the dynamics of surface chemical reactions are still in their infancy, and tremendous efforts will be required in this emerging field in the future. Hopefully, someday, the understanding will be mature enough to apply the knowledge obtained to engineering processes leading to cheaper and more robust catalysis. In the following chapter, several proposed improvements to the experimental setup and possible future work will be discussed. Our hope is that these ideas will be realized in our laboratories in the coming two to three years.

5.1 Time-resolved core-level spectroscopy

The photon energy of the high-harmonic generated EUV pulses used in our current TR-UPS setup is 42 eV (30 nm wavelength). The reasons for choosing this photon energy are its relatively high flux, and ease of generation, with relatively less driving laser intensity required. The 42 eV photon energy is sufficient for probing valence-band structure; however, liberating electrons from core-level orbitals will require higher photon energy. For example, the binding energies of the $1s$ (deep core-level) and $2s$ (shallow core-level) orbitals for oxygen atoms are 543 and 41.6 eV, respectively [111].

Core-level photoemission spectroscopy (or XPS) is a common technique for determining both physisorbed and chemisorbed states of adsorbates on metal surfaces. Since photoelectrons from the core levels are very sensitive to the surrounding chemical environment, XPS is widely used to study static physical phenomena on surfaces using synchrotrons. UPS is generally used to observe changes in molecular valence bands, which gives information about the dynamics of adsorbate bonding structure. XPS, on the other hand, is used to observe energy shifts of the core-level electrons, giving site-specific information about molecules in different chemical environments. Therefore, pushing the EUV photon energy to higher values will allow us to obtain more information about the system, using both UPS and XPS. Information obtained using each technique can help us to better understand the dynamics of chemical reactions.

Generally speaking, photon energy in the range of 30 to 200 eV has good surface sensitivity, since the escape depth of electrons in this energy range is under 5 Å [2]. The current record high-harmonic-generation photon energy is 460 eV (2.7 nm) using helium,

and 239 eV (5.2 nm) using neon, using a pulsed gas jet and tera-watt ultrafast pulses [3]. However, though high-harmonic generation in these high energy ranges is possible, efficient high-harmonic generation has only been demonstrated for photon energies on the order of 50 to 100 eV. To efficiently generate photons of higher energies, higher laser intensity is needed. The high laser intensity, however, leads to a higher degree of ionization of the interacting gas molecules, preventing the driving laser and the EUV light from propagating at the same speed, severely limiting the conversion efficiency. Recent results from our group have shown that by using a modulated hollow-core waveguide to periodically vary the intensity of the driving laser pulses, one can achieve efficient EUV generation even in the presence of substantial ionization. The immediate result of this work is to the shifting of the phase-matching condition to even higher photon energies. About 20 pJ generated intensity has been obtained for individual harmonics at around 100 eV photon energy using this corrugated capillary method [5]. In addition, high quality multi-layer mirrors are much easier to fabricate around 95 eV (13 nm) photon energy with mirror reflectivity better than 75% achievable, in contrast to only 25% reflectivity at around 42 eV (30 nm). Therefore, although high harmonic generation at 100 eV will have ~ 1 order of magnitude less flux than at 42 eV, higher reflectivity multi-layer mirrors can compensate for the lower generated flux, giving a comparable detected signal level.

5.2 Probing bimolecular chemical reaction on surfaces

The work presented in chapter III demonstrated that TR-UPS allows direct observation of chemical reactions on metal surfaces. We saw that when oxygen molecules rotate from the bridge site to the three-fold-hollow site on platinum, a covalent bond between the

surface and the oxygen is created, weakening the intra-molecular bond between the two oxygen atoms. This type of bond creation is generally considered to be one of the simplest chemical reactions. However, completely time-resolving bimolecular chemical reactions on surfaces has long been a major challenge for surface chemists. In particular, by identifying all the precursor states and their reacting time-scales, the reaction "bottleneck" can then be pin-pointed, perhaps improving the efficiency of the chemical reactions.

CO oxidation (2CO + $O_2 \rightarrow 2CO_2$) on platinum surfaces is a good candidate system for such experiments. Theoretical calculations have been performed on CO oxidation on the platinum(111) surface [103, 68]. These calculations suggest that peroxo oxygen molecules (O_2^{2-}) have a lower activation barrier for reacting with CO molecules than superoxo oxygen molecules (O_2^{-}). This is possibly due to the fact that peroxo oxygen has a longer O-O intra-molecular bond, and since peroxo oxygen molecules have a less corrugated potential energy surface around the hollow site, the more preferable site for chemical reactions [68]. Therefore, the catalytic channel for the platinum surface is likely to be that the platinum surface provides a dissociation pathway for the oxygen molecules, allowing oxygen molecules to move from the bridge site to the hollow site, and lowering their dissociation energy. Subsequently, the intermolecular bond cleaves, creating two excited oxygen atoms. The excited oxygen atoms can then directly react with CO molecules, finishing the oxidation process. Finally, the CO_2 molecule will leave the platinum surface, releasing the adsorption sites for another O_2 and CO molecule pair to undergo the catalytic process again.

If this picture of CO oxidation is correct, observing this process could be possible using

TR-UPS. One possible scheme for using TR-UPS to obverse the spectral changes could be to look for the characteristic peak of the peroxo oxygen to appear about half a picosecond after the pump pulse arrives, indicating the movement of the oxygen molecules from the bridge site to hollow site. In the meantime, the 4σ and $1\pi/5\sigma$ features of CO molecules could be used to monitor the orientation of CO molecules. In addition, the strength of the CO peaks should diminish for longer times, due to desorption of the CO_2 molecules from the platinum surface after the oxidation process. Therefore, hopefully, CO oxidation may be time-resolved using TR-UPS (or TR-XPS).

5.3 Angle- and time-resolved photoemission spectroscopy

Currently, the TR-UPS setup cannot resolve the emission angles of photoelectrons emitted from the sample surface. In many surface science experiments, resolving the emission angle is not critical to understanding the details behind the mechanism under study. However, for some experiments, knowing angular information will significantly improve our understanding of the experimental details. For example, in the experiment observing CO oscillation periods on a platinum surface (chapter IV), photoelectrons originating from the 4σ orbital would have an emission peak along the intra-molecular axis. Therefore, if photoelectron angular information were available, a clearer picture of the CO molecular oscillation would emerge, allowing, for example, precise determination of the oscillation angle of the CO molecules.

In synchrotron-based photoemission experiments, two-dimensional hemispherical electron analyzers have recently been used to obtain precise angular distributions of emitted photoelectrons. Traditionally, hemispherical electron analyzers have not been useful in ob-

taining photoelectron angular distributions. In addition, these analyzers can only measure the photoelectron kinetic energy over a narrow energy range, and are unable to simultaneously measure a range of kinetic energies. This results in the loss of most of the photoelectrons. Therefore, these kinds of energy analyzers are only suitable for very bright light sources, such as synchrotron radiation sources. State-of-the-art two-dimensional hemispherical electron analyzers use a sophisticated electronic lens to preserve angular information, while using an MCP and a CCD camera at the detection end for two-dimensional data retrieval. The kinetic energy and emission angle of a photoelectron are mapped onto a single spot of the two-dimensional image, allowing the detector to simultaneously record a certain angular range and kinetic energy range of the photoelectrons. Thanks to such advancements, these hemispherical analyzers could be used to replace the current time-of-flight detector, providing photoelectron angular distribution information without losing the photoelectron count rate in a certain energy range. Currently, these new hemispherical electron analyzers can measure up to about $\pm 7^\circ$ photoemission angle ($\pm 15^\circ$ is under development), while simultaneously recording a 10 eV energy range with about 100 meV energy resolution [112].

Another possible design implementing angle-resolved photoemission spectroscopy borrows from the technique of "cold-target recoil-ion momentum spectroscopy" (COLTRIMS) [113, 115, 116]. COLTRIMS is used in ion-scattering experiments to simultaneously measure the kinetic energies and emission angles of ejected electrons and recoil-ions after ion collision. The key idea of COLTRIMS is the use of a strong magnetic and/or electric field inside the experimental apparatus to confine the flight paths of the ejected electrons and

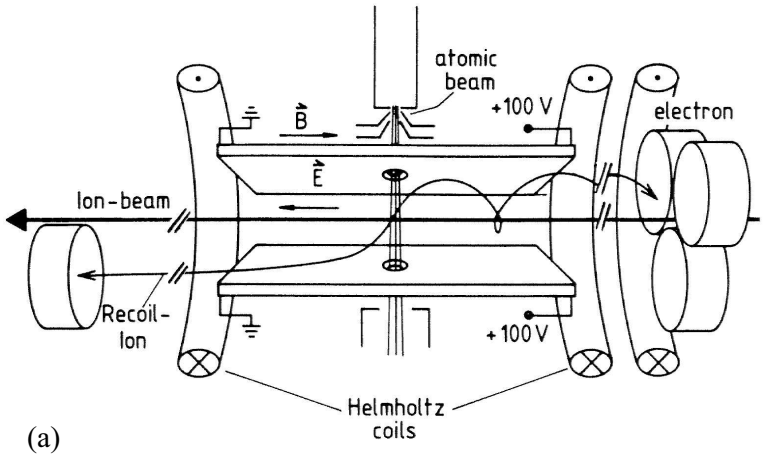

(a)

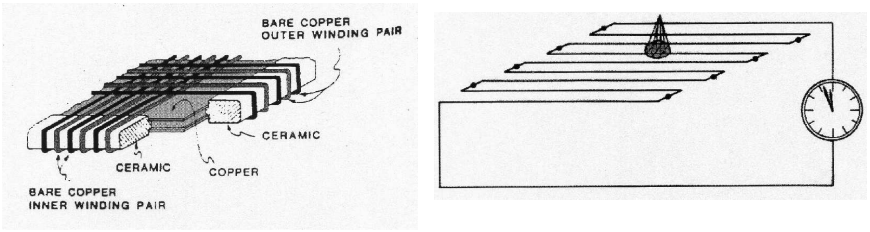

(b)

Figure 5.1: (a) Schematic drawing of "cold-target recoil-ion momentum spectroscopy" (COLTRIMS). A two-stage supersonic gas jet is installed to provide a well-defined atomic beam, which collides with an energetic ion-beam. Helmholtz coils and resistive coated parallel plates are used to generate homogeneous magnetic and electric fields to confine the recoil-ions and the ejected electrons. Position-sensitive micro-channel plates (MCP) are used to resolve the kinetic energy and emission angles of the recoil-ions and electrons. (figure reproduced from Ref. [113]) (b) The anode of the position-sensitive MCP is wrapped by a fine copper-wire (delay-line) on each dimension. When an electron strikes the anode, the position of the electrons on the detector can be extracted by measuring the time difference of the electronic signals at both ends of each delay-line. The position for each dimension can be determined independently. (figure reproduced from Ref. [114])

recoil-ions. The confined electrons and ions undergo rotational motion due to the magnetic field confinement, and their kinetic energies and emission angles can be evaluated by measuring their flight times along with the their impact positions on the detector. A time- and position-sensitive detector is used to capture both the flight time and detection position simultaneously. Such kind of detectors can be realized by using a MCP scaler with its anode wrapped by a two-dimensional delay-line array. These detectors are commercially available [114]. By measuring the time difference of the electron impact signals at both ends of each delay-line, the position of the electron impact can be determined. It is possible to adapt this idea for angle-resolved photoelectron spectroscopy by putting a metal surface into the interaction region, then measuring the kinetic energies and emission angles of the photoelectrons.

APPENDICES

APPENDIX A

Theoretical formalism of adsorbate desorption induced by ultrafast pulses on metal surfaces

The theory of ultrafast laser-induced chemical reactions on metal surfaces is still under development, nevertheless it is beneficial to review current theory in explaining this emerging "femtochemistry" field. In particular, the desorption of adsorbates from metal surfaces has been studied for about a decade, both experimentally and theoretically. Theories based on inelastic scattering from nonthermal surface electrons have been used to explain this unconventional desorption process. Furthermore, as was shown experimentally in chapter III and IV, non-thermal surface electrons also play an important role in excitation of chemisorbed states, and molecular vibrational modes. Therefore, a brief review of current theories of desorption can give insight to help understand various possible explanations.

A.1 Desorption induced by electronic transition (DIET)

Conventional thermal-driven chemical reactions on metal surfaces are thought to be a process of the adsorbate molecules overcoming the reaction energy barrier required for desorption, by progressively acquiring energy from the surface lattice phonons. However,

femtochemistry on metal surfaces cannot be explained using traditional theories. New theories have been proposed to explain the underlying mechanism of this new phenomenon.

When an energetic electron inelastically scatters with a molecule in the gas phase, the probability of vibrationally exciting the molecule through electron scattering is well known to be greatly increased if the incident electron can be trapped into a "shape resonance". This shape resonance corresponds to a particular orbital of the gas-phase molecule that forms a temporary negative molecular ion [117, 118, 119, 120, 121]. This can be explained by "Franck-Condon" principle [122]: When an electron is trapped into a molecular orbital, the "Born-Oppenheimer" (BO) or "Adiabatic" approximation [123] can be applied. Under this approximation, atomic motion is considered to be "frozen" while the electronic transition is occurring; i.e., the motion of electrons is much faster than the motion of the atomic nuclei. The sudden change of the molecule's Hamiltonian due to this excited state transition instantaneously effects the forces on the nuclei, causing the molecule to vibrate.

This theory can be used to describe the process of adsorbate desorption from metal surfaces via intense ultrafast pulses. An intense laser field generates hot surface electrons on a metal surface, and these electrons can tunnel into the unoccupied states of the adsorbates, initiating the process of desorption.

The effectiveness of resonant excitation depends on two important factors. First, the incident electrons must be trapped in a "bond-significant" orbital; that is, one whose occupancy provides new forces on the atomic constituents. In this way, the equilibrium geometry of the negative ion differs from that of the original neutral target. It is very important that the electron be trapped in order to efficiently transfer energy via Franck-

Condon excitation. Under these conditions, the excited potential energy surface (PES) of the atomic space, modified by the trapped electrons, sets the atoms in motion. In contrast, pure inelastic scattering between energetic electrons and atoms does not transfer enough energy from the electron to the atom because the atom is much heavier than the electron in weight.

Second, the effectiveness of this resonant bond excitation depends strongly on the lifetime of the resonant negative-ion state relative to a characteristic time scale for "significant" nuclear motion on the excited PES. For example, for adsorbate desorption from metal surfaces, the highest possibility of molecular desorption occurs when the adsorbate-metal bond is at its point of greatest compression or expansion. In this situation, the lifetime of the trapped ion will be close to one-half of the vibrational period of the adsorbates.

A.1.1 Resonant excitation by non-thermal surface electrons

On metal surfaces, nonthermal surface electrons created by ultrafast pulses become the equivalent of energetic incoming electrons to the molecules in the gas phase. Similar to conventional thermal surface chemistry, the temperatures of the surface electrons and the phonons (lattice) reach an equilibrium at all times. In femtochemistry, energy from the ultrafast pulses heats the surface electrons within the first picosecond, while the motion of the surface lattice is slow. Thus, the lattice remains unperturbed some picoseconds after the excitation. Figure A.1 is a schematic diagram showing the energy level of an adsorbate that is adsorbed onto a metal surface. The highest occupied molecular orbital (HOMO) of the adsorbate is partially filled by electrons, up to the Fermi-level, while the lowest unoccupied molecular orbital (LUMO) of the adsorbate is left unfilled. In general, there is an energy

barrier between the adsorbate and the metal surface, which is created by the space-group symmetry broken on the metal surface. This barrier prevents the metal's surface electrons freely propagating into the adsorbate orbitals [123]. Before laser excitation, the adsorbate is in equilibrium with the metal surface and resides in the ground state PES of the system.

When an ultrafast pulse hits the metal surface, individual surface electrons will adsorb one photon from the ultrafast pulse, raising their kinetic energy by $h\nu$. Since metals have no band gap, electrons can exist at a range of energies above the Fermi-edge (from ε_{Fermi} to $\varepsilon_{Fermi} + h\nu$), as shown in Fig. A.1. These excited electrons produce a photoelectron current $\equiv j_{el}(\mathbf{k}(\varepsilon_{in}; h\nu))$ from within the surface which is incident upon the adsorbed molecules. If the energy level of the LUMO state of the adsorbates falls within this energy range, the nonthermal surface electrons, having acquired sufficient energy, can transfer (or tunnel) to the adsorbate molecules by the process of resonance scattering. Typically, the incident electrons will reside in this resonance state for a time τ_R, and then scatter back into an unoccupied conduction band state with energy $\varepsilon_f \leq \varepsilon_i$, leaving the adsorbate excited with a net energy $\Delta\varepsilon = \varepsilon_i - \varepsilon_f$.

When an electron scatters into the LUMO state, the adsorbates' Hamiltonian changes suddenly. Thus, the adsorbates are excited from the ground state PES to an excited state PES. The BO approximation tells us that the electronic state of the adsorbate system determines the PES for the adsorbate nuclei. Therefore, when an extra electron couples to the LUMO state of the adsorbate, the adsorbate is suddenly excited to an excited-state PES, and atomic forces subsequently cause the nuclei of the adsorbates to move. The results is atomic motion, mediated by non-thermal electrons, can lead to a cleav-

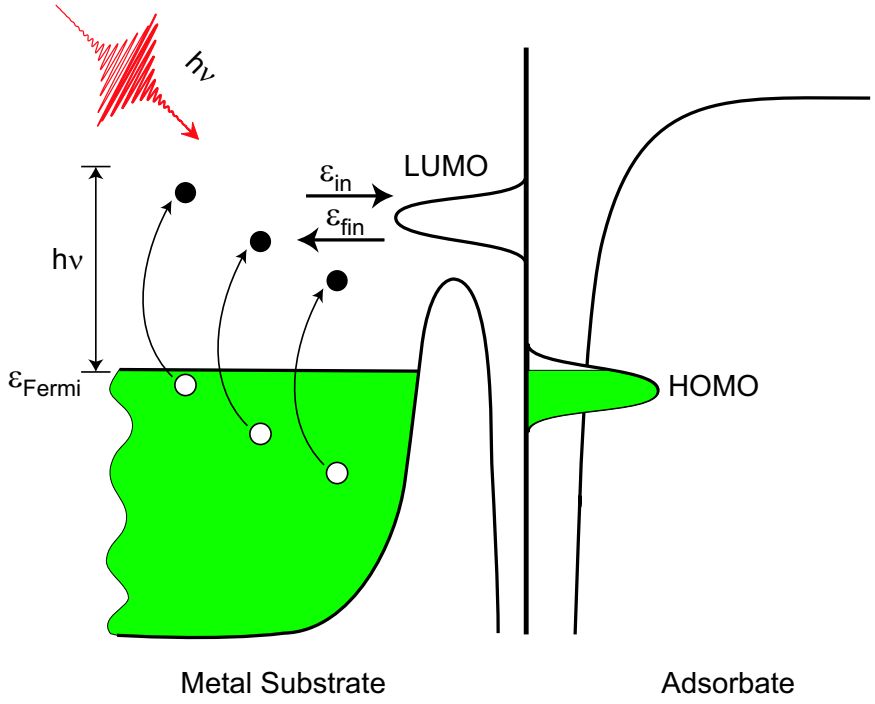

Figure A.1: Energy level diagram showing that the non-thermal electrons are energized rapidly by an intense ultrafast pulse. These “hot” electrons could scatter into the LUMO state of the adsorbates to transfer energy to excite the molecular motions through Franck-Condon excitation scheme. (figure reproduced from Ref. [79])

age of the bond between the adsorbates and the surface, ultimately leading to desorption. This desorption scheme is generally called “Desorption Induced by Electronic Transition” (DIET).[124, 125]

A schematic diagram of the DIET process, depicted in Fig. A.2, shows the PES (one-dimensional curve for simplicity) associated with the electronic ground and excited states. There are two scenarios under which DIET can occur, depending on the nature of the adsorbates’ excited-state PES.

Fig. A.2(a) depicts the most straight forward DIET process, in which the adsorbates enter a repulsive excited-state PES. After the adsorbate enters the excited-state PES, characterized by an repulsive potential V_{excite}, the adsorbate is accelerated on an outward trajectory. Under this scenario, three outcomes are possible. The first case (and most typical) is a rapid relaxation of the adsorbate, falling back onto the ground-state PES V_0, with a slightly displaced from the equilibrium position z_0. The adsorbate has picked some kinetic energy by temporally residing on V_{excite}, but not enough to overcome the energy barrier for desorption. Classically, this means that relaxation occurs prior to the adsorbates’ trajectory arriving at the diabetic curve crossing point $z = z_c$. The second possible outcome, and the major desorption channel for the adsorbate, occurs when the adsorbate resides on V_{excite} long enough to cross the point z_c, later relaxing back to V_0 with kinetic energy $\varepsilon^* = V_{excite}(z_0) > \varepsilon_0^{inf}$, i.e., enough to overcome the energy barrier for desorption. The final case, which is rare, occurs when the adsorbate stays on the excited-state PES until complete desorption happens.

Another scenario of the DIET process, which is strongly dependent on the adsorbate

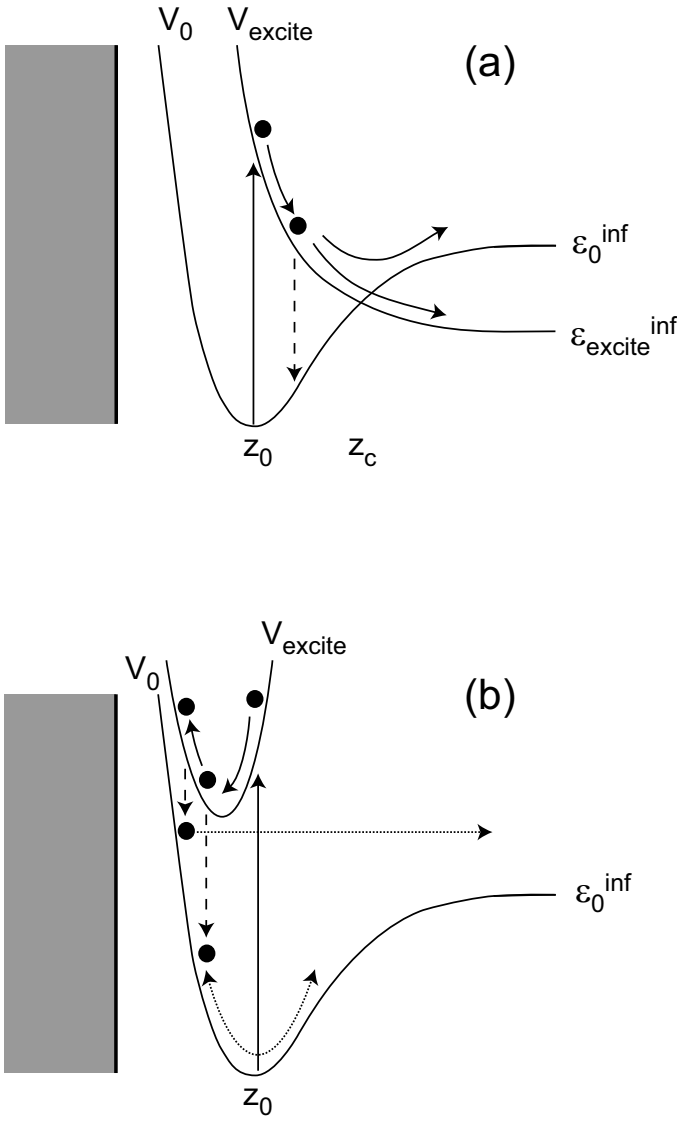

Figure A.2: Potential curves illustrating the process of Desorption Induced by Electronic Transition (DIET). (a) Intra-molecular electronic excitation involving bound-to-repulsive excitation; (b) Intra-molecular electronic excitation involving attractive intermediate state mediation. (figure reproduced from Ref. [79])

motion over V_{excite}, is illustrated in Fig. A.2(b). Here the excited-state PES is more closely bonded to the surface than the ground-state PES. When this happens, the adsorbate will be pulled towards the metal surface following the electronic transfer. Consequently, the initial accelerated nuclear motion is directed inwards such that when the excited state decays back to the ground state (usually within a fraction of a vibrational period), not only has the adsorbate acquired kinetic energy but, perhaps more importantly, it is returned high up on the repulsive wall of the ground-state PES, with a compressed bond between surface and adsorbate. Depending upon the parameters, while the adsorbate is in the intermediate excited-state PES, it may or may not obtain sufficient kinetic energy to desorb once back in the ground-state PES. Both situations (successful desorption and remaining adsorbed) are shown in Fig. A.2(b).

A.1.2 Desorption probability

The energy-resolved production rate for adsorbates with total energy ε, due to resonance scattering by the non-thermal surface electrons is written as $d\dot{N}(\varepsilon;\tau_R,h\nu)/d\varepsilon$. The non-thermal surface electrons are scattered from state $\mathbf{k}_i$ to state $\mathbf{k}_f$, with energy ε_i and $\varepsilon_f = \varepsilon_i - \varepsilon \geq \varepsilon_{Fermi}$, respectively [79]. This give us

$$\frac{d\dot{N}}{d\varepsilon}(\varepsilon;\tau_R,h\nu) = \sum_{\mathbf{k}_i,\mathbf{k}_f} j_{el}(\mathbf{k}_i;h\nu)\sigma_{Tot}(\varepsilon_i(\mathbf{k}_i);\varepsilon_f(\mathbf{k}_f);\tau_R)\delta(\varepsilon_i-\varepsilon_f-\varepsilon) \qquad \text{(A.1)}$$

In this expression, τ_R is the propagation time the adsorbate spends on the excited-state PES $V_-(z)$ before decaying back to the ground-state PES $V_a(z)$. $j_{el}(\mathbf{k}_i;h\nu)$ is the flux distribution of non-thermal surface electrons incident upon the adsorbates. The flux is characterized by the wave-vector $\mathbf{k}_i$ and depends on the laser photon energy $h\nu$. $\sigma_{Tot}(\varepsilon_i(\mathbf{k}_i);\varepsilon_f(\mathbf{k}_f);\tau_R)$ is the total inelastic resonance scattering cross-section, which depends on the incident en-

ergy ε_i, and exit energy ε_f of the electron, and the propagation time τ_R. Equation A.1 can be simplified under some reasonable assumptions, (concerning relatively weak optical excitation [79]), to

$$\frac{d\dot{N}}{d\varepsilon}(\varepsilon;\tau_R,h\nu) \approx Q_{Res}(\varepsilon,h\nu)P(\varepsilon,\tau_R) \tag{A.2}$$

where $P(\varepsilon,\tau_R)$ is the total probability distribution for exciting the molecule with energy ε. A graphical description of $P(\varepsilon,\tau_R)$ is shown in Fig. A.3. Q_{Res} is the electronic factor, which is assumed to be slowly varying over the energy spread of $P(\varepsilon,\tau_R)$. Here, the electronic factor Q_{Res} is approximated to be a constant, and includes all the averaged effects of the incident flux j_{el} and the scattering cross-section σ_{Tot} that occur during the scattering process. The distribution $P(\varepsilon,\tau_R)$ can be evaluated using various microscopic theories. The "Gaussian wavepacket model" is commonly used as it provides a physically intuitive picture of the desorption mechanism using features of classical mechanics while retaining many quantum attributes.

Using the "Gaussian wavepacket model", the distribution $P(\varepsilon,\tau_R)$ can be written as [126]

$$P(\varepsilon;\tau_R) = \frac{1}{\Delta(\tau_R)\sqrt{2\pi}}\exp\left[-\frac{1}{2}\left(\frac{\varepsilon-\varepsilon_f(\tau_R)}{\Delta(\tau_R)}\right)^2\right] \tag{A.3}$$

with

$$\Delta(\tau_R) \equiv \bar{u}V_a'(z_{\tau_R})[1+(\omega\tau_R)^2]^{1/2} \tag{A.4}$$

and

$$\varepsilon_f(\tau_R) = \frac{p_{\tau_R}^2}{2M} + V_a(z_{\tau_R}) \tag{A.5}$$

Equation A.4 shows that the width of the energy distribution after the wavepacket returns

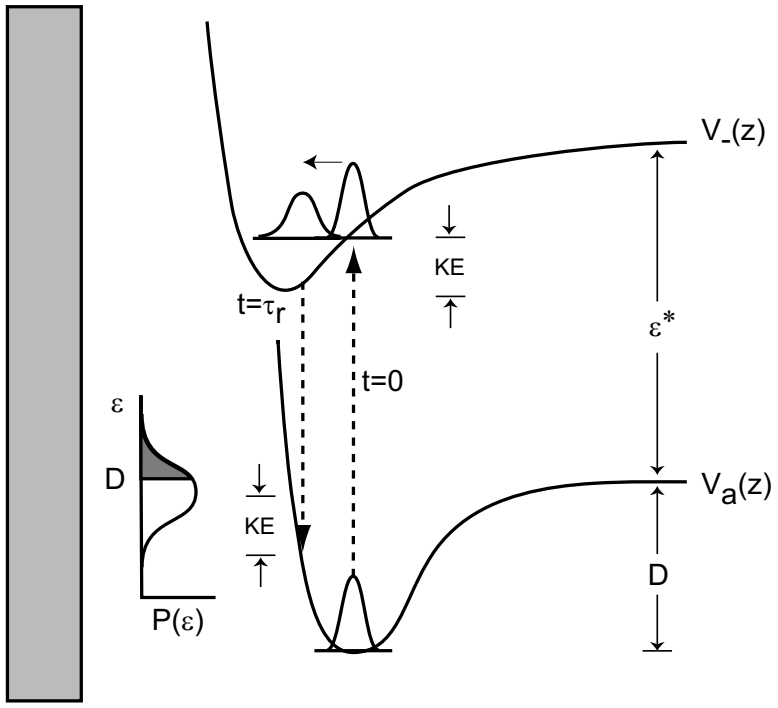

Figure A.3: Potential energy curves of center-of-mass translational motion of the chemisorbed ion (charge transfer from surface) with respect to the surface, showing wavepacket propagation throughout the time sequence involving the negative-ion LUMO resonance. The distribution of the final adsorbate states, between vibrationally excited bound (white) and desorptive continuum states (black) is shown as $P(\varepsilon)$ versus ε. (figure reproduced from Ref. [79])

to the ground-state PES $V_a(z)$ at τ_R is determined by the combination of $\bar{u} = (\hbar/2M\omega)^{1/2}$, the spread of the original ($t = 0$) oscillator probability distribution V_a', the slope of V_a at the point of return, and the additional width acquired while propagating on V_-.

The desorption probability for the adsorbates can then be determined by integrating $P(\varepsilon; \tau_R)$ from the desorption barrier D to infinity. This is

$$P_{des}(\tau_R) = \int_D^{\hbar\nu} P(\varepsilon; \tau_R) d\varepsilon \tag{A.6}$$

which for $\hbar\nu \gg D$ reduces to

$$P_{des}(\tau_R) \simeq 0.5 \left[1 - \mathrm{erf}\left(\frac{D - \varepsilon_f(\tau_R)}{\sqrt{2}\Delta(\tau_R)}\right)\right] \tag{A.7}$$

A.2 Desorption induced by multiple electronic transition (DIMET)

The desorption rate $P_{des}(\tau_R)$ of the adsorbates depends on the propagation time τ_R, as the adsorbates undergo motion on the excited-state PES in this time scale to obtain kinetic energy to overcome the desorption barrier D. In general, the propagation time τ_R can be interpreted as the time that non-thermal electrons spend in the LUMO state of the adsorbate, and is in general very short. Therefore, most adsorbates will not be able to obtain enough kinetic energy to escape from the well upon returning to the ground-state PES $V_a(z)$. This does not explain the non-traditional exponential increase in desorption with ultrafast laser excitation.

In the conventional DIET scheme, most of the adsorbates will not contribute to the desorption yield as not enough kinetic energy is generally obtained in a single excitation process. In DIMET [11, 127], on the other hand, adsorbates could be re-excited before its kinetic energy gained through the previous DIET process is totally relaxed, due to the high

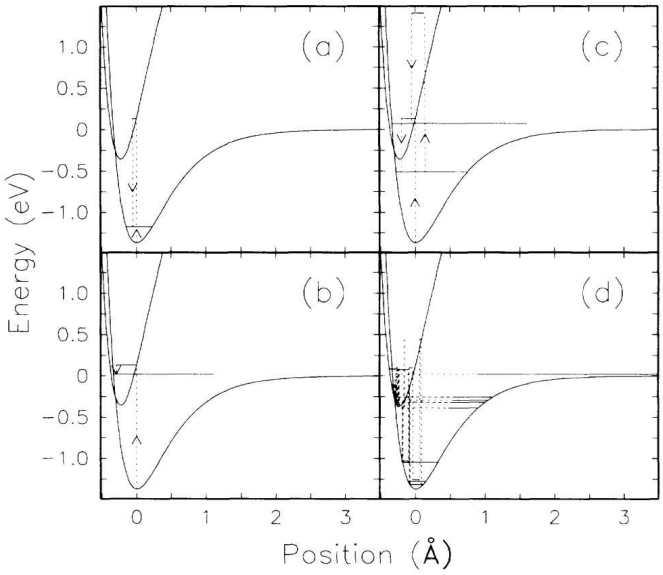

Figure A.4: Trajectories for motion on the ground and excited PES. The dotted lines represent the total energy of the adsorbate complex, with vertical segments arising from Franck-Condon transitions and horizontal segments from conservative motion on a given PES. (a)(b) Trajectories displayed associated with a single-excitation DIET process. (c)(d) Trajectories for the multiple-excitation DIMET process. (figure reproduced from Ref. [11])

concentration of non-thermal surface electrons. This situation is shown in Fig. A.4(c) and (d). The adsorbate makes another Franck-Condon transition, this time from a vibrationally excited level of the ground-state PES. The additional energy associated with the vibrational excitation allows the adsorbate to desorb more easily previously discussed excitations. However, if the excitations are separated by more than the lifetime of the adsorbate-surface vibration, the DIMET mechanism is simply several single DIET excitations, which will not lead to enhancement of the desorption yield.

BIBLIOGRAPHY

BIBLIOGRAPHY

[1] S. Backus, C. Durfee, M. Murnane, and H. Kapteyn. High power ultrafast lasers. *Rev. Sci. Instrum.*, 69(3):1207–1223, 1998.

[2] G. A. Somorjai. *Intorduction to surface chemistry and catalysis*. John Wiley & Sons, 1994.

[3] Z. Chang, A. Rundquist, H. Wang, M. M. Murnane, and H. C. Kapteyn. Generation of coherent soft x-rays at 2.7 nm using high harmonics. *Phys. Rev. Lett.*, 79(16-20):2967–2970, 1997.

[4] C. Durfee, A. Rundquist, S. Backus, C. Herne, M. Murnane, and H. Kapteyn. Phase matching of high-order harmonics in hollow waveguides. *Phys. Rev. Lett.*, 83(11):2187–2190, 1999.

[5] A. Paul, R. A. Bartels, R. Tobey, H. Green, S. Weiman, I. P. Christov, M. M. Murnane, H. C. Kapteyn, and S. Backus. Quasi-phase-matched generation of coherence extreme-ultraviolet light. *Nature*, 421(6918):51–54, 2003.

[6] F. J. Kao, D. G. Busch, D. Cohen, D. Gomes da Costa, and W. Ho. Femtosecond laser desorption of molecular adsorbed oxygen from Pt(111). *Phys. Rev. Lett.*, 71(13):2094–2097, 1993.

[7] J. A. Prybyla, T. F. Heinz, J. A. Misewich, M. M. T. Loy, and J. H. Glownia. Desorption induced by femtosecond laser pulses. *Phys. Rev. Lett.*, 64(13):1537–1540, 1990.

[8] L. M. Struck, L. J. Richter, S. A. Buntin, R. R. Cavanagh, and J. C. Stephenson. Femtosecond laser-induced desorption of CO from $\mathrm{Cu}(100)$: Comparison of theory and experiment. *Phys. Rev. Lett.*, 77(22):4576–4579, 1993.

[9] G. Eichorn, M. Richter, K. Al-Shamery, and H. Zacharias. Time-correlated laser desorption of NO from NiO(100)/Ni(100). *Chem. Phys. Lett.*, 289(3-4):367–372, 1998.

[10] F. Budde, T. F. Heinz, M. M. T. Loy, J. A. Misewich, F. de Rougemont, and H. Zacharias. Femtosecond time-resolved measurement of desorption. *Phys. Rev. Lett.*, 66(23):3024–3027, 1991.

[11] J. A. Misewich, A. Kalamarides, T. F. Heinz, U Höfer, and M. M. T. Loy. Vibrationally assisted electronic desorption: Femtosecond surface chemistry of $O_2/Pd(111)$. *J. Chem. Phys.*, 100(1):736–739, 1994.

[12] S. Deliwala, R. Finlay, J. Goldman, T. Her, W. Mieher, and E. Mazur. Surface femtochemistry of O_2 and CO on $Pt(111)$. *Chem. Phys. Lett.*, 242(6):617–622, 1995.

[13] W. D. Mieher and W. Ho. Bimolecular surface photochemistry: Mechanisms of co oxidation on $Pt(111)$ at 85 K. *J. Chem. Phys.*, 99(11):9279–9295, 1993.

[14] F. J. Kao, D. G. Busch, D. Gomes da Costa, and W. Ho. Femtosecond versus nanosecond surface photochemistry – O_2+CO on $Pt(111)$ at $80K$. *Phys. Rev. Lett.*, 70(26):4098–4101, 1993.

[15] T. Her, R. J. Finlay, C. Wu, and E. Mazur. Surface femtochemistry of $CO/O_2/Pt(111)$: The importance of nonthermalized substrate electrons. *J. Chem. Phys.*, 108(20):8595–8598, 1998.

[16] M. Bonn, S. Funk, C. Hess, D. Denzler, C. Stampfl, M. Scheffler, M. Wolf, and G. Ertl. Phonon- versus electron-mediated desorption and oxidation of CO on $Ru(0001)$. *Science*, 285(5430):1042–1045, 1999.

[17] W. Steinmann and Th. Fauster. Two-photon photoelectron spectroscopy of electronic states at metal surfaces. In H. L. Dai and W. Ho, editors, *Laser spectroscopy and photochemistry on metal surfaces*, Advanced series in physical chemistry, chapter 5. World Scientific Publishing, 1995.

[18] S. Schuppler, N. Fischer, Th. Fauster, and W. Steinmann. Lifetime of image-potential states on metal surfaces. *Phys. Rev. B*, 46(20):13539–13547, 1992.

[19] R. W. Schoenlein, J. G. Fujimoto, G. L. Eesley, and T. W. Capehart. Femtosecond studies of image-potential dynamics in metals. *Phys. Rev. Lett.*, 61(22):2596–2599, 1988.

[20] R. W. Schoenlein, J. G. Fujimoto, G. L. Eesley, and T. W. Capehart. Femtosecond relaxation dynamics of image-potential states. *Phys. Rev. B*, 43(6):4688–4698, 1991.

[21] R. W. Schoenlein, J. G. Fujimoto, G. L. Eesley, and T. W. Capehart. Femtosecond dynamics of the n=2 image-potential state on $Ag(100)$. *Phys. Rev. B*, 41(8):5436–5439, 1990.

[22] M. Bauer, S. Pawlik, and M. Aeschlimann. Decay dynamics of photoexcited alkali chemisorbates: Real-time investigations in the femtosecond regime. *Phys. Rev. B*, 60(7):5016–5028, 1999.

[23] M.Bauer, S. Pawlik, and M. Aeschlimann. Resonance lifetime and energy of an excited Cs state on $Cu(111)$. *Phys. Rev. B*, 55(15):10040–10043, 1997.

[24] M. Bauer, S. Pawlik, R. Burgermeister, and M. Aeschlimann. Symmetry properties of an electron alkali excitation at a noble metal surface as investigated by two-photon photoemission. *Surf. Sci.*, 402-404:62–65, 1998.

[25] M. Bauer, S. Pawlik, and M. Aeschlimann. Femtosecond lifetime investigations of excited adsorbate states: atomic oxygen on $\mathrm{Cu}(111)$. *Surf. Sci.*, 377-379:350–354, 1997.

[26] Th. Fauster and W. Steinmann. *Photonic probes of Surface*, page 347. North-Holland, Amsterdam, 1995.

[27] H. Petek, M. Weida, H. Nagano, and S. Ogawa. Real-time observation of adsorbate atom motion above a metal surface. *Science*, 288(5470):1402–1404, 2000.

[28] S. Ogawa, H. Nagano, and H. Petek. Phase and energy relaxation in an antibonding surface state: $\mathrm{Cs/Cu}(111)$. *Phys. Rev. Lett.*, 82(9):1931, 1999.

[29] A. G. Borisov, A. K. Kazansky, and J. P. Gauyacq. Stabilisation of alkai-adsorbate-induced states on $\mathrm{Cu}(111)$ surfaces. *Surf. Sci.*, 430(1-3):165–175, 1999.

[30] W. S. Fann, R. Storz, H. W. K. Tom, and J. Bokor. Electron thermalizaton in gold. *Phys. Rev. B*, 46(20):13592–13595, 1992.

[31] P. B. Allen. Theory of thermal relaxation of electrons in metals. *Phys. Rev. Lett.*, 59(13):1460–1463, 1987.

[32] W. S. Fann, R. Storz, H. W. K. Tom, and J. Bokor. Direct measurement of nonequilibrium electron-energy distributions in subpicsecond laser-heated gold films. *Phys. Rev. Lett.*, 68(18):2834–2837, 1992.

[33] J. Bokor and W. S. Fann. Ultrafast hot electron relaxation in metals. In H. L. Dai and W. Ho, editors, *Laser spectroscopy and photochemistry on metal surfaces*, Advanced series in physical chemistry, chapter 8. World Scientific Publishing, 1995.

[34] J. A. Prybyla, H. W. K. Tom, and G. D. Aumiller. Femtosecond time-resolved surface reaction: Desorption of CO from $\mathrm{Cu}(111)$ in < 325 fs. *Phys. Rev. Lett.*, 68(4):503–506, 1992.

[35] M. Bonn, C. Hess, S. Funk, J. Miners, B. Persson, M. Wolf, and G. Ertl. Femtosecond surface vibrational spectroscopy of CO adsorbed on $\mathrm{Ru}(001)$ during desorption. *Phys. Rev. Lett.*, 84(20):4653–4656, 2000.

[36] Ch. Hess, M. Wolf, S. Roke, and M. Bonn. Femtosecond time-resolved vibrational sfg spectroscopy of $\mathrm{CO/Ru}(001)$. *Surf. Sci.*, 502-503:304–312, 2002.

[37] Y. R. Shen. Surface nonlinear optics: a historical prospective. *IEEE J. Sel. Top. Quant.*, 6(6):1375, 2000.

[38] Y. R. Shen. Surface-properities probed by 2nd-harmonic and sum-frequency generation. *Nature*, 337(6027):519–525, 1989.

[39] B. N. J. Persson, F. M. Hoffmann, and R. Ryberg. Influence of exciton motion on the shape of optical absorption lines: Applications to vibrations at surfaces. *Phys. Rev. B*, 34:2266–2283, 1989.

[40] R. W. Schoenlein, W. P. Leemans, A. H. Chin, P. Volfbeyn, T. E. Glover, P. Balling, M.S Zolotorev, K.-J. Kim, S. Chattopadhyay, and C. V. Shank. Femtosecond x-ray pulses at 0.4 Å generated by 90^o thomson scattering: A tool for probing the structural dynamics of materials. *Science*, 274(11):236–238, 1996.

[41] W. P. Leemans, R. W. Schoenlein, P. Volfbeyn, A. H. Chin, T. E. Glover, P. Balling, M.S Zolotorev, K.-J. Kim, S. Chattopadhyay, and C. V. Shank. Interaction of relativistic electrons with ultrashort laser pulses: generation of femtosecond x-rays and microprobing of electronbeams. *IEEE J. Quant. Electr.*, 33(11):1925–1934, 1997.

[42] K.-J. Kim, S. Chattopadhyay, and C. V. Shank. Generation of femtosecond x-rays by 90^o thomson scattering. *Nucl. Instrum. Meth. A*, 341(1-3):351–354, 1994.

[43] C. Pellegrini, J. Rosenzweig, G. Travish, K. Bane, R. Boyce, G. Loew, P. Morton, H.-D. Nuhn, J. Paterson, P. Pianetta, T. Raubenheimer, J. Seeman, R. Tatchyn, V. Vylet, H. Winick, K. Halbach, K.-J. Kim, M. Xie, D. Prosnitz, E. T. Scharlemann, R. Bonifacio, L. De Salvo, and P. Pierini. The SLAC soft x-ray high power FEL. *Nucl. Instru. Meth. A*, 341(1-3):326–330, 1994.

[44] G. N. Kulipanov, A. N. Skrinsky, and N. A. Vinokurov. Sychrotron light sources and recent developments of accelerator technology. *J. Synchr. Rad.*, 5(3):176–178, 1998.

[45] K.-J. Kim. Advanced capabilities for future light sources. *J. Synchr. Rad.*, 5(3):202–207, 1998.

[46] D. Attwood, editor. *Soft X-rays and extreme ultraviolet radiation*. Cambridge University Press, 1999.

[47] P. A. Franken, A. E. Hill, C. W. Peters, and G. Weinreich. Generation of optical harmonics. *Phys. Rev. Lett.*, 7(4):118–119, 1961.

[48] A. L'Huillier, M. Lewenstein, and P. Balcou. *Harmonic generation in strong laser fields*. Cambridge University Press, 2004.

[49] J. Diels and W. Rudolph, editors. *Ultrashort Laser Pulse Phenomena*. Academic Press, 1996.

[50] A. L'Huillier and Ph. Balcou. High-order harmonic generation in rare gases with a 1-ps 1053-nm laser. *Phys. Rev. Lett.*, 70(6):774–777, 1993.

[51] P. B. Corkum. Plasma perspective on strong-field multiphoton ionization. *Phys. Rev. Lett.*, 71(13):1994–1997, 1993.

[52] J. L. Krause, K. J. Schafer, and K. C. Kulander. High harmoinc generation from atoms and ions in the high intensity regime. *Phys. Rev. Lett.*, 68(24):3535–3538, 1992.

[53] K. J. Schafer and K. C. Kulander. High harmoinc generation from ultrafast pump lasers. *Phys. Rev. Lett.*, 78(4):638–641, 1997.

[54] R. Trebino, editor. *Frequency-Resolved Optical Gating: The measurement of Ultrashort Laser Pulses*. Kluwer Academic Publishers, 2002.

[55] L. Nugent-Glandorf, M. Scheer, D. A. Samuels, V. Bierbaum, and S. R. Leone. A laser-based instrument for the study of ultrafast chemical dynamics by soft x-ray-probe photoelectron spectroscopy. *Rev. Sci. Instrum.*, 73(4):1875–1886, 2002.

[56] L. Nugent-Glandorf, M. Scheer, D. A. Samuels, V. Bierbaum, and S. R. Leone. Ultrafast photodissociation of Br_2: Laser-generated high-harmonic soft x-ray probing of the transient photoelectron spectra and ionization cross sections. *J. Chem. Phys.*, 117(13):6108–6116, 2002.

[57] Website of the center of x-ray optics, Lawrence Berkely National Laboratory. http://cindy.lbl.gov.

[58] A. Stolow. Gigahertz bandwidth ultrahigh vacuum 50 Ω coaxial high-voltage coupling capacitor for photoelectron spectroscopy. *Rev. Sci. Instrum.*, 67(5):1777–1780, 1996.

[59] J. A. R. Samson. *Techniques of vacuum ultraviolet spectroscopy*. John Wiley & Sons, 1967.

[60] R. B. Cairns and J. A. R. Samson. Metal photocathodes as secondary standards for absolute intensity measurements in the vacuum ultraviolet. *J. Opt. Soc. Am.*, 56(11):1568–1573, 1966.

[61] J. L. Wiza. Microchannel plate detectors. *Nucl. Instrum. Meth.*, 162(1-3):587–601, 1979.

[62] M. Drescher, M. Hentschel, R. Kienberger, G. Tempea, C. Spielmann, G. A. Reider, P. B. Corkum, and F. Krausz. X-ray pulses approaching the attosecond frontier. *Science*, 291(5510):1923–1927, 2001.

[63] C. Puglia, A. Nilsson, B. Hernnas, O. Karis, P. Bennich, and N. Martensson. Physisorbed, chemisorbed and dissociated O_2 on $\mathrm{Pt}(111)$: Studied by different core-level spectroscopy methods. *Surf. Sci.*, 342(1-3):119–133, 1995.

[64] W. Wurth, J. Stöhr, P. Feulner, X. Pan, K. R. Bauchspiess, Y. Baba, E. Hudel, G. Rocker, and D. Menzel. Bonding, structure, and magnetism of physisorbed and chemisorbed O_2 on Pt(111). *Phys. Rev. Lett.*, 65(19):2426–2429, 1990.

[65] J. Gland, B. Sexton, and G. Fisher. Oxygen interactions with the $\mathrm{Pt}(111)$ surface. *Surf. Sci.*, 95(2-3):587–602, 1980.

[66] W. Eberhardt, T. Upton, S. Cramm, and L. Incoccia. Inner valence levels as a structural probe for chemisorbed molecules: O_2 on $\mathrm{Pt}(111)$. *Chem. Phys. Lett.*, 146(6):561–565, 1988.

[67] S. Lehwald, H. Ibach, and H. Steininger. Overtones and multiphoton processes in vibration spectra of adsorbed molecules. *Surf. Sci.*, 117(1-3):342–351, 1982.

[68] A. Eichler and J. Hafner. Reaction channels for the catalytic oxidation of CO on $\mathrm{Pt}(111)$. *Surf. Sci.*, 433-435:58–62, 1999.

[69] A. Eichler and J. Hafner. Molecular precursors in the dissociative adsorption of O_2 on $\mathrm{Pt}(111)$. *Phys. Rev. Lett.*, 79(22):4481–4484, 1997.

[70] A. Eichler, F. Mittendorfer, and J. Hafner. Precursor-mediated adsorption of oxygen on the (111) surfaces of platinum-group metals. *Phys. Rev. B*, 62(7):4744–4755, 2000.

[71] B. Stipe, M. Rezaei, and W. Ho. Atomistic studies of O_2 dissociation on $\mathrm{Pt}(111)$ induced by photons, electrons, and by heating. *J. Chem. Phys.*, 107(16):6443–6447, 1997.

[72] B. Stipe, M. Rezaei, W. Ho, S. Gao, M. Persson, and B. Lundqvist. Single-molecule dissociation by tunneling electrons. *Phys. Rev. Lett.*, 78(23):4410–4413, 1997.

[73] N. R. Avery. An EELS and TDS study of molecular oxygen desorption and decomposition on $\mathrm{Pt}(111)$. *Chem. Phys. Lett.*, 96(3):371–373, 1983.

[74] T. Matsushima. The mechanism of the CO_2 formation on $\mathrm{Pt}(111)$ and polycyrstalline surfaces at low temperatures. *Surf. Sci.*, 127(3):403–423, 1983.

[75] H. Steininger, S. Lehwald, and H. Ibach. Adsorption of oxygen on $\mathrm{Pt}(111)$. *Surf. Sci.*, 123(1):1–17, 1982.

[76] M. L. Bocquet, J. Cerdà, and P. Sautet. Transformation of molecular oxygen on a platinum surface: A theoretical calculation of STM images. *Phys. Rev. B*, 59(23):15437–15445, 1999.

[77] R. J. Finlay, T. H. Her, C. Wu, and E. Mazur. Reaction pathways in surface femtochemistry: routes to desorption and reaction in $\mathrm{CO}/\mathrm{O}_2/\mathrm{Pt}(111)$. *Chem. Phys. Lett.*, 274(5-6):499–504, 1997.

[78] J. W. Gadzuk. Hot-electron femtochemistry at surfaces: on the role of multiple electron processes in desorption. *Chem. Phys.*, 251:87–97, 2000.

[79] J. W. Gadzuk. *Laser Spectroscopy and Photochemistry on Metal Surfaces*, chapter 21, pages 897–942. World Scientific, Singapore, 1995.

[80] B. Rethfeld. private communication.

[81] P. Siffalovic, M. Drescher, M. Spieweck, T. Wiesenthal, Y. C. Lim, R. Weidner, A. Elizarov, and U. Heinzmann. Laser based apparatus for extended ultraviolet femtosecond time-resolved photoemission spectroscopy. *Rev. Sci. Instrum.*, 72:30–35, 2001.

[82] E. Zarate, P. Apell, and P. M. Echenique. Calculation of low-energy-electron lifetimes. *Phys. Rev. B*, 60:2326–2332, 1999.

[83] R. Knorren, K. H. Bennemann, R. Burgermeister, and M. Aeschlimann. Dynamics of excited electrons in copper and ferromagnetic transition metals: Theory and experiment. *Phys. Rev. B*, 61:9427–9440, 2000.

[84] S. I. Anisimov, B. L. Kapeliovich, and T. L. Perelman. Electron-emission from surface of metals induced by ultrashort laser pulses. *Sov. Phys. JEPTP*, 66:776, 1974.

[85] F. Budde, T. F. Heinz amd A. Kalamarides, M. M. T. Loy, and J. A. Misewich. Vibrational distributions in desorption induced by femtosecond laser pulses - coupling of adsorbate vibration to substrate electronic excitation. *Surf. Sci.*, 283:143–157, 1993.

[86] P. D. Nolan, B. R. Lutz, P. L. Tanaka, J. E. Davis, and C. B. Mullins. Molecularly chemisorbed intermediates to oxygen adsorption on $\mathrm{Pt}(111)$: A molecular beam and electron energy-loss spectroscopy study. *J. Chem. Phys.*, 111(8):3696–3704, 1999.

[87] I. Panas and P. Siegbahn. A theoretical study of the peroxo and superoxo forms of molecular oxygen on metal surfaces. *Chem. Phys. Lett.*, 153:458–464, 1988.

[88] J. Misewich, S. Nakabayashi, P. Weigand, M. Wolf, and T. Heinz. Anomalous branching ratio in the femtosecond surface chemistry of $\mathrm{O_2/Pd}(111)$. *Surf. Sci.*, 363(1-3):204–213, 1996.

[89] T. Germer, J. Stephenson, E. Heilweil, and R. Cavanagh. Hot-carrier excitation of adlayers – time-resolved measurement of adsorbate-lattice coupling. *Phys. Rev. Lett.*, 71(20):3327–3330, 1993.

[90] M. Bauer, C. Lei, K. Read, R. Tobey, J. Gland, M. M. Murnane, and H. C. Kapteyn. Direct observation of surface chemistry using ultrafast soft-x-ray pulses. *Phys. Rev. Lett.*, 87(2):25501–25504, 2001.

[91] C. Lei, M. Bauer, K. Read, R. Tobey, Y. Liu, T. Popmintchev, M. M. Murnane, and H. C. Kapteyn. Hot-electron-driven charge transfer processes on $\mathrm{O_2/Pt}$ surface probed by ultrafast extreme-ultraviolet pulses. *Phys. Rev. B*, 66(24):245420–245430, 2002.

[92] S. Hüfner. *Photoelectron spectroscopy*. Springer-Verlag, 1995.

[93] H. J. Freund and N. Neumann. Photoemission of molecular adsorbates. *Appl. Phys. A*, 47:3–23, 1988.

[94] D. C. Harris and M. D. Bertolucci, editors. *Symmetry and spectroscopy: an introduction to vibrational and electronic spectroscopy*. Dover publications, New York, 1978.

[95] H. P. Steinrück. Angle-resolved photoemission studies of adsorbed hydrocarbons. *J. Phys.: Condens. Matter*, 8:6465–6509, 1996.

[96] G. Blyholder. CNDO model and interpretation of the photoelectron spectrum of CO chemisorbed on Ni. *J. Vac. Sci. Technol.*, 11(5):865–868, 1974.

[97] J. E. Demuth, D. Schmeisser, and Ph. Avouris. Resonance scattering of electrons from $\mathrm{N_2}$, CO, $\mathrm{O_2}$ and $\mathrm{H_2}$ adsorbed on a silver surface. *Phys. Rev. Lett.*, 47(16):1166–1169, 1981.

[98] C. L. Allyn, T. Gustafsson, and E. W. Plummer. The orientation of CO adsorbed on $\mathrm{Ni}(100)$. *Chem. Phys. Lett.*, 1:127–132, 47.

[99] K. H. Frank, H. J. Sagner, E. E. Koch, and W. Eberhardt. $2\pi^*$ level of chemisorbed CO on Ni(111): Nearest-neighbor interactions versus bonding to the substrate. *Phys. Rev. B*, 38(12):8501, 1988.

[100] N. V. Richardson and A. M. Bradshaw. The frequencies and amplitudes of CO vibrations at a metal surface from model cluster calculations. *Surf. Sci.*, 88(1):225–268, 1979.

[101] A. M. Lahee, J. P. Toennies, and Ch. Wöll. Low energy adsorbate vibrational modes observed with inelastic helium atom scattering: CO on Pt(111). *Surf. Sci.*, 117(1-3):371–388, 1986.

[102] H. Ibach and D. L. Mills, editors. *Electron Energy Loss Spectroscopy and Surface Vibrations*. Academic Press, New York, 1982.

[103] A. Alavi, P. Hu, T. Deutsch, P. Silvestrelli, and J. Hutter. CO oxidation on $\mathrm{Pt}(111)$: An $ab\ initio$ density functional theory study. *Phys. Rev. Lett.*, 80(16):3650–3683, 1998.

[104] B. Poelsema, L. K. Verheij, and G. Comsa. He-scattering investigation of CO migration on Pt(111). *Phys. Rev. Lett.*, 49(23):1731–1735, 1982.

[105] B. N. J. Persson and R. Rydberg. Vibrational phase relaxation at surface: CO on Ni(111). *Phys. Rev. Lett.*, 54(19):2119–2122, 1985.

[106] B. E. Hayden and A. M. Bradshaw. The adsorption of CO on Pt(111) studied by infrared reflection-adsorption spectroscopy. *Surf. Sci.*, 125(3):787–802, 1983.

[107] E. Schweizer, B. N. J. Persson, M. Tushaus, D. Hoge, and A. M. Bradshaw. The potential energy surface, vibrational phase relaxation and the order-disorder transition in the adsorption system $\mathrm{Pt}(111)$-CO. *Surf. Sci.*, 213(1):49–89, 1989.

[108] Ch. Hess, S. Funk, M. Bonn, D. N. Denzler, M. Wolf, and G. Ertl. Femtosecond dynamics of chemical reactions at surfaces. *Appl. Phys. A*, 71(5):477–483, 2000.

[109] P. Jakob and B. N. J. Perrson. Infrared spectroscopy of overtones and combination bands. *J. Chem. Phys.*, 109(19):8641–8651, 1998.

[110] C. Zhang, P. Hu, and A. Alavi. A density functional theory study of CO oxidation on $\mathrm{Ru}(0001)$. *J. Chem. Phys.*, 112(23):10564–10570, 2000.

[111] *X-ray data booklet*. Lawrence Berkeley National Laboratory, 2001.

[112] SES-100 and SES-200 electron spectrometer from Gammadata-Scienta, Sweden.

[113] J. Ullrich, R. Moshammer, R. Dörner, O. Jagutzki, V. Mergel, H. Schmidt-Böcking, and L. Spielberger. Recoil-ion momentum spectroscopy. *J. Phys. B: At. Mol. Opt. Phys.*, 30:2917–2974, 1997.

[114] 3-dimensional Multihit-MCP-Detector from RoentDek GmbH, Germany.

[115] R. Moshammer, M. Unverzagt, W. Schmitt, J. Ullrich, and H. Schmidt-Böcking. A 4π recoil-ion electron momentum analyzer: a high-resolution "microscope" for the investigation of the dynamics of atomic molecular and nuclear reactions. *Nucl. Instr. and Meth. in Phys. Res. B*, 108:425–445, 1996.

[116] M. A. Abdallah, A. Landers, M. Singh, W. Wolff, H. E. Wolf, E. Y. Kamber, M. Stöckli, and C. L. Cocke. Capture and ionization processes studied with $\mathrm{COLTRIMS}$. *Nucl. Instr. and Meth. in Phys. Res. B*, 154:73–82, 1999.

[117] G. J. Schulz. Resonances in electron-impact on diatomic-molecules. *Rev. Mod. Phys.*, 45(3):423–486, 1973.

[118] N. F. Lane. Theory of electron-molecule collisions. *Rev. Mod. Phys.*, 52(1):29–119, 1980.

[119] M. Allan. Study of triple-states and short-lived negative-ions by means of electron-impact spectroscopy. *J Elec. Spect. Relat. Phenom.*, 48(3-4):219–315, 1989.

[120] W. Domcke and L. S. Cederbaum. Simple formula for vibrational structure of resonances in electron-molecule scattering. *J. Phys. B*, 10(2):L47–L52, 1977.

[121] W. Domcke and L. S. Cederbaum. Vibration-induced narrowing of electron-scattering resonances near threshold. *J. Phys. B*, 13(14):2829–2838, 1980.

[122] P. W. Atkins, editor. *Physical Chemistry*. W. H. Freeman Company, 2001.

[123] A. Groß, editor. *Theoretical Surface Science: A Microscopic Perspective*. Springer-Verlog, Berlin, 2003.

[124] D. Menzel and R. Gomer. Desorption from metal surfaces by low-energy electrons. *J. Chem. Phys.*, 41(11):3311–3328, 1964.

[125] P. A. Redhead. Interaction of slow electrons with chemisorbed oxygen. *Can. J. Phys.*, 42:886–905, 1964.

[126] J. W. Gadzuk, L. J. Richter, S. A. Buntin, D. S. King, and R. R. Cavanagh. Laser-excited hot-electron induced desorption: A theorectical model applied to $\mathrm{NO/Pt(111)}$. *Surf. Sci.*, 235(2-3):317–333, 1990.

[127] J. A. Misewich, T. F. Heinz, and D. M. Newns. Desorption induced by multiple electronic transitions. *Phys. Rev. Lett.*, 68(25):3737–3740, 1992.

ABSTRACT

Using ultrafast extreme-ultraviolet pulses for time-resolved dynamics of molecules chemisorbed on metal surfaces

by

Chi-Fong Lei

Chair: Henry C. Kapteyn

The time-resolved observation of chemical reactions on metal surfaces represents a very important step towards understanding how these surfaces work as catalysts. Developming techniques that would allow us to observe these dynamics is therefore very important for both scientific and industrial applications. However, experimental methods that combine both surface sensistivity and sub-picosecond time resolution have proven to be challenging. In this thesis, I describe a ”Time-Resolved extreme-Ultraviolet Photoemission Spectroscope” (TR-UPS), that allows us to observe the dynamics of adsorbate molecules on surfaces with femtosecond time resolution. This experimental tool combines state-of-the-art techniques for generating EUV light (42 eV photon energy, sub-10 fs pulse width) using high-harmonic generation of intense ultrafast infrared pulses, with the technique of photoelectron spectroscopy.

Two experimental investigations have been performed with the TR-UPS. A saturation layer of O_2 adsorbed onto a Pt(111) single crystal surface at 77 K results in the oxygen preferentially residing on the bridge-site of the platinum surface. By exciting the O_2/Pt system with an ultrafast pulse, we can then observe time-dependent changes in the electronic structure of the surface/adsorbate that corresponds to movement of the oxyen from the bridge-sites to the hollow-sites of the platinum surface. This change occurs in about half a picosecond. Subsequently, the oxygen molecules relax back to their original configurations in under 5 ps. In the second experiment, CO molecules are introduced onto the Pt(111) surface. The CO molecules are known to adsorb onto the platinum surface in an upright position, parallel to the platinum surface normal. Using symmetry properties of the CO molecular orbitals, I determine the oscillation period of the frustrated translational mode of the CO molecules to be about 950 fs.